Single Atom Detection Using Optical Cavities

Rachel Poldy

A thesis submitted for the degree of
Doctor of Philosophy in Physics of
The Australian National University

February 2012

DECLARATION

This thesis is an account of research undertaken between February 2007 and August 2011 at the Department of Quantum Science, formally the Department of Physics, The Australian National University, Canberra, Australia.

Except where acknowledged in the customary manner, the material presented in this thesis is, to the best of my knowledge, original, and has not been submitted in whole or part for a degree in any university.

Rachel Poldy

Rachel Poldy
August, 2011

Fan her head!…She'll be feverish after so much thinking.

Alice Through the Looking Glass, Lewis Carroll

ACKNOWLEDGEMENTS

Scientific accomplishments encompassed in the process of a PhD are rarely - probably never - realised single-handedly. In my own case, I am sure that this undertaking could never have been completed without the presence of a whole assortment of characters. I will try to restrict my written acknowledgements to a reasonable length, but my gratitude to all these people is unending, and I could write another entire dissertation on their support alone.

I have been extremely fortunate to have found myself working under the direction of two advisors who could not have been better chosen to suit my needs, academically, intellectually and emotionally. Without a doubt, the most important and influential person in this escapade has been my supervisor, Ben Buchler. I have limitless admiration for Ben's meticulous approach to understanding, and his uncanny ability (and endless patience!) to explain. His demonstration of learning and teaching through research has been an inspiring experience. Ben has also become an irreplaceable friend, and a huge support during the more trying parts of the PhD process, and life, which have both been anathema at times. Thank you so much.

Another direct influence on my experience over the last few years has been from my other supervisor John Close, who together with Nick Robins leads a research group that has been a thorough pleasure to work with. Aside from the highest regard for quality in research, John has a priceless ability to select and direct people for their best skills, and to cultivate a cohesive work place, complete with fun and humour.

I hugely admire the dedication, time and energy that Nick pours into the research and the students here. It is no exaggeration to say that without him our group would be unrecognisable.

A research environment like ours is constantly in flux but I have enjoyed the company of everyone with whom I have shared it over the last few years. Thank you to the current (and recent) students and staff who make up our own sizeable group - Paul Altin, Mattias Johnsson, Daniel Doering, Michael Hush, Stuart Szigeti, John Debs, Robin Stevenson, Gordon McDonald, Matt Jeppessen, Cristina Figl, Graham Dennis, Joe Hope (who is great) and Andre Carvalho - but also the more temporary students who have come and gone, as well as those in the other research groups within the department, in particular Gravitational Waves and Quantum Optics. I have leant things from you all and equally importantly have thoroughly enjoyed your company.

Paul, in particular, deserves my deepest gratitude, for his help, time and patience with me in the lab, but more importantly for his continual emotional presence and support; gestures that I never adequately recognise or reciprocate, but that are sincerely appreciated.

I have to acknowledge the brilliantly thorough and constructive feedback that Stuart gave me in the final days of editing and revising this document. The insights of a theorist, and in particular one who communicates as beautifully as Stuart, are always worth listening to!

Thank you also to the staff in the department mechanical workshop. They have patiently endured the tiresome experience of a student who just couldn't seem to get a design right the first time round.

I cannot over emphasise the importance for me of the elements of the last few years that have *not* been related to work. I would simply not have completed this project without the ability to escape at times: Most notably, to all my cycling friends, thank you for the rides. And to the soup group for all the food and fun.

I am indescribably indebted to my parents, Annie and Franzi, for being more supportive and understanding than I could ever have asked for.

And to Jacqui. I know you 'get it'. That has helped me through it all.

ABSTRACT

In the same way that we have the ability to detect single particles of light - photons - in optical experiments and devices, the role of a single atom counter in analogous set-ups using atoms is of notable interest. It is also a role that has yet to be properly fulfilled, particularly in the case of cold, neutral atoms. In this thesis, we investigate the use of an optical cavity of modest finesse to detect single rubidium atoms. We explore the system with theoretical modelling and experimental testing. This is the first study of optical cavities that thoroughly considers the optimisation of design for high-quantum efficiency, low-noise single-atom counting, with an investigation of such a comprehensive range of parameters.

We model the atom detection with a quantum description of a two-level atom and single cavity mode. Specifically, we numerically solve a set of ODEs that define the field of a Fabry-Perot cavity mode in a truncated Fock basis. Their solution gives the steady-state density matrix for the cavity-atom system that is subsequently used to determine the expectation values for a range of operators.

Our modelling presents a set of variables that define a large parameter space. We consider the full parameter space in order to find the best theoretical signal-to-noise ratio for a maximally coupled atom. We find good signal-to-noise ratios are achieved using both resonant and detuned frequencies for the probe laser and cavity resonance, provided the intra-cavity intensity corresponds approximately to the atomic saturation intensity. This requires increasing driving power in the probe beam as the detuning is increased. A corollary is that the probe powers resulting in the best signal-to-noise ratios - particularly for detuned detection - are higher than the saturation intensity for a typical avalanche photodiode. Consequently heterodyne detection is determined to be the best photon detection system for the cavity set-up.

We proceed to refine the model, with simulations of atomic trajectories that account for various forces within the cavity mode. The dipole force results in a strong channelling of atoms into high-coupling regions of the mode, meaning that detuned detection results in better quantum efficiencies than resonant detection. High quantum efficiencies accompanied by low false-count rates suggests the ability to detect the statistics of an atomic source with high sensitivity. A clearance of more than 20dB above the atomic noise-floor is found for detuned detection, and approximately 8dB for resonant detection.

The experimental investigation of cavity detection is realised with an under-coupled Fabry-Perot cavity with a finesse of approximately the same value as our modelled cavity: 10000. We study resonant detection. The set-up differs somewhat from the simulated process in two respects; our measurements are not shot-noise limited as in the model, and our atoms transit the cavity much faster and with lower density resulting in a substantially weaker signal. We have begun the investigation of a new atomic source that will produce slower atoms, and hopefully allow a more complete experimental study of the cavity detector.

CONTENTS

I Theory and Modelling 11

II Experimental Practicalities and Results 85

Appendices:

LIST OF FIGURES

CHAPTER

ONE

INTRODUCTION

1.1 What is 'quantum-atom optics'?

This thesis will focus on the detection of single atoms from cold atomic sources in the research field of quantum-atom optics. In its present form, quantum-atom optics is intrinsically concerned with quantum mechanics and in particular the wave-nature of massive particles. The term *atom optics* refers to the links between traditional classical and quantum optical systems that make use of light (photons) and the analogous systems that use atoms, or more generally, massive particles including ions and molecules [99].

Understanding light - how it propagates and interacts with itself and the environment - has been fundamentally important in the formation of quantum mechanics as a theoretical framework. It has also been critical to the development of one of the most indispensable tools of experimental scientific research, the laser, that is used in a plethora of scientific and technological applications. The availability of this coherent source of light has allowed us to extend the precision of our measurements of the physical world beyond the possibilities offered by thermal light sources. Quantum mechanical measurements, inevitably pertaining to the unimaginably small, allow us to determine temporal and spatial properties with precision not achievable with classical devises that typically suffer from thermal fluctuations orders of magnitude larger than the values of interest. It is therefore natural to consider the extension of atom optics to *quantum* atom optics, utilising coherent ensembles of cold atoms in place of cold thermal ensembles in precision measurement experiments [16] as well as investigations in fundamental physics [80].

It is worth remembering that 'quantum' is used as a somewhat flexible term, since what is considered 'non-classical' for light (for example, a number state) may seem perfectly classical for atoms. Nevertheless, in both photonic and atom optics, wave-particle duality is often observed, which in itself must be considered a very non-classical experience. Coherence is one of the properties most commonly thought of as non-classical for atoms and one of its principle signatures is the uniformity in time and space of the phase relationship between waves. This is *first order* coherence. More generally, coherence may be thought of as all the properties that define correlations between two sources. For atomic ensembles, the best coherence is achieved with a Bose-Einstein Condensate (BEC), and the experimental realisation of this state in 1995 [10, 40] has fuelled ongoing interest in theoretical and experimental investigations in this field. Research has included the production of atom lasers [98, 37, 61, 18, 120], the measurement of first and second-order coherence [11, 103], tuneable particle interactions [46, 38, 119, 9] and correlations [77, 103] and quantum phase transitions [15]. BECs and atom lasers are central to the field of quantum-atom optics and to the motivation behind this thesis - which will focus on the detection of single atoms from such sources - although their production and unique characteristics will not be discussed outside of this introduction. For details on the standard cooling and trapping techniques necessary for the realisation of these remarkable quantum states, the reader is referred to the extensive literature on the topic, for example reference [97].

1.2 Why detect single atoms?

It is difficult to imagine devices based on cold atoms, and in particular, condensed, coherent sources - with their adverse vacuum requirements and often restrictive topological arrangements - ever becoming common-place in the way that *photonic* lasers have done. Nevertheless there is substantial interest in their potential role as tools of precision measurement in various forms of interferometer [21, 146, 44, 39]. In horology, frequency standards based on atomic and molecular beam magnetic resonance were suggested as far back as the 1940s [113], and the current primary standard for time and frequency measurements makes use of

Ramsey interferometry in a caesium fountain clock, with a fractional frequency uncertainty of 3×10^{-16} [106]. Atomic oscillators based on optical transitions offer significantly more precision than the microwave transition in caesium, and similar technology using cold ions has produced a clock with a fractional frequency uncertainty of only 8.6×10^{-18} [32].

As well as high precision time standards, atom-interferometric devices have been used to measure the gravitational constant, G [48, 88], the fine structure constant, α [58, 28, 36] and to probe inertial forces employing measurements of accelerations and rotations with sensitivity comparable to optical gyroscopes [59]. To date, the most precise measurements achieved with atom interferometers have made use of cold thermal atomic sources offering higher fluxes than BECs [137, 108]. Although the coherence of a condensed source is an attractive feature, issues such as matter-wave-front distortion limit the sensitivity of the interferometric measurements they provide. Often, to improve such atom-beam attributes, low fluxes are used [121], but this also limits sensitivity. However, as with quantum optics using photons, in the absence of high flux, improvement of interferometric sensitivity can be accomplished using 'squeezed' states, and spin-squeezing in cold atomic samples has already been demonstrated [57, 45, 116].

1.2.1 Measuring quantum statistics

The ability to detect squeezing requires detection with a sensitivity of at least *'root N'*; that is to say that the noise of the detection system is below the Poissonian noise of a shot noise-limited atomic source, with a mean flux of N atoms per measurement interval. Indeed, as with the measurement of squeezing, *any* novel quantum statistics are only distinguishable when detection sensitivity exceeds the Poissonian limit of $\sqrt{N}$. In order to directly probe these novel quantum statistics in cold atomic gases, a detector with sensitivity at the single-atom level is desirable, and certainly a detection sensitivity of at least $\sqrt{N}$ is required. An important consideration for any detection device, is the dark-noise - or noise-floor - clearance, which tells us how much head-room there is between this *root N* limit, and the inherent noise of the detector. Given the profound difficulties in achieving sensitive atomic detection, it is a worthy pursuit to investigate the potential of a chosen detection set-up using this figure of merit. The possibility of measuring squeezing in an atom laser beam, and determining the noise-floor clearance of a cavity-based detector is an important theme in this thesis, and in particular in the work presented in chapter 4.

More generally, in the same way that quantum-photon optics makes use of single photon counters, it is reasonable to suppose that quantum-atom optics will require atom detectors with single-particle resolution. It is considered that studies of massive particle entanglement, quantum information processing, and quantum control may well rely on the manipulation and detection of single particles.

For BECs and atoms lasers, there has also been substantial interest in the measurement of higher-order coherence in atomic fields [147]. In BECs, the third-order correlation function $g^3(\mathbf{x})$ has been observed directly [68] and *via* measurement of three-body losses [27], and several experiments have measured the second-order correlation function $g^2(\mathbf{x})$ [68, 127, 77, 83]. The second order correlation-function of an atom laser has also been measured [103], but, since atom lasers tend to have lower flux than BECs, measurements using lasers instead of condensates require more sensitive detection.

1.2.2 Producing non-classical atomic beams

The production of non-classical states in an atomic ensemble is not in itself a trivial pursuit, and a detailed discussion of the theoretical and practical considerations is beyond the scope of this thesis. Nevertheless, given its role in the motivation behind this work, a brief mention as to how such states in an atom laser beam might be achieved must be included.

Mechanisms for squeezing proceed *via* interactions - or non linear terms in the Hamiltonian. In quantum optics applications, photon-photon interactions in vacuum do not occur, and a substantial engineering effort is required to produce a non-linear medium capable of optical squeezing. Atoms interact with each other and with photons, and squeeze for free, and a variety of mechanisms has been proposed for the production of squeezing in atomic beams. Atom-atom interactions can be used to create entanglement in atomic spin [43, 111]. Alternatively, the quantum state of a squeezed optical field can be transferred onto the atomic beam [49, 79, 63].

In the first case, collisions between two trapped condensate atoms in the $|m_F = 0\rangle$ spin-state, can produce a pair of atoms, one in the $|m_F = +1\rangle$ state and one in the $|m_F = -1\rangle$ state, with sufficient energy to escape the trap, generating correlated atom laser beams. Other proposals involve generating number squeezing using non-linear interactions between atoms within a BEC with two internal states [62, 132, 90, 84].

In the second case, squeezing occurs *via* atom-photon interactions. When an atomic and an optical field are coupled, they can be described together by a single mode, and complete state transfer occurs between them in a Rabi-like cycle. The creation of non-classical light is well established [20, 12, 89, 75, 114], and it seems reasonable that a non-classical atom-laser can be generated by transferring the quantum state of an optical mode to an atomic beam so that the transmitted light is entangled in amplitude and phase with the outcoupled atom laser beam [64, 63].

Finally, it is worth noting a further consideration in atomic squeezing, as compared to its optical counterpart: one complexity in optical squeezing is the immense susceptibility to loss due to scattering and absorption in a typical lab environment. The vacuum chamber required for a cold atom experiment is a sunk cost. We may as well take advantage of it and use this low loss, clean environment with squeezed atomic sources. The realisation of spin-squeezed states of a two-component Bose Einstein condensate have recently been demonstrated experimentally [57, 116].

1.3 Detection techniques

This thesis is concerned with the high quantum efficiency detection of cold atoms with single-particle resolution, using an optical cavity. The detection process relies on the coupling of the atom to the cavity field and the subsequent measurement of the field. These will be discussed in chapters 2 and 3. The interaction was described in 1963 by Jaynes and Cummings [76], and the quantised picture they presented has subsequently become known as the Jaynes-Cummings model. Research in which the Jaynes-Cummings Hamiltonian plays a central role, generally referred to as cavity quantum electrodynamics (cavity QED), continues to fuel significant interest in quantum information science [92].

The coupling process results in 'dressed states' that have different resonant frequencies to the bare-atom and empty cavity. Consequently an atom inside the cavity disrupts the transmission of a probe laser, and observing changes in the cavity output field can be used to establish the presence of a single atom. The system has been demonstrated with a Fabry-Pérot cavity used to detect single atoms in a thermal atomic source [93, 70], as well as from a coherent matter wave

[104], and the possibility of cavity detection of single atoms using more exotic cavities has been investigated [122]. Outside their use as detectors for single atoms, optical cavities have been used to couple to relatively large ensembles, including BECs of several thousand atoms [24, 118], as well as to demonstrate 'optomechanics' in macroscopic components whose behaviour is described in the quantum regime [24, 142, 65, 86]. The motion of atoms within the cavity mode has been observed [42, 101, 72], and several groups have investigated the phenomenon of Vacuum Rabi splitting, using optical, microwave and solid-state cavities coupled to a variety of two-state systems [136, 94, 81, 67].

Cavities are not the only possibility for atomic detection. Broadly speaking, the options available can be divided into two categories: optical and physical detection. Optical detection (of which cavities are an example) relies on observations of light fields that are in some way associated with the presence of an atom, while physical detection measures an atom when it makes contact with some other material component that is a part of the detector.

Probably the most common technique used in experimental set-ups for atom detection is absorption imaging. While free-space absorption imaging is a reliable and relatively straight-forward process, it is generally only appropriate for sufficiently optically deep atomic samples, and is not a favourable option for single atom detection [91]. Single molecules *have* been observed with this technique [51] but only with long integration times; ruling out high bandwidth detection.

One of the most theoretically simple (though often technically challenging) optical detection schemes is fluorescence detection, which measures spontaneously emitted photons from an atom in the detection region. Single atoms at well determined optical lattice sites have been observed with fluorescence detection [87], as has the direct measurement of sub-Poissonian statistics in a trapped BEC [33]. Provided the photon detection optics account for a sufficient numerical aperture surrounding the atom-detection region, the fluorescence signal can be strong [7]. If this is not the case, or the background counts are too high, atoms need to be many [129, 137], or trapped on the order of $100\mu s$ [87, 33, 55], to acquire high signal-to-noise ratios. For atoms trapped in a 2D optical lattice, imaging of macroscopic atomic ensembles with single-atom resolution and impressive sensitivity has been achieved using very high numerical aperture fluorescence imaging [14, 131]. These 'quantum gas microscopes' achieve near unity fidelity in their atom detection, although the necessary exposure times are long; typically between 200 and 1000 ms. Fast detection times for single atoms have been achieved using an integrated chip/detector scheme [145]. Although practically very different, of the current available detection techniques, fluorescence detection is the most comparable candidate to cavity detection. The two approaches have even be used in a single integrated set-up [55], but there has yet to be a thorough investigation that compares the merits - practical and theoretical - of high efficiency single-atom detection based on each of these mechanisms.

An example of physical detection of quantum degenerate gases has been demonstrated with the use of microchannel plates (MCP) for metastable helium and neon [127, 143, 115]. A metastable atom in a highly excited and long-lived state possesses a very large internal energy. On impact with a conducting surface, the atom falls to its ground state and the energy is used to eject electrons from the surface. The electron pulse can be accelerated, multiplied and detected with good signal-to-noise ratio allowing single atom counting [125, 107, 148].

Neutral ground-state atoms do not have enough energy for this process. Instead, converting neutral atoms to ions, *via* photoionisation, allows improved detection efficiency, since ions have a lot of energy, and are relatively easy to detect [29]. Alternatively, the principles of a scanning electron-microscope have been employed on a cold, trapped quantum gas, to observe single atoms with a resolution on the order of hundreds of nanometers, by first ionising the atoms with an electron beam (rather than the photon beam used in photoionisation), and subsequently detecting the ions [52].

A note on terminology: In the literature covering single atom detection research, there is some ambiguity surrounding the relevant measures of a good detector. It is important to distinguish between the detection *quantum efficiency*, and what I will term *fidelity*: In this work, by quantum efficiency I refer to the ratio of the number of detected quanta to the actual number of quanta that pass through the detection region in a given measurement time. Fidelity pertains to the reliability with which we can say that a detection signal was triggered by a real event, rather than a *dark* signal intrinsic to the detector. In the language of quantum optical photosensitive devices, the term *dark current* refers to the flow of electrons in the device, even when no photons are present. If this current is beyond a given threshold, it will contribute to false photon counts, thus limiting the fidelity of the device. Alternatively, if the quantum efficiency is low, then not every photon hitting the detector will result in a measurable flow of electrons. Both are important properties, although it is usually only possible to optimise one at the expense of the other. It is therefore advantageous to design a detector with its end purpose in mind, so as to choose and work towards its desired attributes.

1.4 Thesis structure

The work carried out for this thesis falls broadly into two categories: (1) The theoretical modelling of a cavity system with the goal to design a high quantum efficiency detector for single atoms in an atom laser beam. (2) The subsequent building and characterisation of an experimental set-up to implement the detection scheme. Each chapter begins with a brief discussion of the motivation for the work that is presented there, and a layout of the subsequent sections. The structure of the narrative is as follows:

- **Chapter 2** provides the necessary theoretical grounding or references to more detailed theoretical background for the remainder of the work, in particular for the discussions in chapters 3 and 4. It also provides an overview of the theoretical models of the two-level atom, optical cavity and their coupling, that are central to this work.

- **Chapter 3** is are concerned with a thorough analysis of the signal-to-noise ratio (snr) of the proposed single-atom detector. It investigates the many parameters that influence the quality of the detection, considering both the detection set-up and operation regimes.

- **Chapter 4** builds on the theoretical work on detection snr, and is concerned with deducing the quantum efficiency, dark-noise and noise-floor clearance of a practical detector and its ability to measure number squeezing in an atomic beam.

- **Chapter 5** gives an account of the experimental set-up. The principal components of the apparatus are covered, as well as the frequency-locking procedures that are employed and the data acquisition process.

- Results of our detection signal are presented in **chapter 6**. Various features of our atomic source are explored and compared with work by other authors.
- **Chapter 7** contains a summary of the theoretical and experimental work and some concluding remarks regarding the direction of future experiments.

Part I

Theory and Modelling

CHAPTER

TWO

BACKGROUND

The work that is discussed in this thesis pertains to the interaction between a single atom and a single mode of the electromagnetic field within an optical resonator. These are the two fundamental components of the detection system that we consider. This chapter contains a review of the models of these components, and details the quantum mechanical description of their interaction.

2.1 The Two-Level Atom

In Bohr's model, an atom possesses an infinite number of discrete energy levels[1] characterised by the principal quantum number n, with approximate values given by the relation:

$$E_n = -hcR_\infty \frac{Z_{\text{eff}}^2}{n^2}$$

Here the energy of each level is mostly due to the Coulomb interaction between bound electrons and the atom's nucleus. R_∞ is the Rydberg constant, h is Planck's constant, c the speed of light, and Z_{eff} is the effective nuclear charge that accounts for the shielding effect of inner-orbital electrons on the bare nuclear charge.

More subtle structure to the internal energy levels of the atom exists due to the interactions between the magnetic moments of the electrons' spin and orbital angular momenta (fine structure) as well as interactions of the nuclear spin with

---

[1] Although theoretically there are an infinite number of energy levels for any atom, in practice there will be a 'highest-bound-state' level. If an electron absorbs enough energy to be excited to a level above that state but not enough to escape, it will drop back down to an open orbital in a lower level and radiate one or more photons to carry away the extra energy.

the atomic fields (hyperfine structure). The mean field due to core electrons is a large effect; in alkali atoms, with only a single valence electron, the effect lifts the degeneracy in the orbital angular momentum quantum number l.

The atom we use is rubidium 87 - one of the alkali atoms that is relatively easily condensed to form BECs, and is consequently a popular choice in quantum-atom optics. Figure 2.1 shows the structure for the D2 energy levels in rubidium 87. The principle quantum number is $n = 5$, and the degeneracy of the orbital angular momentum states is lifted, leading to separate energy levels for the different l states, labelled **S** ($l = 0$) and **P** ($l = 1$).

Rather than modelling the atom using this set of unevenly-spaced energy levels, a two-level description may be valid when the driving field is only resonant (or close-to-resonant) with two of the energy levels, and far off resonance for all other transitions. If this is the case, the atomic model is analogous to a two-state, spin-1/2 system.

The lower of the two energy eigenstates, the ground state, may be labelled

$$|-\rangle = \begin{pmatrix} 0 \\ 1 \end{pmatrix},$$

the upper, or excited state,

$$|+\rangle = \begin{pmatrix} 1 \\ 0 \end{pmatrix}.$$

The operators that act to raise ($\hat{\sigma}_+ = |+\rangle\langle-|$) and lower ($\hat{\sigma}_- = |-\rangle\langle+|$) the atomic excitation between these levels are often referred to as 'pseudospin' operators. In the Schrödinger picture, the Hamiltonian for the bare atom is

$$\hat{H}_a = \hbar\omega_a|+\rangle\langle+| \equiv \hbar\omega_a\hat{\sigma}_+\hat{\sigma}_- \tag{2.1}$$

where $\hbar\omega_a$ is the energy difference between the two levels. Of course, the ground state energy is arbitrary, and an equally valid Hamiltonian that is often used is

$$\hat{H}_a = \frac{1}{2}\hbar\omega_a\left(|+\rangle\langle+| - |-\rangle\langle-|\right) \equiv \frac{1}{2}\hbar\omega_a\hat{\sigma}_z. \tag{2.2}$$

where $\hat{\sigma}_z$ is the atomic inversion operator, related to the raising and lowing operators *via*

$$\frac{1}{2}\hat{\sigma}_z = (\hat{\sigma}_+\hat{\sigma}_- - \hat{\sigma}_-\hat{\sigma}_+).$$

In the dipole approximation, the wavelength of a classical electromagnetic field interacting with the atom is much larger than the size of the atom. The mathematics used to describe the evolution of the two-level atom in the presence of such a field has parallels in other areas of theoretical physics: it is equivalent to that of a magnetic dipole in a magnetic field, and the dynamics of the atomic state is often represented on a 'Bloch sphere', analogous to the 'Poincaré sphere' that is used to represent polarisations of light. This type of representation will not be heavily used in this thesis, but is common in related literature. Detailed descriptions are given in, for example, references [47, 97].

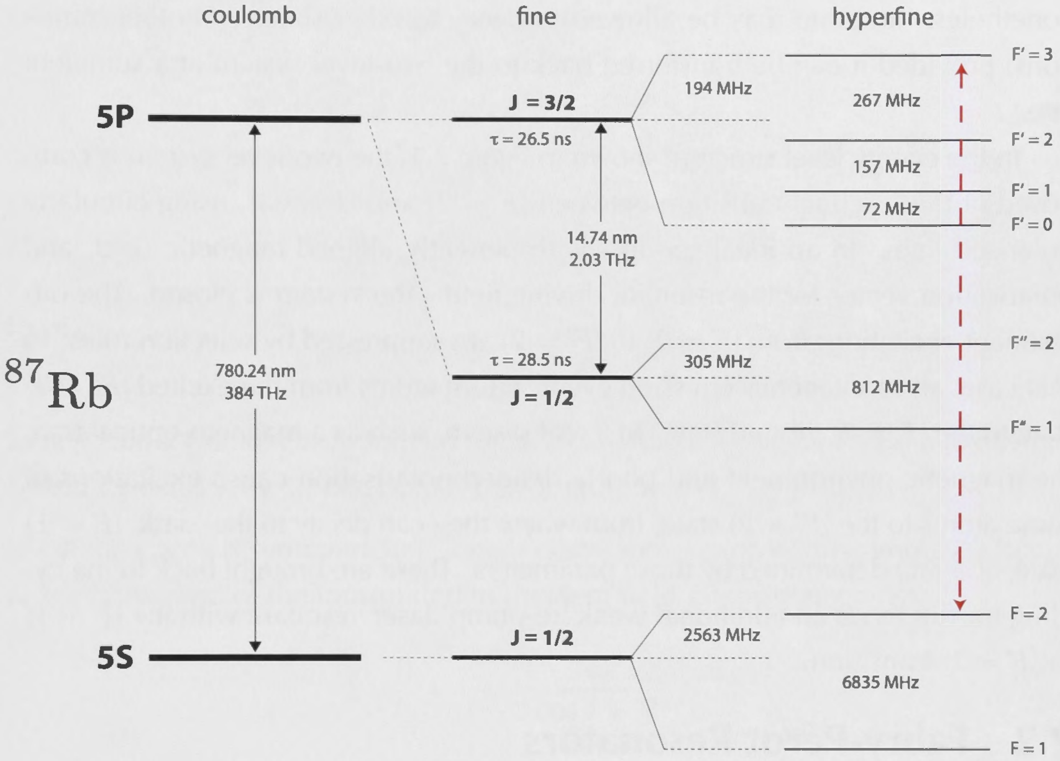

Figure 2.1: The fine, and hyperfine level structure of the ground and first excited states of rubidium 87. The red, dashed arrow indicates the two-level cycling transition.

The two-level systems that are used in experimental quantum-atom optics are diverse. They include neutral atoms [136], highly excited Rydberg atoms [112], molecules [35] and ions [34], as well as 'artificial atoms' such as quantum dots [81, 67, 149] and confined Cooper-pairs in super-conducting circuits [17]. In all cases, the validity of the two-level model requires that available photons are only resonant (or close-to-resonant) with one of many possible transitions. If this condition is not entirely satisfied, but one wishes to use the two-level model nonetheless, an atom may be allowed to decay to other states (*via* other transitions) provided it can be transferred back to the two-level system at a sufficient rate.

In the energy level structure shown in figure 2.1, the two-level system is composed of the 'cycling' transition between $|F = 2\rangle$ and $|F' = 3\rangle$, using circularly polarised light. In an ideal set-up - with perfectly aligned magnetic field, and polarisation vector for the resonant driving field - the system is closed. The off-resonant excitations from $|F = 2\rangle$ to $|F' = 2\rangle$ are suppressed by selection rules. In that case, all spontaneous emission events return atoms from the excited $|F' = 3\rangle$ state to the $|F = 2\rangle$ ground state. In a real system, such as a magneto-optical trap, the magnetic environment and poorly defined polarisation cause excitations of some atoms to the $|F' = 2\rangle$ state, from where they can decay to the 'dark' $|F = 1\rangle$ state, at a rate determined by those parameters. These are brought back to the cycling transition *via* an additional weak 're-pump' laser, resonant with the $|F = 1\rangle$ to $|F = 2\rangle$ transition.

2.2 Fabry-Pérot Resonators

2.2.1 Longitudinal Modes

Many different systems have been used to isolate and trap photons in different frequency regimes. Useful cavity fields range from the whispering gallery modes of toroidal structures and microresonators [123, 128, 126], to those of resonators using Bragg mirrors in the optical realm [104, 71], polished mirror mircowave cavities [96, 94], as well as semiconductor heterostructures [81, 67], microwave circuits [141], and defects in nano-fabricated photonic crystals [149]. A review of much of the varied work that has been carried out using optical cavities is given in reference [139].

The cavity used in the work presented in this thesis was a Fabry-Pérot resonator, shown schematically in figure 2.2. This is one of the simplest types of cavity to analyse, and a classical treatment, considering the complex amplitudes of self-reproducing waves, is given in many undergraduate optics texts (see, for example, reference [124]). Maxwell's equations, and the boundary conditions introduced by the cavity mirrors, place restrictions on the spatial properties of the electromagnetic field, and lead to reflected and transmitted fields, E_r and E_t, that are related to the input field, E_0, and the phase, δ, accumulated in a round-trip of the cavity, with the following expressions:

$$\frac{E_r}{E_0} = r_1 + t_1^2 r_2 e^{-i\delta}\left(\frac{1}{1 - r_1 r_2 e^{-i\delta}}\right) \tag{2.3}$$

$$\frac{E_t}{E_0} = t_1 t_2 e^{-i\delta/2}\left(\frac{1}{1 - r_1 r_2 e^{-i\delta}}\right). \tag{2.4}$$

Here

$$\delta = 4\pi L/\lambda$$

for a resonator of length L, formed by an input mirror with amplitude reflectivity r_1 and transmissivity t_1, and output mirror of r_2, and t_2.

If the cavity is symmetric ($r_1 = r_2 = r$) the above expressions simplify. Using $\mathcal{R} = r^2$, the ratio of the transmitted to incident field intensity becomes:

$$\frac{I_t}{I_0} = \frac{(1-\mathcal{R})^2}{1 - 2\cos\delta + \mathcal{R}^2}$$

It is usual to rewrite this expression as

$$\frac{I_t}{I_0} = \frac{1}{1 + (2\mathscr{F}/\pi)^2 \sin^2(\delta/2)} \tag{2.5}$$

where $\mathscr{F}$ is a parameter known as the *finesse*. For a perfect cavity, with no intracavity losses, the finesse is determined completely by the quality of the cavity mirrors:

$$\mathscr{F} = \frac{\pi\mathcal{R}^{1/2}}{1-\mathcal{R}}.$$

The transmitted field intensity is clearly a periodic function of the round-trip phase [equation (2.5)], as shown in figure 2.3, and consequently depends on the wavelength of light used and its relation to the cavity length. Each time the length is changed by one half wavelength, a new peak in transmission is scanned.

Operating *on resonance* then, we are restricted to standing waves whose

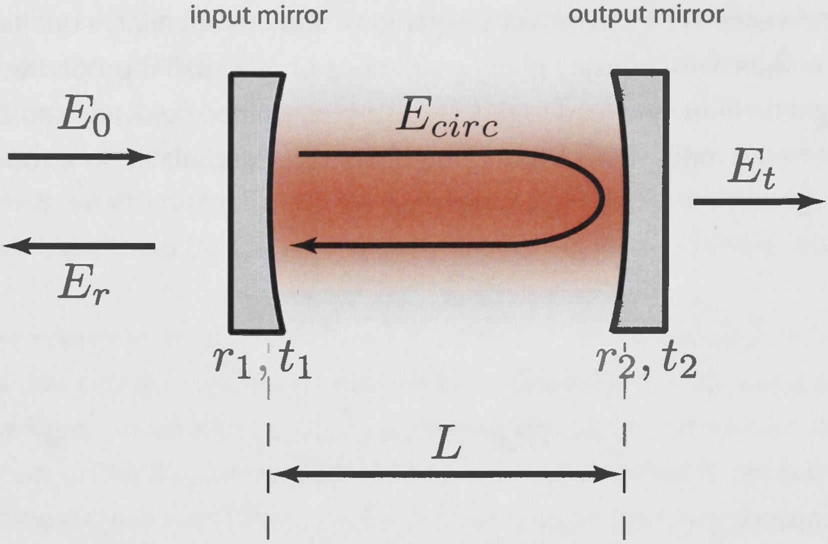

Figure 2.2: Schematic diagram of a Fabry-Pérot cavity showing input, E_0, reflected, E_r, circulating, E_{circ} and transmitted, E_t fields.

wavelengths are defined by the cavity length,

$$2L = n\lambda \tag{2.6}$$

Consequently, the resonant frequencies of the field take discrete values given by

$$\nu = \frac{nc}{2L} \tag{2.7}$$

where n is the number of nodes in the standing-wave, and each n defines a different longitudinal mode of the field. There is a constant frequency difference between adjacent resonator modes, n and $n-1$, known as the free spectral range

$$\nu_{FSR} = \frac{c}{2L}. \tag{2.8}$$

From (2.5), the full-width at half the maximum intensity (FWHM), $\Delta\nu$, of each resonance can be found, and the finesse measures the ratio of the free spectral range to the width of a resonance:

$$\mathscr{F} = \frac{\nu_{FSR}}{\Delta\nu}. \tag{2.9}$$

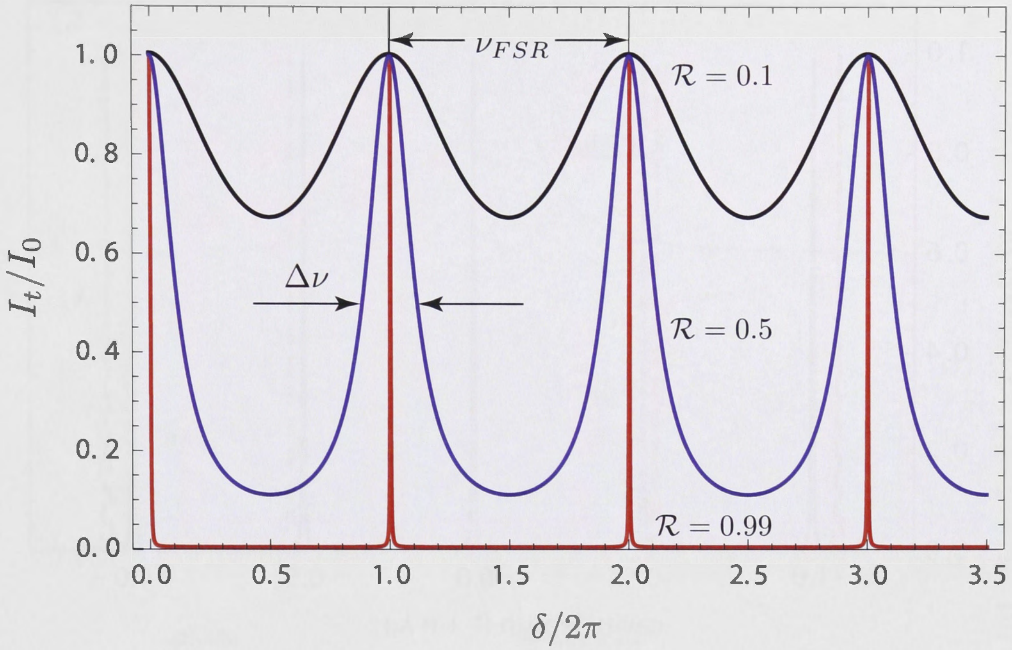

Figure 2.3: Fabry-Pérot transmission intensity [equation (2.5)] over three free spectral ranges, for a cavity formed with mirrors of poor to good reflectance $R = r^2 = 0.1, 0.5$ and 0.99.

With the relations given, it becomes apparent that two different frequencies will be resonant in the same cavity mirrors at different cavity lengths, as indicated in figure 2.4.

In this figure, the abscissa is parameterised in wavelengths, λ_1, so the resonant lengths do not always coincide; this is precisely because the free-spectral-range measures the occurrence of each new half-wavelength between the cavity mirrors. Attaining 'co-resonance' - that is, a cavity length for which two wavelengths are both resonant - is covered in the discussion of our experimental set-up in chapter 5.

It can be useful to consider the response of the cavity in terms of the phase shift on the probe beam instead of changes in intensity. In figure 2.5, we show a cavity response in terms of both these observables, as a function of the cavity linewidth, κ. The phase of the field defined with equation (2.4) is given by $\Phi = arg[\mathbf{E}]$ while the intensity is $I = \mathbf{E}^* \cdot \mathbf{E}$.

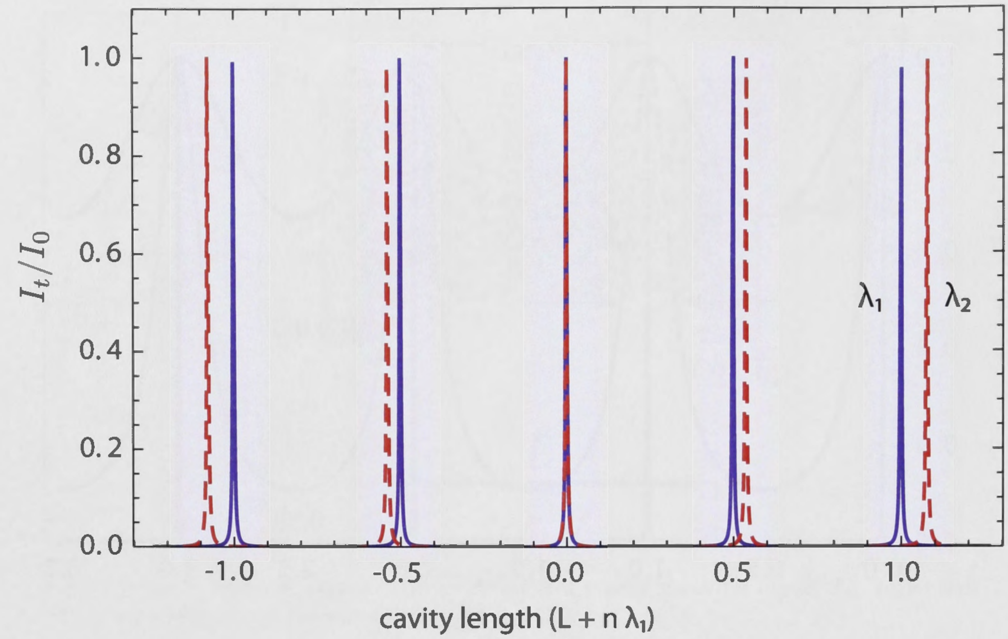

Figure 2.4: Resonant positions for two different frequencies for a cavity finesse of 100. The cavity length is varied about a length, L, at which both wavelengths are resonant.

2.2.2 Transverse Modes

The discussion given above considers the confinement of the field along the cavity axis. When planar-mirrors are used, this confinement is only marginally stable. That is to say that a small misalignment of the mirrors, or incoming beam with respect to the mirrors, will result in reflections for which the rays are not self-reproducing, and eventually leave the bounds of the (finite) mirrors. Concave spherical-mirror cavities are constructed using two spherical mirrors with radii of curvature R_1 and R_2, and can be made fully stable. The limits to the resonator stability are the cases of the planar-mirror cavity, for which $R_1 = R_2 = \infty$, and the 'symmetric concentric' cavity for which $R_1 = R_2 = L/2$. Between these limits cavities are considered stable. In a ray-optics model, misalignment of a stable cavity results in beam paths that are self-reproducing, but may require more than one round trip before this condition is met.

The boundary conditions imposed on the electromagnetic field in spherical-mirror cavities result in resonant beams that are described by the infinite set of Hermite-Gaussian modes [124]. These modes are defined by three independent

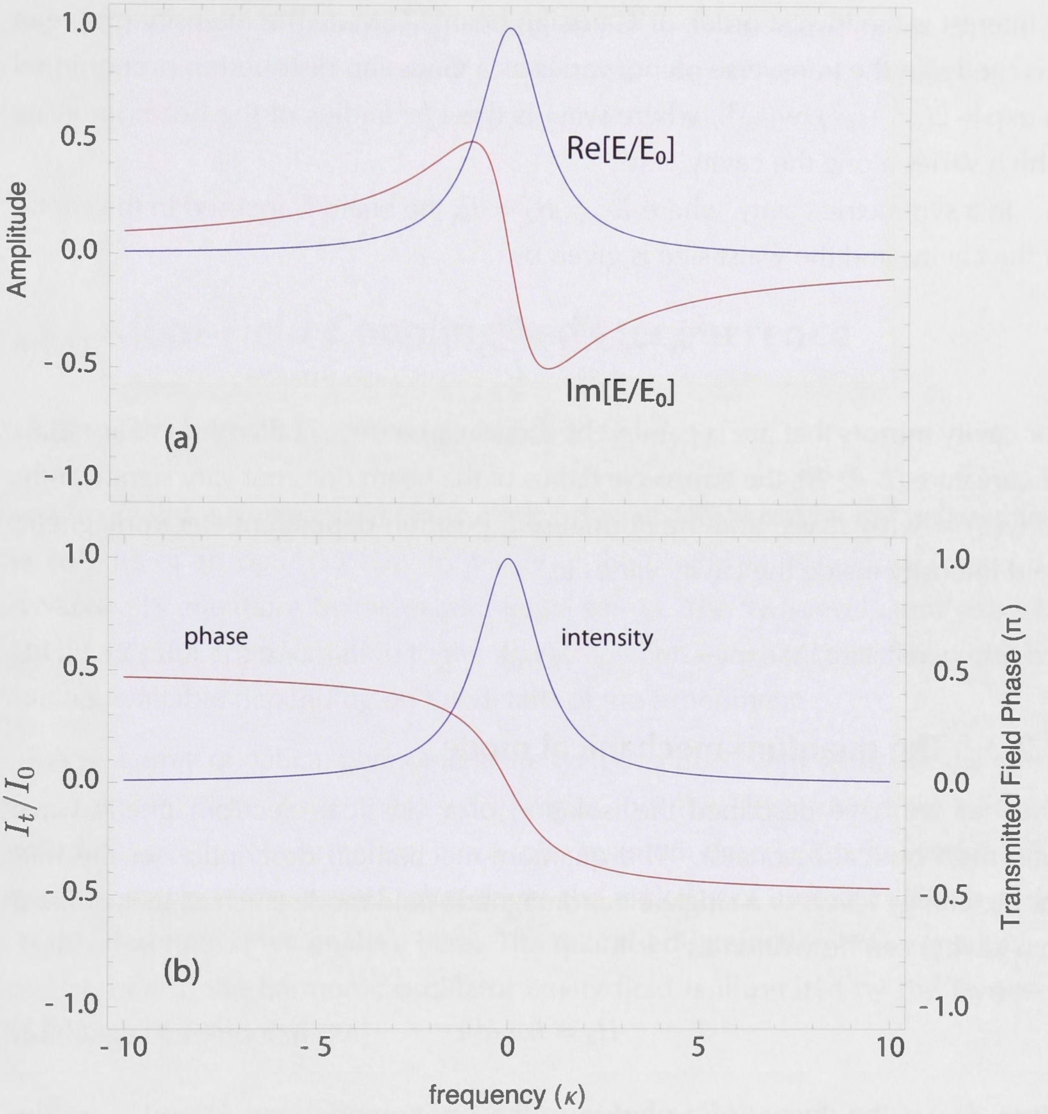

Figure 2.5: Response of a symmetric optical resonator ($r_1 = r_2$). Figure (a) shows the real and imaginary components of the transmitted field, **E**, and (b) shows the transmitted intensity $I = \mathbf{E}^* \cdot \mathbf{E}$ and phase response, $\Phi = arg[\mathbf{E}]$.

integers, (l, m, n) describing the intensity distribution of the field. The integers l and m characterise the beam profile in the transverse plane, while n defines the order of the longitudinal modes, as discussed previously. The transverse modes are commonly labelled and referred to as TEM$_{lm}$ (transverse electromagnetic). In specific experimental circumstances, higher order modes are used (see for example, references [75, 95, 130, 152]) but typically, as in the present work, the mode of interest is the lowest order, or Gaussian beam: TEM_{00}. The intensity profile of this mode, in the transverse plane, varies as a Gaussian distribution proportional to $\exp\left[-2(x^2+y^2)/\text{w}(z)^2\right]$, where $\text{w}(z)$ is the $1/e^2$ radius of the beam intensity which varies along the cavity axis.

In a symmetric cavity, where $R_1 = R_2 = R$, the beam is focused in the centre of the cavity, and the waist size is given by

$$\text{w}_0^2 = \frac{\lambda L}{2\pi}(2\frac{|R|}{L} - 1)^{1/2} \tag{2.10}$$

For cavity mirrors that are separated by a distance much smaller than their radius of curvature ($L \ll R$), the transverse radius of the beam does not vary significantly, so $\text{w}(z) \approx \text{w}(0) \equiv \text{w}_0$, and the normalised, position-dependent electromagnetic field intensity inside the cavity varies as

$$I(\boldsymbol{r}) = \cos^2(2\pi z/\lambda)\exp(-2(x^2+y^2)/\text{w}_0^2) \qquad -L/2 \leqslant z \leqslant L/2 \tag{2.11}$$

2.2.3 The quantum-mechanical mode

Thus far we have described the isolation of a classical electromagnetic wave within an optical resonator. The quantum-mechanical description of the harmonic energy levels of a single electromagnetic field mode (such as that isolated in a cavity) can be written as[2]

$$\hat{H}_c = \hbar\omega_c \hat{a}^\dagger \hat{a} \tag{2.12}$$

Here, $\hbar\omega_c$ is the energy of a photon of the cavity mode, and $\hat{a}^\dagger$ and $\hat{a}$ are the creation and annihilation operators that add or remove photons:

$$\hat{a}|n\rangle = \sqrt{n}|n-1\rangle$$

$$\hat{a}^\dagger|n\rangle = \sqrt{n+1}|n+1\rangle,$$

They obey the commutation relation $[\hat{a}, \hat{a}^\dagger] = 1$, and together give the photon number-operator $\hat{n} = \hat{a}^\dagger\hat{a}$.

The classical intra-cavity intensity scales with the number of intra-cavity pho-

---

[2] We ignore the zero point energy conventionally included in the Hamiltonian of the harmonic field operator since it will not be important for the coupled system to be discussed shortly.

tons, and the single-photon energy density is simply the photon energy, $\hbar\omega_c$, divided by the cavity mode volume, V_m. The mode volume is found by integrating the cavity mode [equation (2.11)] over all three spatial dimensions:

$$V_m = \frac{1}{4}\pi \mathrm{w}_0^2 L$$

2.3 Atom-Field Coupling and Decoherence

2.3.1 The Jaynes-Cummings Model

Experimentally, a single mode of the electromagnetic field can be isolated within the volume of an optical cavity by virtue of the boundary conditions imposed on Maxwell's equations by the experimental set-up. The 'two-level atom' model may be a useful approximation to the real system, or a very accurate description of states available depending on the details of the experiment.

A vast array of optical phenomena are well described with semiclassical theory, in which atoms have quantised energies, but the electromagnetic field is treated classically. Nevertheless, it is a fully quantum description that yields the novel dynamics of cavity QED that drives the majority of current research and it is this description we analyse here. The quantised interaction between a two-level atom and the harmonic-oscillator cavity field is illustrated by the Jaynes-Cummings Hamiltonian [76]

$$\hat{H} = \hbar\omega_a \hat{\sigma}_+ \sigma_- + \hbar\omega_c \hat{a}^\dagger \hat{a} + \hbar g(\boldsymbol{r})(\hat{\sigma}_+ + \hat{\sigma}_-)(\hat{a} + \hat{a}^\dagger). \tag{2.13}$$

The first term describes the excitation of the two-level atom with atomic energy spacing, $\hbar\omega_a$, while the second tells us the occupation of the cavity mode with equally-spaced energy levels separated by $\hbar\omega_c$. Here $\hbar$ is Plank's constant divided by 2π, and ω_i is the resonant frequency of the system, i: either the atom (when $i = a$) or cavity (when $i = c$). The third term describes the coupling between the atomic electric dipole and the electric field of the cavity mode. This is not to be confused with the coupling of the composite system to external reservoir modes, that will be discussed in the following section.

The strength of the interaction is determined by the size of the dipole moment,

$\boldsymbol{\mu}$, and the strength of the field, $\boldsymbol{E}(\boldsymbol{r})$:

$$\hbar g(\boldsymbol{r}) = \boldsymbol{\mu} \cdot \boldsymbol{E}(\boldsymbol{r}) \tag{2.14}$$

Values for the magnitudes of the atomic dipole matrix elements of various transitions can be found in literature [134], and the directions of $\boldsymbol{\mu}$ and $\boldsymbol{E}(\boldsymbol{r})$ are determined by their polarisation. $\boldsymbol{E}(\boldsymbol{r})$ is time-independent since it is a standing wave within the cavity. With the appropriate magnetic environment and polarisation of the field, the two can be aligned to give the maximum coupling constant. If this is not the case, it may be necessary to use an average value for the atomic dipole matrix element as it precesses about the field axis.

The Interaction Picture

If we consider the system is driven by a field with frequency ω_0, it can be useful to re-write the Hamiltonian (2.13) as

$$\hat{H} = \underbrace{\hbar\omega_0 \hat{a}^\dagger \hat{a} + \hbar\omega_0 \hat{\sigma}_+ \hat{\sigma}_-}_{\hat{H}_0} + \underbrace{\hbar\Delta_c \hat{a}^\dagger \hat{a} + \hbar\Delta_a \hat{\sigma}_+ \hat{\sigma}_- + \hbar g(\boldsymbol{r})(\hat{\sigma}_+ + \hat{\sigma}_-)(\hat{a} + \hat{a}^\dagger)}_{\hat{V}}$$

where

$$\Delta_a = \omega_0 - \omega_a$$

and

$$\Delta_c = \omega_0 - \omega_c$$

represent the detunings of the the uncoupled systems from the driving field.

We transform to a frame rotating with the driving field using

$$\hat{H}_{\text{sys}} = U_0^\dagger \hat{V} U_0;$$

$$U_0 = e^{-i(\hat{H}_0)t/\hbar}$$

and the Hamiltonian for the Jaynes-Cummings system in the interaction picture becomes:

$$\hat{H}_{sys} = \hbar\Delta_c \hat{a}^\dagger \hat{a} + \hbar\Delta_a \hat{\sigma}_+ \hat{\sigma}_- + \hbar g(\boldsymbol{r})(\hat{a}\hat{\sigma}_+ + \hat{a}^\dagger \hat{\sigma}_- + e^{2i\hbar\omega_0} \hat{\sigma}_+ \hat{a}^\dagger + e^{-2i\hbar\omega_0} \hat{\sigma}_- \hat{a}).$$

The Rotating Wave Approximation

In the rotating frame, the terms $\hat{\sigma}_+\hat{a}^\dagger$ and $\hat{\sigma}_-\hat{a}$ acquire a time dependence, that is very fast compared to the other relevant rates in the system. Equation (2.15) employs the *rotating wave approximation* where these terms have been dropped. We can see that the coupling term is now energy conserving, so that the annihilation of a photon in the cavity mode *via* the operator a is always accompanied by the raising of the atomic energy with $\hat{\sigma}_+$, and *vice versa*.

$$\hat{H}_{sys} = \hbar\Delta_c\hat{a}^\dagger\hat{a} + \hbar\Delta_a\hat{\sigma}_+\hat{\sigma}_- + \hbar g(\boldsymbol{r})(\hat{a}\hat{\sigma}_+ + \hat{a}^\dagger\hat{\sigma}_-) \tag{2.15}$$

2.3.2 The Master Equation

In the absence of dissipation, the Jaynes-Cummings model (2.15) can be solved exactly, however such a simplification brings limitations. A more accurate model includes the dissipation of energy that occurs both as a result of spontaneous emission from the excited state of the two-level atom into modes other than the cavity mode and the loss of photons from the cavity mode *via* transmission, scattering and absorption in the mirrors. When these dissipative processes are added to the Jaynes-Cummings model, the system dynamics are found using solutions to the *master equation*.

A complete derivation of the master equation is a lengthy process, and is covered well in a number of quantum optics textbooks. A particularly thorough derivation is given by Doherty and Mabuchi in *Optical Microcavities*, [139]. Here I will present a summary of that derivation since it is satisfying to see the origin of the equation that is central to the modelling work in this thesis.

The purpose of the master equation is to analyse the evolution of an open quantum system, that is, one which is not isolated from its environment. The environment is modelled as an infinite reservoir, or bath, connected weakly to the system *via* an interaction Hamiltonian, $\hat{H}_{int}$, so that the complete Hamiltonian may be represented as $\hat{H}_{tot} = \hat{H}_{sys} + \hat{H}_b + \hat{H}_{int}$, where $\hat{H}_{sys}$ is the Hamiltonian of the system and $\hat{H}_b$ is that of the bath. In the Schrödinger picture, the total density operator for the system and bath together, obeys the usual Hamiltonian dynamics:

$$\dot{\rho}_{tot} = -\frac{i}{\hbar}[\hat{H}_{tot}, \rho_{tot}]. \tag{2.16}$$

However, with this approach we wish to derive information about the system only, by tracing out the many degrees of freedom of the bath. We are interested, therefore, in the *reduced density operator*,

$$\rho(t) = \mathrm{Tr_b}\left\{\rho_{tot}(t)\right\}. \tag{2.17}$$

By transforming first to the interaction picture, (2.16) becomes

$$\dot{\rho}_I = -\frac{i}{\hbar}[\hat{H}, \rho_I] \tag{2.18}$$

and the reduced density matrix in the interaction picture is

$$\rho(t) = \mathrm{Tr_b}\left\{\rho_I(t)\right\}. \tag{2.19}$$

Here

$$\rho_I = U_0^\dagger \rho U_0$$

$$\hat{H} = U_0^\dagger \hat{H}_{int} U_0$$

with the transformation matrix

$$U_0 = e^{-i(\hat{H}_{sys}+\hat{H}_b)t/\hbar}.$$

To find a solution to (2.18), we first integrate from 0 to t to obtain:

$$\rho_I(t) = \rho(0) + \frac{-i}{\hbar}\int_0^t [\hat{H}(t_1), \rho_I(0)]\, dt_1$$

A second iteration gives:

$$\rho_I(t) = \rho_I(0) + \frac{-i}{\hbar}\int_0^t [\hat{H}(t_1), \rho_I(0)]\, dt_1 + (\frac{-i}{\hbar})^2 \int_0^t \int_0^{t_1} [\hat{H}(t_1), [\hat{H}(t_2), \rho_I(t_2)]]\, dt_1 dt_2.$$

Now differentiating with respect to t,

$$\dot{\rho}_I(t) = -\frac{i}{\hbar}[\hat{H}(t), \rho_I(0)] + (\frac{-i}{\hbar})^2 \int_0^t [\hat{H}(t), [\hat{H}(t_1), \rho_I(t_1)]]\, dt_1. \tag{2.20}$$

We now make several key assumptions:

- We assume that the system and bath are only weakly correlated at an initial time, t_0, when the interaction and Schrödinger pictures coincide, so that the total density operator can be factored into a direct product:

  $$\rho_I(0) = \rho_{tot}(0) = \rho(0) \otimes \rho_b$$

  Also, if the reservoir is sufficiently large, its statistical properties are not changed by the system-reservoir coupling, and its density matrix, ρ_b is essentially time-independent.

- We choose the interaction Hamiltonian such that it has no diagonal elements in the basis in which $\hat{H}_b$ is diagonal. These assumptions allow us to conclude

  $$\mathrm{Tr}_b \left\{ \hat{H}(t) \rho_I(0) \right\} = 0, \tag{2.21}$$

  and so, taking the trace over the bath variables, for both sides of (2.20), and making use of the identity (2.19):

  $$\dot{\rho}(t) = -\frac{1}{\hbar^2} \int_0^t \mathrm{Tr}_b \left\{ [\hat{H}(t), [\hat{H}(t_1), \rho_I(t_1)]] \right\} dt_1. \tag{2.22}$$

- The *Born approximation*: If the interaction between the bath and system is much weaker than any interactions between components *within* the bath or system (in other words, V is very much less than $\hat{H}_{sys}$ or $\hat{H}_b$), then we can legitimately replace $\rho_I(t_1)$ with the approximation $\rho_I(t_1) \approx \rho(t_1) \otimes \rho_b$ in the above expression.

- We note that for the weak interaction assumption, the rate of change of the system density matrix (in the interaction picture), will be much slower than that of the bath operators, and so the term $\rho(t_1)$ changes insignificantly over the relevant correlation time, t of (2.22). Thus we set $\rho(t_1) \to \rho(t)$ to obtain:

  $$\dot{\rho}(t) = -\frac{1}{\hbar^2} \int_0^t \mathrm{Tr}_b \left\{ [\hat{H}(t), [\hat{H}(t_1), \rho(t) \otimes \rho_b)]] \right\} dt_1. \tag{2.23}$$

  Finally we recognise that there is a remaining rate to consider - the thermal correlation time, τ - that measures the speed at which energy is dissipated within the bath modes. When this is much faster than the speed at which it is coupled back into the system ($t \gg \tau$), the system is described as having a 'short memory'. If this is the case we can change the limits of the time integral as follows to conclude:

$$\dot{\rho}(t) = -\frac{1}{\hbar^2}\int_0^\infty \mathrm{Tr}_b\left\{[\hat{H}(t),[\hat{H}(t-\tau),\rho(t)\otimes\rho_b)]]\right\}dt_1. \tag{2.24}$$

This final set of assumptions is known as the *Markov approximation*, and the final equation at which we have arrived (2.24) is a common form of the master equation.

Master Equation for the Atom-Cavity System

For the system at hand, we have

$$\hat{H}_{tot} = \hat{H}_{sys} + \hat{H}_b + \hat{H}_{int}$$

where $\hat{H}_{sys}$ is the Jaynes-Cummings Hamiltonian given by equation (2.15).

The bath in this case is an infinite set of harmonic oscillators, $\hat{b}(\omega)$ that constitutes the electromagnetic field modes of the environment:

$$\hat{H}_b = \hbar\int_{-\infty}^{\infty}\omega\hat{b}^\dagger(\omega)\hat{b}(\omega)\,d\omega.$$

The bath is coupled to this system *via* two processes: (1) the spontaneous decay of the atomic excited state to a mode outside the cavity, dissipating at a rate γ, and (2) the loss of photons through the cavity mirrors, with dissipation operator $\kappa\hat{a}$.

$$\hat{H}_{int} = i\hbar\int_{-\infty}^{\infty}\gamma[\hat{b}^\dagger(\omega)\hat{\sigma}_- - \hat{\sigma}_+\hat{b}(\omega)]\,d\omega + i\hbar\int_{-\infty}^{\infty}\kappa[\hat{b}^\dagger(\omega)\hat{a} - \hat{a}^\dagger\hat{b}(\omega)]\,d\omega.$$

Here we have again employed the rotating wave approximation used in the coupling term of equation (2.15), this time for the interaction of the system with the modes outside the cavity. Note that both γ and κ are *field* (or amplitude), rather than intensity (number) decay rates, although the linewidths that are observed in typical experimental scenarios measure intensity decay rates.

With the appropriate substitutions, the master equation for the damped atom-cavity system can be found:

$$\begin{aligned}\frac{d}{dt}\rho(t) = \quad & -\frac{i}{\hbar}[\hat{H},\rho] + \frac{\kappa}{2}(2\hat{a}\rho\hat{a}^{\dagger} - \hat{a}^{\dagger}\hat{a}\rho - \rho\hat{a}^{\dagger}\hat{a}) \\ & +\frac{\gamma}{2}(2\hat{\sigma}_{-}\rho\hat{\sigma}_{+} - \hat{\sigma}_{+}\hat{\sigma}_{-}\rho - \rho\hat{\sigma}_{+}\hat{\sigma}_{-}) \end{aligned} \tag{2.25}$$

The master equation can be solved to find the evolution of the (reduced) density matrix ρ, and expectation values for system operators can subsequently be determined using the density-operator relation:

$$\langle\hat{O}\rangle = \mathrm{Tr}\left\{\rho\hat{O}\right\}.$$

This is the procedure employed in our detection modelling discussed in the following chapter.

2.3.3 A Pumped Cavity: The Driven Jaynes-Cummings Hamiltonian

The Jaynes-Cummings Hamiltonian *with* dissipation necessarily leads to a depletion of photons from the cavity mode; the photon number decays via loss through the cavity mirrors and atomic spontaneous emission. In practice, most experiments drive the cavity mode with a laser field providing constant power at the input mirror that replenishes photons lost from the system. This allows us to find a steady-state for the density matrix (2.25) by including a constant pump term.

The Hamiltonian we use is the *driven* Jaynes-Cummings Hamiltonian:

$$\hat{H} = \hbar\Delta_c\hat{a}^{\dagger}\hat{a} + \hbar\Delta_a\hat{\sigma}_{+}\hat{\sigma}_{-} + \hbar g(\tilde{r})(\hat{a}\hat{\sigma}_{+} + \hat{a}^{\dagger}\hat{\sigma}_{-}) + \hbar\varepsilon(\hat{a} + \hat{a}^{\dagger}). \tag{2.26}$$

The pump-rate is related to the incident power and the transmissivity of the input mirror. For a resonant cavity, with intracavity photon number, n_{res}

$$\varepsilon^2 = n_{\mathrm{res}}\kappa^2$$

If, without changing the pumping rate ε, the cavity is detuned, then the intracavity photon number n_0 will reduce

$$\begin{aligned}
n_0 &= \frac{n_{\text{res}}}{1+(\dfrac{\Delta}{\kappa})^2} \\
&= \kappa^2 \frac{n_{\text{res}}}{\kappa^2+\Delta^2} \\
&= \varepsilon^2 \frac{1}{\kappa^2+\Delta^2} \\
\therefore \varepsilon &= \sqrt{n_0(\kappa^2+\Delta_c^2)}.
\end{aligned} \tag{2.27}$$

CHAPTER

THREE

SINGLE-ATOM DETECTION

The first step to analysing the value of an optical cavity as a single-atom detector, is to consider the best possible single-to-noise ratio that one could expect for optimal detection conditions. There are other metrics that are necessary to consider in the analysis but they are often considerably dependent on the style of detection used (for example, detection *time* may be an important factor in some atom number measurements, but is one that is not taken into consideration at all in absorption and MCP measurements). Signal-to-noise and fidelity are universal figures of merit, useful when comparing different types of detection. In the following chapter, we present a thorough analysis of signal atom detection using optical cavities.

Much of this chapter has been published as reference [110]: R. Poldy, B. C. Buchler, J. D. Close, *Single-atom detection with optical cavities*, Physical Review A, 2008 volume 78 (1). A large set of parameters that influence the signal-to-noise ratio for cavity detection is considered, with an emphasis on detunings, probe power, cavity finesse and photon detection schemes. Real device operating restrictions for single photon counting modules and standard photodiodes are included in our discussion, with heterodyne detection emerging as the clearly favourable technique, particularly for detuned detection at high power.

The cavity detection process has been considered in several previous studies. Work by Horak *et al.* investigates optical cavity detection of single atoms using microcavities [73]. The authors use a semiclassical model to analyse the signal-to-noise ratio of cavity based detection for a variety of parameters. Pinkse *et al.*

use a quantum model to calculate the signal-to-noise ratio for an atom passing through a cavity [109]. They consider a broader range of detection regimes, exploring the effect of the detuning of the probe laser independently from both the empty-cavity resonance (cavity-probe detuning) and bare-atom resonance (atom-probe detuning). However, their results do not consider variation of the probe power, since they are interested in the single atom *and single photon* regime that is the usual focus of cavity quantum-electrodynamics (QED) experiments.

Here we engage in a more complete investigation that thoroughly explores the detection 'parameter space'. We analyse the signal-to-noise ratio of cavity single atom detection by providing contour plots for the signal-to-noise ratio as a function of cavity finesse, probe laser intensity, cavity-probe detuning, and atom-probe detuning. The goal is to provide detailed information for the design and implementation of cavity based single atom detection that is appropriate for given requirements of quantum efficiency and detection bandwidth. This is the only investigation that covers such a complete range of parameters for this technology.

3.1 Introduction

Figure 3.1 is a schematic representation of a possible measurement process for cavity detection of single atoms. A shot-noise limited probe laser is transmitted through an empty cavity and the power is measured. A detection signal is observed when an atom falls through the cavity, interacting with the field and causing, for example, a reduction in transmitted power, as shown in the hyperthetical data of figure 3.1(b). The interaction may also be measured in other ways such as a phase shift in the probe beam, or an *increase* in transmitted power, and these possibilities are discussed in later sections of this chapter.

Cavity QED is generally separated into two parameter regimes, those of strong and weak coupling. These define the relative strengths of coupling *within* the system compared to the coupling of the system to external reservoir modes. 'Strong coupling' refers to systems in which the processes of interest are largely determined by the atom-field dipole coupling rate, g_0; it is this regime that has attracted much of the consideration in cavity QED. Consequently, recent investigations and experimental designs have, for the most part, been restricted to those that achieve the required strong coupling conditions. The focus of the present work is not to investigate properties of the strong coupling regime, but to analyze the cavity de-

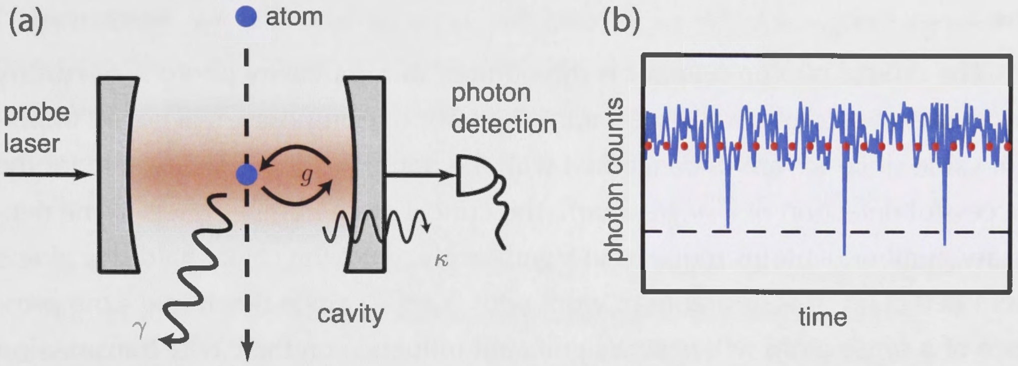

Figure 3.1: Single atom detection with an optical cavity showing (a) schematic diagram of cavity set-up. (b) typical photon counts for a detection event. The dashed line indicates the threshold for an atom detection event.

tection process in order to determine the best designs and operating conditions for high quantum efficiency single atom detection. We show that many (although not all) of the same features of strong-coupling experiments are necessary for a good signal-to-noise ratio in single atom detection. It is therefore worth clearly defining this regime.

For strong coupling, the exchange of energy within the system occurs on a time scale much shorter than other processes, so that $g_0 > \max[\Gamma, T^{-1}]$, where Γ is the set of decoherence rates for the system, and T is the interaction time. In the atom-cavity system, $\Gamma = \{\gamma, \kappa\}$ with γ the rate of decay of the atomic dipole, and κ that of the cavity field, as defined in chapter 2. To achieve strong coupling, it is necessary to ensure the atom-field interaction time, T, is long with respect to other system dynamics [102]. The atom-field coupling and the cavity decay rates are also important, and the coupling regime is often characterised in more specific terms with two dimensionless parameters; the critical photon number

$$m_0 \equiv \frac{\gamma^2}{2g_0^2}$$

and the critical atom number

$$N_0 \equiv \frac{2\gamma\kappa}{g_0^2} = C^{-1}.$$

These values indicate the number of quanta necessary to significantly influence the system. Strong coupling is usually defined when both N_0 and m_0 are less than one.

The critical photon number is the number of intra-cavity photons necessary to saturate the atom in a resonant transition. For our purposes, it is not an important value since we are unconcerned with the number of *photons* needed for the successful detection of a *single atom*. The critical atom number refers to the necessary number of atoms required to significantly affect the cavity field. For single atom detection, it is desirable to work with $N_0 \lesssim 1$, since this implies the presence of a *single* atom will have a significant influence on the cavity transmission and be easily measured. N_0 is often inverted, and refered to as the co-operativity parameter, C [82].

Single-atom detection need not be performed in the strong coupling regime - where *both* N_0 and m_0 are small - as has been highlighted in work by several authors [60, 73]. The main objective is to minimise N_0 subject to real world experimental constraints.

Short cavities may be used to increase g_0, which scales inversely with the square root of the cavity volume. As a result, short cavities lead to a reduction of m_0. Cavity length does not, however, influence N_0, since κ also scales with the inverse of cavity length, and thus the length dependence is cancelled in the presence of κ and g_0^2. Motivated by the strong coupling regime, and at times by the complementary requirements of restricted geometry in chip experiments, recent work in cavity QED has tended towards very short cavities, tens to hundreds of micrometers [93, 70, 103, 60, 102, 138]. Although limiting cavity length will not improve single atom detection, it is possible to reduce the mode volume in ways that do help. Reducing the beam diameter in the cavity is one such possibility [60, 138].

As well as reducing cavity length, considerable efforts have been made to produce cavities with ultra-high finesse. This results in diminished cavity linewidth, κ, without an accompanying reduction in g_0, so is an ideal way to manipulate N_0. Whispering gallery mode cavities have reached a finesse of $\mathscr{F} > 10^7$ [126] and open optical cavities with finesses in excess of $\mathscr{F} = 3 \times 10^5$ have been demonstrated using custom built mirrors [102, 103]. Custom design and fabrication can be a costly and arduous task, however reasonably high finesses of around $\mathscr{F} \sim 10^4$ are within reach even with commercial mirrors (*Newport 'SuperMirror' 10CV00SR.40F*). Although this is a trade-off in mirror quality for ease and expense of construction, we will show that it is still possible to achieve a good signal-to-noise ratio for single atom detection using such a finesse, provided the system is operated in appropriate regions of parameter space. Determining where these regions are is the motivation for the work covered in this chapter.

The layout is as follows:

- **Section 3.2** reviews the atom-cavity field model presented in chapter 2 as the essence of an ideal atom detector using direct photon counting.
- The signal-to-noise ratio in the entire parameter space is then analysed in **section 3.3**.
- In **section 3.4.1**, we introduce the limitations of real photon detectors based on single photon counting modules, and consider the implications for the cavity operating regime.
- An alternative photon detection scheme based on heterodyne detection is presented in **section 3.4.2**.
- **Section 3.4.4** discusses the susceptibility of the atom detection process to frequency noise in the system for different operating conditions.
- Finally, in **section 3.4.5**, we consider the conversion of signal-to-noise ratio to detector quantum efficiency (QE) and other limits to detection quality.

3.2 Cavity QED Model

The system we are interested in is illustrated in figure 3.1(a). It consists of a single two-level atom with an excited state resonance at ω_a coupled to the TEM$_{00}$ mode of an optical cavity with resonant frequency ω_c.

The system is driven with a classical (coherent) field at ω_0 and dissipation occurs *via* spontaneous decay of the atomic excited state, γ, and cavity field decay, κ. The cavity decay comprises transmission through input and output mirrors as well as scattering losses: $\kappa = \kappa_{\text{in}} + \kappa_{\text{out}} + \kappa_{\text{loss}}$ giving a cavity linewidth (FWHM) of 2κ.

The Hamiltonian for this system is that of the driven Jaynes-Cummings model. In a reference frame rotating with the driving field, as presented in section 2.3:

$$\hat{H} = \hbar\Delta_c \hat{a}^\dagger \hat{a} + \hbar\Delta_a \hat{\sigma}_+ \hat{\sigma}_- + \hbar g(\boldsymbol{r})(\hat{a}\hat{\sigma}_+ + \hat{a}^\dagger \hat{\sigma}_-) + \hbar\varepsilon(\hat{a} + \hat{a}^\dagger).$$

The position-dependent atom-field coupling constant is given by $g(\boldsymbol{r}) = g_0 U(\boldsymbol{r})$ where $U(\boldsymbol{r})$ is the normalised magnitude of the electric field, and g_0 is the single-photon field-atom coupling constant, a measure of the maximum coupling strength. For a Gaussian standing-wave of waist size w_0 and cavity length L, $U(\boldsymbol{r}) = \cos(2\pi z/\lambda)\exp(-(x^2+y^2)/\mathrm{w}_0)$. The effective mode volume, integrated over the cavity length, is $V = \pi \mathrm{w}_0^2 L/4$. The single-photon electric field coupling constant for this mode is $g_0 \equiv \sqrt{\mu^2\omega_c/(2\hbar\epsilon_0 V)}$, where μ is the electric-dipole moment of the atom aligned in the field. The coupling can also be expressed as $g_0 = \sqrt{\sigma_0 c\gamma/V}$ for atomic cross-section $\sigma_0 = 3\lambda^2/(2\pi)$, and γ the free space atomic decay rate.

Expectation values for system operators, $\hat{O}$, are determined using the density-operator relation:

$$\langle\hat{O}\rangle = \mathrm{Tr}\left\{\rho\hat{O}\right\},$$

where the density matrix, ρ, is found from the steady-state solution to the master equation:

$$\begin{aligned}\frac{d}{dt}\rho(t) &= -\frac{i}{\hbar}[\hat{H},\rho] + \kappa(2\hat{a}\rho\hat{a}^\dagger - \hat{a}^\dagger\hat{a}\rho - \rho\hat{a}^\dagger\hat{a}) \\ &\quad + \frac{\gamma}{2}(2\hat{\sigma}_-\rho\hat{\sigma}_+ - \hat{\sigma}_+\hat{\sigma}_-\rho - \rho\hat{\sigma}_+\hat{\sigma}_-). \qquad (3.1)\end{aligned}$$

3.2.1 A little bit of code

We model the cavity mode with a truncated Fock state basis, $|0\rangle, |1\rangle, |2\rangle \ldots |k\rangle$ that is valid provided k is significantly larger than the mean intra-cavity photon number. The result is a set of $2(k+1)$ linear equations ($k+1$ photon states, and two atomic states) that are solved to find the steady-state density matrix, $\rho(t_{ss})$.

We express the matrix elements of $\dot{\rho}$ making use of equation (3.1), and

$$\dot{\rho}_{mn,ij} = \langle n, j|\dot{\rho}|m, i\rangle \qquad (3.2)$$

Here, m, n represent the initial and final photon occupation, and i, j the atomic excitation (g or e). We need equations for the matrix elements for $0 < (m,n) < k$ as well as the cases when either m or n is the lowest or highest occupation number (0 or k) and for ($i = j = e$), ($i = j = g$),($i = g, j = e$), and ($i = e, j = g$). An example is, for $0 < (m,n) < k$ and $i = j = g$:

$$\begin{aligned}\dot{\hat{\rho}}_{mn,gg} &= -i\Delta_a\hat{\rho}_{mn,gg}\\ &\quad -i\varepsilon[\sqrt{n+1}\hat{\rho}_{mn+1,gg}+\sqrt{n}\hat{\rho}_{mn-1,gg}-\sqrt{m}\hat{\rho}_{m-1n,gg}-\sqrt{m+1}\hat{\rho}_{m+1n,gg}]\\ &\quad -ig[\sqrt{n}\hat{\rho}_{mn-1,gg}-\sqrt{m}\hat{\rho}_{m-1n,gg}]\\ &\quad +\gamma\hat{\rho}_{mn,ee}\\ &\quad +\kappa[2\sqrt{(n+1)(m+1)}\hat{\rho}_{m+1n+1,gg}-(m+n)\hat{\rho}_{mn,gg}].\end{aligned}$$

A sample of the Mathematica® code used in these simulations is given in appendix A.

The size of the Fock basis we used varied depending on the simulation. A smaller basis improves the computational speed, but is only appropriate for very small values of the mean intra-cavity photon number. We found the smallest workable size depended on the input photon number, N_{in}, and the coupling of the cavity input mirror. For $N_{\text{in}} < 20$, we used a basis size of $k = (3 + 11.5\sqrt{N_{\text{in}}/(\kappa/2)})$, and otherwise used $k = (26.2 + 1.45N_{\text{in}}/(\kappa/2))$ - where values for k were rounded up to the nearest integer. With these values, our simulations provided numerical results that did not change with increased basis sizes.

The atom is detected inside the cavity *via* its influence on the cavity field and subsequently the cavity transmission. The number of photons detected at the output mirror in a measurement interval, τ, is $N = n\kappa_{\text{out}}\tau$, where $n = \langle\hat{a}^\dagger\hat{a}\rangle$ is the steady-state intra-cavity photon number. For a cavity containing no atoms, with an intracavity photon number n_0, $N_{\text{empty}} = n_0\kappa_{\text{out}}\tau$. The signal for an atom detection event is the difference in these photon numbers, and, assuming the statistics remain Possionian during an atom transit, the signal-to-noise ratio of the measurement is

$$\text{SNR} = \frac{(N_{\text{empty}} - N)}{\sqrt{N_{\text{empty}} + N}}. \tag{3.3}$$

As well as $n = \langle\hat{a}^\dagger\hat{a}\rangle$, other expectation values that we are interested in are $\langle\hat{a}\rangle$, $\langle\hat{a}^\dagger\rangle$ and $\langle -i(\hat{a} - \hat{a}^\dagger)\rangle$ as we will discuss in sections 3.4.2 and 3.4.3.

The assumption of Poissonian noise can break down in extreme regimes of high finesse and large atom cavity coupling where anti-bunching and squeezing can occur [30]. We will, however, concentrate on regimes, where we have confimed that these effects are minimal.

3.3 Detection Parameter Space

By 'parameter space' for single atom detection, we refer to variations in cavity-probe ($\Delta_c = \omega_0 - \omega_c$), and atom-probe ($\Delta_a = \omega_0 - \omega_a$) detunings, cavity finesse ($\mathscr{F} = \pi R^{1/2}/(1-R)$), and probe power (related to ε). In this section, we present numerical data for the signal-to-noise ratio of atom detection with a maximally coupled atom-cavity system ($g(\boldsymbol{r}) = g_0$). We find these data are naturally separated into two broad detection regimes: resonant detection at low probe powers, and non-resonant detection at higher powers. These regions of parameter space are addressed separately in sections 3.3.1 and 3.3.2.

3.3.1 Resonant Detection

Initially, we consider the resonant condition, a point in parameter space where all three system frequencies are coincident; $\omega_0 = \omega_c = \omega_a$.

The system we model is for a transition in the rubidium 87 D2 line ($5^2\mathrm{S}_{1/2} \rightarrow 5^2\mathrm{P}_{3/2}$, $\lambda = 780$nm: refer to figure 2.1) with a decay rate of $\gamma = 2\pi \times 6$MHz [134]. The cavity length is $L = 100\mu$m, and mode waist $\mathrm{w}_0 = 20\mu$m. For a cavity with approximately planar mirrors the described geometry means the Purcell effect can be ignored. The system has an atom-field coupling of $g_0 \sim 2\pi \times 26$MHz and a cavity decay rate that scales inversely with finesse. We have chosen to present data for these parameters because they are in the range of realistic experimental design [103], however, the qualitative results that are presented in this work are common to a wide range of design choices.

The data presented here are for an impedence-matched cavity, where $\kappa_{\text{out}} = \kappa_{\text{in}} = (1/2)\kappa$, and the empty-cavity transmission is 100%. In an experimental set-up, it is the input probe power, rather than transmitted power, that is kept constant during an atom detection event, so data are parameterised in terms of this input photon flux. In the results presented, we consider $\kappa_{\text{loss}} = 0$, a reasonable approximation for cavities of moderate finesse. We also note that one could immediately gain a factor of $\sqrt{2}$ in the signal-to-noise ratio, [equation (3.3)], by using an undercoupled cavity with $\kappa_{\text{in}} \ll \kappa_{\text{out}}$, instead of the impedence-matched cavity modelled here. In chapter 5, we discuss the parameters for the actual experimental cavity, where we have chosen mirrors with the transmissivity favouring the output mirror by a factor of three.

Figure 3.2 shows how the signal-to-noise ratio varies with probe power and

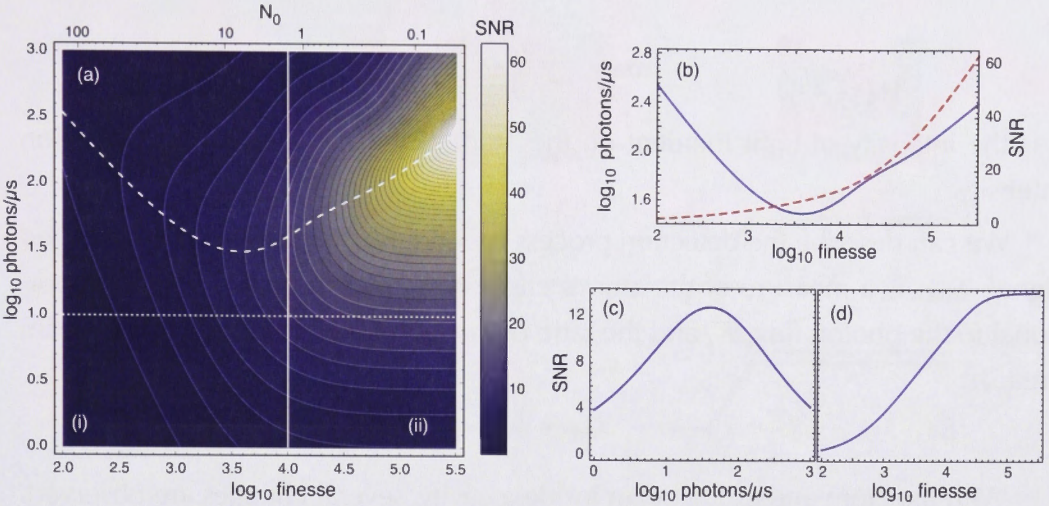

Figure 3.2: Signal-to-noise ratio for resonant atom detection with ideal photon counting. The cavity has a length of 100μm, and waist of 20μm. $\kappa_{\text{in}} = \kappa_{\text{out}}, \kappa_{\text{loss}} = 0$, $\gamma = 2\pi \times 6$MHz, $\tau = 20\mu$s. Panel (b) corresponds to a cross section along the dashed line in (a), showing the positions of optimum SNR. The dashed line indicates the SNR and solid line the power as a function of cavity finesse. Panel (c) corresponds to the solid line at $\mathscr{F} = 10^4$ and (d) to a cross section along the dotted line in (a) at flux$=$ 10photons/μs.

cavity finesse. In figure 3.2(a), the dashed line traces the position of maximum SNR. For a given finesse, there is a clear optimum power at which to operate, shown for $\mathscr{F} = 10^4$ in figure 3.2(c). As the finesse increases, the maximum value of the signal-to-noise ratio improves.

At $\mathscr{F} \sim 3000$, there is a transition in the system's behaviour; as this value is approached from the low-finesse side, the optimum signal-to-noise ratio occurs at lower probe power, while in the limit of high-finesse, the reverse is true, and increasing cavity finesse beyond 3000 requires increases in power to achieve the maximum signal-to-noise ratio. The transition can be understood in context of the critical atom number, N_0, and we can separate the plot into regions of (i) high and (ii) low critical atom number.

High Critical Atom Number: Atom as a Saturable Absorber

In the low-finesse limit, the critical atom number is large (> 1), so multiple atoms are necessary to substantially influence the cavity transmission. An equivalent statement is to say that in this regime the effect of a single atom on the transmitted power is only perturbative. In this limit, the atom can be modelled classically as a saturable absorber with absorption cross-section, σ, that scales, on resonance, as

$$\sigma = \frac{\sigma_0}{I/I_{\text{sat}} + 1}.$$

I is the intensity of light incident on the atom and I_{sat} is the atomic saturation intensity.

We can describe the detection process as follows. In free space, the detected signal, S_{det}, is a measure of the atom's effect on a photon beam, and is proportional to the photon flux, F, and the ratio of the atomic cross-section to the beam area, A:

$$S_{\text{det}} = F\frac{\sigma}{A}.$$

With the atom and probe beam inside a cavity, several changes are observed. Each photon now passes the atom more than once, effectively increasing F. The atom therefore has a greater chance of absorbing each photon, and has a more significant effect on the probe beam when the absorption happens inside a cavity. As the finesse increases, so too does the number of round trips for each photon before it decays from the cavity mode, so the signal improves with finesse.

A second effect of the intensity amplification by the cavity, is a reduction in atomic cross-section. Increases in finesse therefore mean that the external probe power necessary to saturate the atom (inside the cavity) is reduced, and the maximum signal-to-noise ratio requires lower power as the finesse increases, in accordance with the dashed line in region (i) of figure 3.2(a).

Low Critical Atom Number: Coupled Resonators

In contrast with the low-finesse regime, the high-finesse regime requires increasing probe powers with increasing finesse in order to achieve the maximum signal-to-noise ratio.

In region (ii) of figure 3.2(a), the critical atom number, N_0, is less than one, so a single atom significantly influences the system. The smaller N_0 becomes, the more significant an effect a single atom will have. In this regime, we consider the quantum mechanical model in more detail. That model concerns the coupling of two resonators, the bare two-level atom and the empty cavity, giving coupled (dressed) states, $|n+\rangle$ and $|n-\rangle$, that are linear combinations of the uncoupled states: $|n+\rangle = \sin\alpha|n-1\rangle|e\rangle + \cos\alpha|n\rangle|g\rangle$ and $|n-\rangle = \cos\alpha|n-1\rangle|e\rangle - \sin\alpha|n\rangle|g\rangle$. The Jaynes-Cummings energy spectrum of these dressed states has eigenenergies

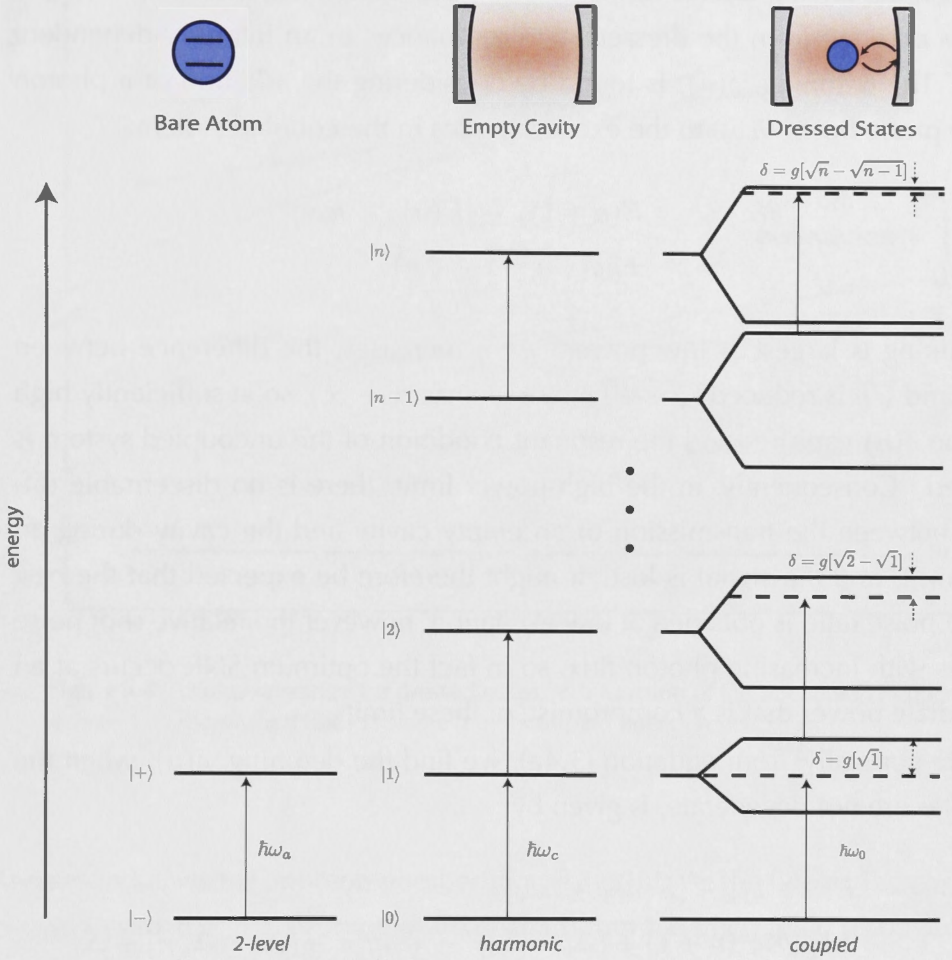

Figure 3.3: Energy spectrum for resonant dressed states. Detunings reduce for high levels of exitation.

given by

$$E(n)_{\pm} = \hbar\omega_c(n - 1/2) \pm \frac{1}{2}\hbar\sqrt{4g^2 n + (\Delta_c - \Delta_a)^2}, \tag{3.4a}$$

that reduce, in the case of resonant atom and cavity driving, $\Delta_c = \Delta_a = 0$, to

$$E(n)_{\pm} = \hbar\omega_0(n - 1/2) \pm \hbar g\sqrt{n}. \tag{3.4b}$$

A good review of the dressed states for this resonant condition is given in reference [6].

Figure 3.3 shows the mode-splitting of the resonant dressed atom-cavity system. When the driving laser is resonant with the uncoupled system ($\hbar\omega_0 = \hbar\omega_a = \hbar\omega_c$), it is detuned from the dressed state resonances in an intensity-dependent manner. The detuning, $\delta(n)$, is found by considering the addition of a photon from the probe beam ($\hbar\omega_0$) to the excited modes in the coupled system:

$$\begin{aligned}\delta(n) = & \quad E(n+1)_\pm - [E(n)_\pm + \hbar\omega_0] \\ = & \quad \pm\hbar g(\sqrt{n+1} - \sqrt{n})\end{aligned}$$

The detuning is largest at low power. As n increases, the difference between $\sqrt{n+1}$ and $\sqrt{n}$ is reduced ($\sqrt{n+1} - \sqrt{n} \to 0$ as $n \to \infty$), so at sufficiently high excitation $\delta(n)$ vanishes and the resonant condition of the uncoupled system is recovered. Consequently, in the high-power limit, there is no discernable difference between the transmission of an empty cavity and the cavity during an atom transit, and the signal is lost. It might therefore be expected that the best signal-to-noise ratio is obtained at low excitation, however the relative shot noise improves with increasing photon flux, so in fact the optimum SNR occurs at an intermediate power that is a compromise of these limits.

More generally, from equation (3.4a), we find the detuning, $\delta(n)$, when the bare-states are not degenerate, is given by:

$$\begin{aligned}\delta(n) = & \quad E(n+1)_\pm - [E(n)_\pm + \hbar\omega_0] \\ = & \quad \pm\hbar[\sqrt{4g^2(n+1) + (\Delta_c - \Delta_a)^2} - \sqrt{4g^2 n + (\Delta_c - \Delta_a)^2}] - \Delta_c\end{aligned}$$

and (once again) we find that at high power levels, when $n+1 \to n$, the detuning of the uncoupled cavity (Δ_c) is recovered. Figure 3.4 shows the energy spectrum of the dressed states as a function of the frequency difference between the uncoupled system components. The centre at $\Delta_c = \Delta_a$ corresponds to the mode-splitting shown in figure 3.3.

The detuning, $\delta(n)$, must be considered in the context of the system decay rates that determine the linewidth of the dressed modes. Figure 3.5 shows the mode-splitting for $\mathscr{F} = 10^3$, 10^4 and 10^5, at probe powers of 1 and $10^{2.3}$ photons/μs.

In a system with large decay rates, or low finesse [figure 3.5(a)], the dressed state resonant frequencies are not distinctly different from the uncoupled, empty cavity, resonance. Since there is little contrast, the signal is lost easily with in-

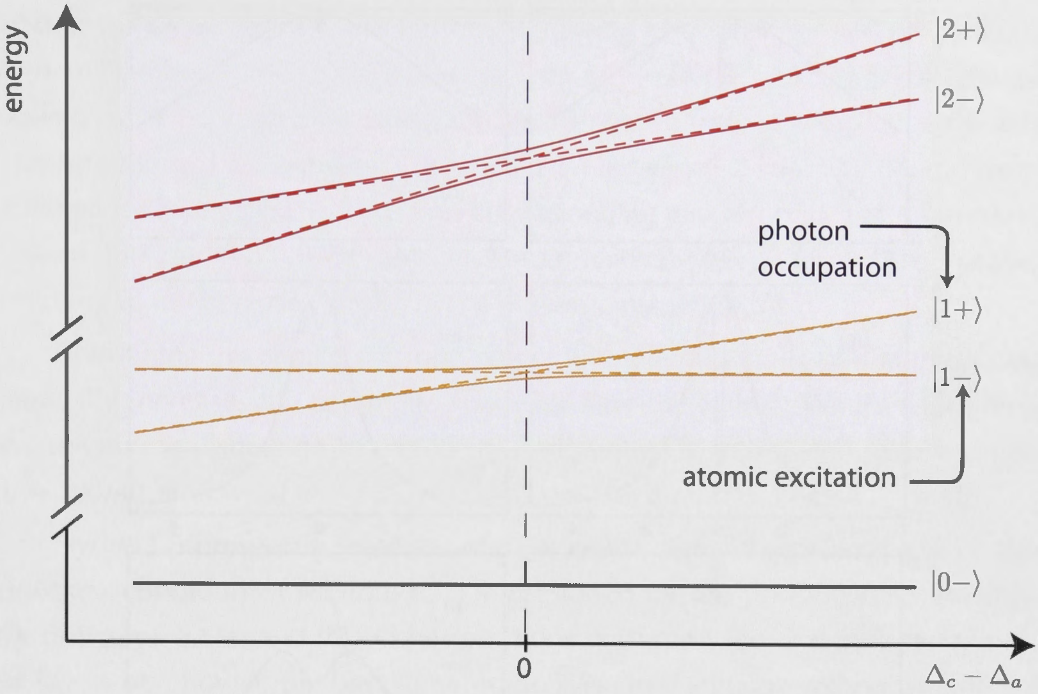

Figure 3.4: Energy spectrum for dressed states, as a function of the uncoupled frequency difference. The dashed lines indicate the uncoupled energy levels.

creases in intra-cavity photon number [figure 3.5(b)]. As the finesse increases, the dressed state energies become more distinct from the uncoupled resonance [figure 3.5(e)]. In the high-finesse regime, the probe power must be increased considerably before the high-intensity detuning limit ($n+1 \rightarrow n$) comes into effect. Consequently, increasing finesse requires increasing probe powers to achieve the maximum signal-to-noise ratio, as indicated with the dashed line in region (ii) of figure 3.2(a).

If we choose to limit the probe power with which the cavity is driven (the flux limit of single photon counting modules is discussed in section 3.4.1), then the signal-to-noise ratio no longer improves with finesse, as shown in figure 3.2(c). In this high-finesse regime, the mode-splitting results in a complete black-out of cavity transmission during an atom transit (shown as the long arrow (i) in figure 3.5(e)). Further increases in finesse narrow the resonances but cannot improve the signal that is already maximized. In this regime, the signal-to-noise ratio only improves by increasing the probe power.

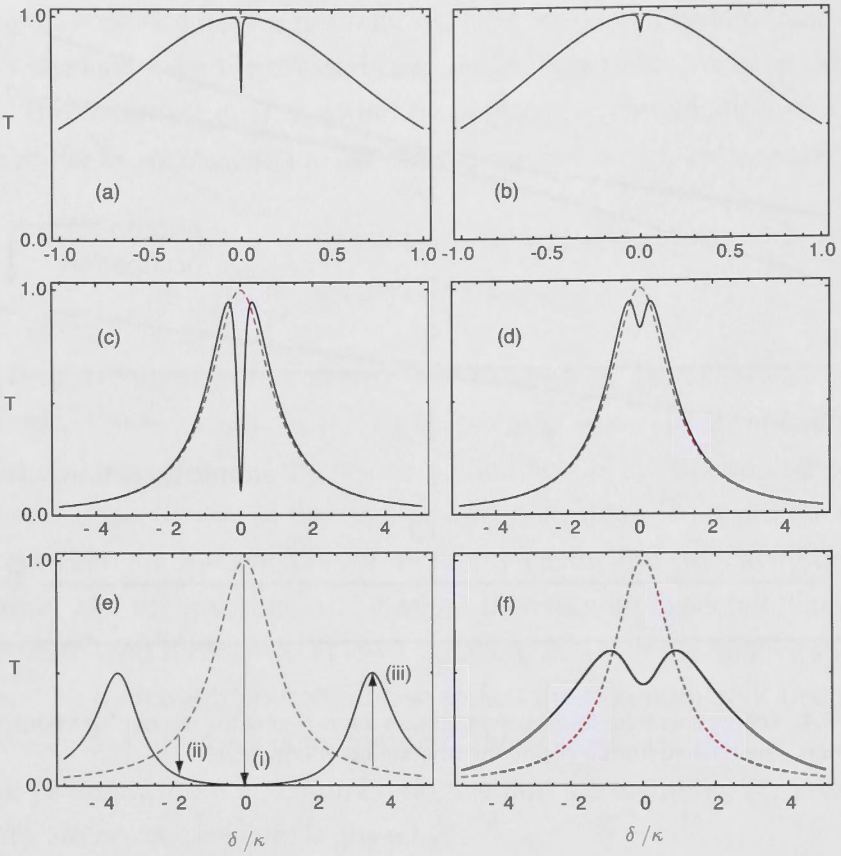

Figure 3.5: Relative photon transmission, T, for the atom-cavity system as a function of probe detuning. Dashed traces are for the empty cavity and solid lines represent the dressed modes. The cavity finesse $\mathscr{F}$ is (a,b) 10^3, (c,d) $\mathscr{F} = 10^4$ and (e,f) 10^5. The left plot for each value of $\mathscr{F}$ is for a driving flux of 1 photon/μs, the right is for $10^{2.3}$ photons/μs.

3.3.2 Non-Resonant Detection

By detuning the probe, we open the possibility of both 'positive' and 'negative' signals. The sign is arbitrarily defined by equation (3.3), and is not important: 'Positive' signals correspond to decreases in cavity transmission (since these are the natural signals observed with resonant detection, and therefore probably the most intuitive to understand). Both positive and negative signals have been observed in previous cavity detection work [70]. The arrows on figure 3.5(e) show examples of the sign and magnitude of the signal for various detunings. Arrows pointing *down* are an indication of positive signals, while an upwards pointing arrow implies an increase in transmission during an atom detection event. For a resonant probe (i), the signal is always seen as a reduction ('dip') in transmitted power, since the atom effectively detunes the system from resonance. A dip may also be observed if the probe is detuned from the empty cavity (ii). Alternatively, if the probe is detuned to a position corresponding to a resonance of the dressed system, the atom will bring the system onto resonance with the detuned probe, resulting in an increase ('peak') in the power transmitted (iii).

Combining the choice of probe power with the possibility of detunings dramatically increases the parameter space for atom detection. We therefore limit the remaining discussion to the cavity design already introduced (cavity length $L = 100\mu$m, and waist $w_0 = 20\mu$m), and consider a modest finesse $\mathscr{F} = 10^4$.

Figure 3.6 presents a selection of data for the signal-to-noise ratio, with the resonant condition of section 3.3.1 represented by the position A in the centre of figures 3.6(a) and (b). Other positions correspond to non-zero detunings. At low probe power, the best signal-to-noise ratio occurs on-resonance and for higher powers, the maximum shifts to detuned operating conditions. Figure 3.6(c) shows the signal-to-noise ratio as a function of power for positions A, B and C in figure 3.6(a) and (b).

The global maximum for the signal-to-noise ratio (ie: the best SNR obtainable over the whole parameter space) is the peak of ~ 13 that occurs on resonance, at A. Nonetheless, it may be advantageous to work with red-detuned ($\Delta_a > 0$) conditions, due to the benefits of the dipole force that can be used to manipulate the atom's position in the cavity [104]. This process and the benefits it affords the detection efficiency are the essence of the following chapter.

The mode-splitting shown in figure 3.5 is a useful picture for the dressed states of a resonant system. It is also a good description of the dressed states of a system with equal detunings, $\Delta_a = \Delta_c$, accessed when the probe laser frequency is scanned but the cavity is kept resonant with the atom ($\omega_c = \omega_a$), but for more general detunings and at high power, the split modes do not provide useful intuition about the atom's influence on the system.

Figure 3.6(d) shows the output flux for the empty cavity and the coupled atom-cavity system at a driving flux of 10^4 photons/μs with the data normalised to the empty cavity transmission. The probe frequency is scanned giving atom-probe and cavity-probe detunings indicated on the top and bottom axes. For

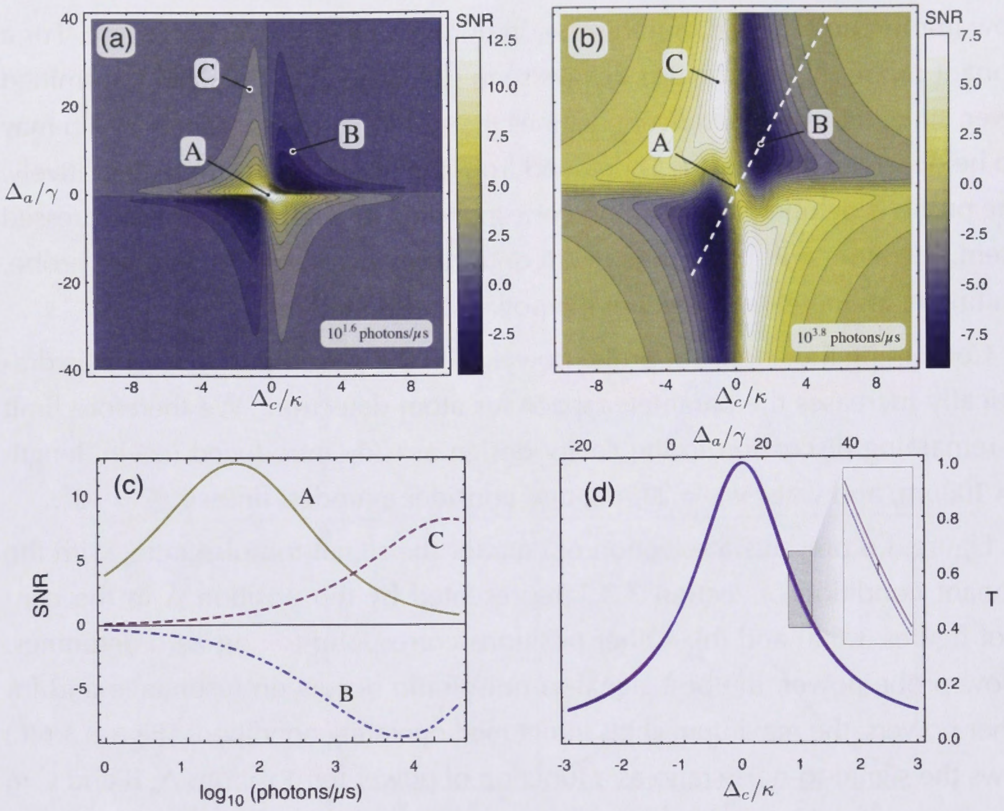

Figure 3.6: Signal-to-noise ratio for a range of cavity and atom detunings. $\mathscr{F} = 10^4$, other parameters as in figure 3.2. The probe power is (a) ~ 40 photons/μs, (b) ~ 6300 photons/μs. (c) Signal-to-noise ratio as a function of probe power positions in detuning space marked A ($\Delta_c = 0\kappa, \Delta_a = 0\gamma$), B ($\Delta_c = 1\kappa, \Delta_a = 10\gamma$) and C ($\Delta_c = -1\kappa, \Delta_a = 25\gamma$) in (a) and (b). (d) normalised cavity transmission, T, at a probe power of 10^4 photons/μs, through the cross-section shown with the white dashed line in (b). The atom shifts the cavity resonance from the dashed to solid line, giving a signal represented with the short arrow.

these detuning and power conditions, the atom has a dispersive effect, shifting the cavity resonance as shown by the solid line in figure 3.6(d). At the resonant peak there is almost no change in transmitted power, since here the amplitude gradient is zero, but on the side of the resonance the small frequency shift means a signal is observed, indicated with the short arrow in the inset of 3.6(d). The signal relative to the empty cavity transmission is small, but since it occurs at high probe power the relative shot noise is also small so the signal-to-noise ratio can be large. In 3.6(c), the magnitude of the optimum signal-to-noise ratio at position B is ~ 9. This is not as good as the signal-to-noise ratio achievable on-resonance but is still very satisfactory.

It should be mentioned of course, that achieving the shot-noise limit when operating on the side of a resonance - where frequency noise in the apparatus translates to amplitude noise at the detection - is usually experimentally challenging, and consequently avoided. We will discuss this further in section 3.4.4, but also note that there are other possibilities for taking advantage of detuned detection, without having to work on the flanks of a resonant feature. Work by Lye *et al.* [91] and Horak *et al.* [73] considered the signal-to-noise ratio for far-detuned detection in a different way; the dispersive interaction of the atom with the cavity field can be measured as a phase shift, rather than a variation in transmission amplitude. The phase angle measures the difference between the phase of the transmitted probe and the input laser. For the empty cavity, the phase response is zero at the resonant frequency, and it is here that the phase gradient is largest, as shown in figure 2.5. The frequency shift that the atom induces therefore has the greatest effect on the phase at the transmission intensity peak, rather than the side of the transmission where the amplitude gradient is maximum. Phase quadrature detection with a heterodyne set-up is discussed in section 3.4.3.

3.4 Photon Counting Practicalities

3.4.1 Single Photon Counting Modules

In section 3.3 we presented data for an ideal atom detection system where all the transmitted photons at the cavity output mirror are detected. In practice, this will never be the case, and optimization of atom detection is critically influenced by the photon measurement process.

A typical single photon counting module is an avalanche photodiode (APD), for example *Perkin Elmer SPCM-AQRH* [4]. This type of device has been employed in experiments by several research groups [103, 102, 74]. The quantum efficiency (QE) of an APD is typically around 50% at 780nm, but is non-linear with power. We will, however, continue to assume an efficiency of 50%, noting that this generous value is limited to low photon flux. An acceptible incident photon flux limit is about 20 photons/μs, giving an APD count rate of 10 photons/μs. The net result of 50% efficient detection is a reduction by a factor of $\sqrt{2}$ in the signal-to-noise ratio. The detector flux limit means that, even for the moderate finesse of $\mathscr{F} = 10^4$ considered here, we cannot reach the probe power required for optimal detection using an APD.

3.4.2 Heterodyne Detection

So far we have considered the detection of cavity transmission by direct photon counting, measuring the observable, $\langle \hat{a}^\dagger \hat{a} \rangle$. Saturation of real single photon detectors means we are obliged to limit the probe power, and consequently cannot access the optimum signal-to-noise ratio of an ideal atom detector. An alternative is to use heterodyne detection with photodiodes that do not saturate at the probe power discussed here, but is still capable of measuring the very low powers with which we are concerned [93]. A possible set-up is indicated in figure 3.7.

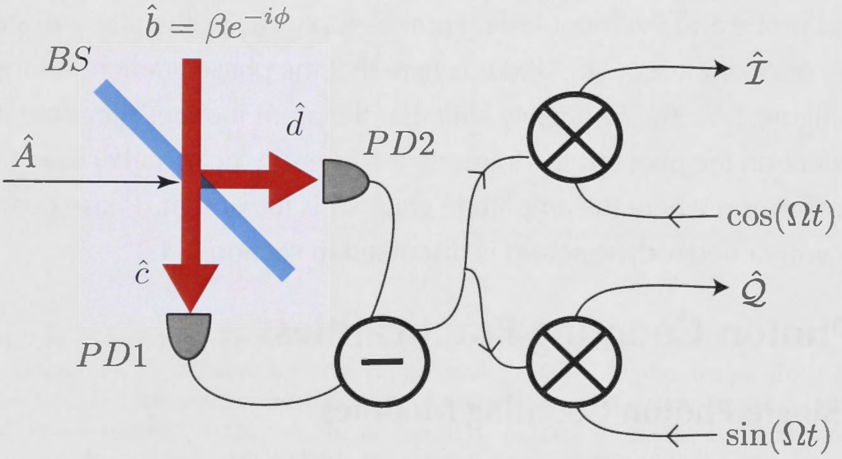

Figure 3.7: Schematic representation of heterodyne photodetection.

Input fields $\hat{A}$ and $\hat{b}$ are combined on a 50-50 beam-splitter. Here, $\hat{A} = \hat{a}\sqrt{\kappa_{\text{out}}\mathcal{T}}$ is the field at the cavity output mirror and $\hat{b} = \beta e^{-i\phi}$ is that of a strong coherent local oscillator, whose frequency is shifted from the probe laser by Ω. The phase of the local oscillator (LO) can then be expressed as $\phi = \Omega t + \varphi$, where Ω is the explicit frequency difference, and φ is an arbitrary phase difference. We require the heterodyne signal to detect the influence of the atom on the transmitted probe power. The process must be independent of any variations in φ. To avoid an involved locking procedure, mixing the signal with appropriate $\sin(\Omega t)$ and $\cos(\Omega t)$ components removes the phase dependence as follows:

The beam-splitter output fields, $\hat{c} = 1/\sqrt{2}(\hat{A} + \hat{b})$ and $\hat{d} = 1/\sqrt{2}(\hat{A} - \hat{b})$, are measured as currents at photodiodes PD1 and PD2:

$$\hat{c}^\dagger\hat{c} = \frac{1}{2}(\hat{A}^\dagger\hat{A} + \hat{b}^\dagger\hat{b} + \hat{A}^\dagger\hat{b} + \hat{b}^\dagger\hat{A}),$$

$$\hat{d}^\dagger\hat{d} = \frac{1}{2}(\hat{A}^\dagger\hat{A} + \hat{b}^\dagger\hat{b} - \hat{A}^\dagger\hat{b} - \hat{b}^\dagger\hat{A}).$$

Subtracting these photocurrents we find

$$\hat{c}^\dagger\hat{c} - \hat{d}^\dagger\hat{d} = \beta(\hat{A}^\dagger e^{-i\phi} + \hat{A}e^{i\phi}). \tag{3.5}$$

Mixing the signal with sine and cosine functions that oscillate at Ωt gives terms

$$\begin{aligned} \hat{\mathscr{I}} = &\quad \cos(\Omega t) \times \beta(\hat{A}^\dagger e^{-i(\Omega t+\varphi)} + \hat{A}e^{i(\Omega t+\varphi)}) \\ = &\quad (\beta/2)[\hat{X}^+\cos(\varphi) - \hat{X}^-\sin(\varphi) \\ &\quad +\hat{X}^+\cos(2\Omega t+\varphi) - \hat{X}^-\sin(2\Omega t+\varphi)] \\ = &\quad (\beta/2)(\hat{X}^{-\varphi} + \hat{X}^{-(2\Omega t+\varphi)}), \end{aligned} \tag{3.6}$$

$$\begin{aligned} \hat{\mathscr{Q}} = &\quad \sin(\Omega t) \times \beta(\hat{A}^\dagger e^{-i(\Omega t+\varphi)} + \hat{A}e^{i(\Omega t+\varphi)}) \\ = &\quad (\beta/2)[-\hat{X}^+\sin(\varphi) - \hat{X}^-\cos(\varphi) \\ &\quad +\hat{X}^+\sin(2\Omega t+\varphi) + \hat{X}^-\cos(2\Omega t+\varphi)] \\ = &\quad (\beta/2)(\hat{X}^{-(\varphi+\pi/2)} + \hat{X}^{-(2\Omega t+\varphi-\pi/2)}) \end{aligned} \tag{3.7}$$

where we have used the amplitude, $\hat{X}^+ = (\hat{A}^\dagger + \hat{A})$, and phase, $\hat{X}^- = -i(\hat{A} - \hat{A}^\dagger)$, quadratures of $\hat{A}$ and expressed the results with $\hat{X}^\vartheta = \hat{X}^+\cos(\vartheta) + \hat{X}^-\sin(\vartheta)$. Equations (3.6) and (3.7) are used to generate the final measurement,

$$\begin{aligned} \langle\hat{\mathscr{I}}\rangle^2 + \langle\hat{\mathscr{Q}}\rangle^2 = &\quad (\beta^2/4)[\langle\hat{X}^+\rangle^2 + \langle\hat{X}^-\rangle^2] \\ = &\quad (\beta^2/4)[\langle\hat{A} + \hat{A}^\dagger\rangle^2 - \langle\hat{A} - \hat{A}^\dagger\rangle^2] \\ = &\quad \beta^2\langle\hat{A}\rangle\langle\hat{A}^\dagger\rangle. \end{aligned} \tag{3.8}$$

Terms with $2\Omega t$ dependence in $\hat{\mathscr{I}}$ and $\hat{\mathscr{Q}}$ are vacuum terms [151, 150]. They do not contribute to the signal but add to the noise which is determined by examining the variance of $\hat{\mathscr{I}}$ and $\hat{\mathscr{Q}}$. The variance $V_{\hat{\mathscr{I}}} \equiv (\Delta\hat{\mathscr{I}})^2$ is given by

$$\begin{aligned} V_{\hat{\mathscr{I}}} = & \quad \langle\hat{\mathscr{I}}^2\rangle - \langle\hat{\mathscr{I}}\rangle^2 \\ = & \quad (\beta^2/4)[\langle(X^{-\varphi})^2\rangle - \langle X^{-\varphi}\rangle^2 \\ & \quad +\langle(X^{-(2\Omega t+\varphi)})^2\rangle - \langle X^{-(2\Omega t+\varphi)}\rangle^2] \\ = & \quad (\beta^2/4)[V^{\varphi} + V^{2\Omega t+\varphi}] \\ = & \quad \beta^2/2, \end{aligned}$$

with an identical result for $V_{\hat{\mathscr{Q}}}$. Here, we have assumed the field remains coherent, so the variances of the measured and vacuum fields are both one: $V^{\varphi} = V^{2\Omega t+\varphi} = 1$.

The total noise on the measurement is

$$\begin{aligned} \Delta(\langle\hat{\mathscr{I}}\rangle^2 + \langle\hat{\mathscr{Q}}\rangle^2) = & \quad \sqrt{(2\langle\hat{\mathscr{Q}}\rangle\Delta\hat{\mathscr{Q}})^2 + (2\langle\hat{\mathscr{I}}\rangle\Delta\hat{\mathscr{I}})^2} \\ = & \quad \beta^2\sqrt{2\langle\hat{A}\rangle\langle\hat{A}^{\dagger}\rangle}. \end{aligned} \tag{3.9}$$

The expressions for the measurement [equation (3.8)] and noise [equation (3.9)] replace $N = \kappa_{\text{out}}\tau\langle\hat{a}^{\dagger}\hat{a}\rangle$ in equation (3.3), and a similar approach is taken for the empty cavity coherent field where $\langle\hat{a}\rangle_0\langle\hat{a}^{\dagger}\rangle_0 = \langle\hat{a}^{\dagger}\hat{a}\rangle_0 = n_0$. The signal-to-noise ratio for atom detection *via* field amplitude measurement with a heterodyne set-up is therefore of a slightly different form to that of direct photon number (intensity) detection;

$$S_{\text{het}} = \frac{\sqrt{\kappa_{\text{out}}\tau}(n_0 - \langle\hat{a}\rangle\langle\hat{a}^{\dagger}\rangle)}{\sqrt{2(n_0 + \langle\hat{a}\rangle\langle\hat{a}^{\dagger}\rangle)}}. \tag{3.10}$$

The noise includes the familiar factor of $\sqrt{2}$ of heterodyne measurements [151, 150]. However, the signal-to-noise ratio for heterodyne detection is not necessarily smaller by $\sqrt{2}$ than for direct detection, since the signal and noise now both contain expectation values of different quantum operators.

3.4.3 Phase Quadrature Detection

Instead of the cavity field amplitude or intensity, we can also use the heterodyne set-up to measure the phase of the probe beam with respect to the LO. Changes in phase due to the presence of a single atom can be observed in the dispersive regime discussed in section 3.3.2. The relevant observable in this case is the expectation value of the phase quadrature, $\langle \hat{X}^{-} \rangle = \langle -i(\hat{A} - \hat{A}^{\dagger}) \rangle$, and since the initial phase response of the cavity *without* atom is given by the imaginary part of the field, the detection signal-to-noise ratio becomes:

$$\mathrm{SNR}_{\mathrm{pq}} = \sqrt{\frac{\kappa_{\mathrm{out}} \tau}{2}} \left[\mathrm{Im} \left\{ \frac{\sqrt{n_0}[1 + (\Delta_c/\kappa)^2]}{1 + i(\Delta_c/\kappa)} \right\} + \langle i(\hat{a} - \hat{a}^{\dagger}) \rangle \right] \tag{3.11}$$

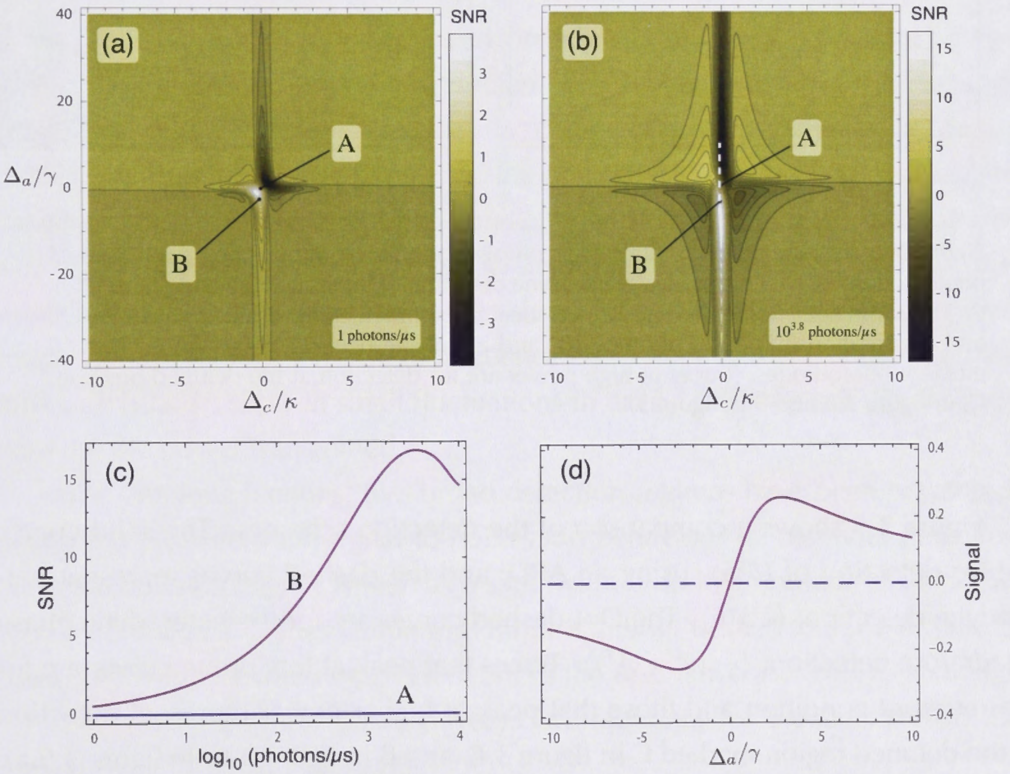

Figure 3.8: Signal-to-noise ratio of phase quadrature detection for a range of cavity and atom detunings. $\mathscr{F} = 10^4$, other parameters as in figure 3.2. The probe power is (a) ~ 1 photons/μs, (b) ~ 6300 photons/μs. (c) Signal-to-noise ratio as a function of probe power for the positions in detuning space marked A ($\Delta_c = 0\kappa, \Delta_a = 0\gamma$) and B ($\Delta_c = 0\kappa, \Delta_a = -2\gamma$) in (a) and (b). (d) Normalised cavity phase shift, at a probe power of 10^4 photons/μs, along the cross-section shown with the dashed white line in (b). The atom shifts the cavity resonance giving a phase shift from the dashed (empty cavity) to solid line (atomic influence). The absolute size of the signal is proportional to the amplitude of the probe beam. The normalised signal is divided by the empty-cavity amplitude.

Phase quadrature detection yields the largest signals and best signal-to-noise ratios on the cavity resonance, since this is the position for which there is the greatest phase gradient in the cavity response function, as discussed in section 2.2. Selected data over the detuning and photon flux parameter space for phase quadrature detection are shown in figure 3.8.

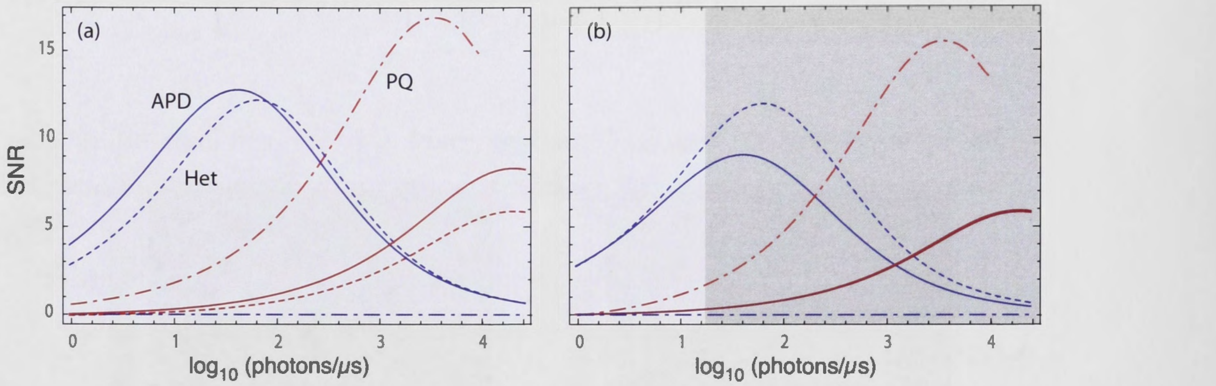

Figure 3.9: A comparison of the signal-to-noise ratio for atom detection with (a) ideal photon counting (APD) and ideal heterodyne detection of intensity (Het) and phase (PQ). (b) The same detection methods, for non-ideal photon detection: an APD with 50% QE and a saturation flux of 20 photons/μs, and a realistic heterodyne set up using 95% efficient photodiodes. Traces at high power are for detection at the detuned position, C, in figure 3.6 and B in figure 3.8.

Figure 3.9 shows a comparison of the detection schemes. The solid curves are for detection of $\langle \hat{a}^\dagger \hat{a} \rangle$, using an APD, and the dashed curves represent heterodyne detection; $\langle \hat{a}^\dagger \rangle \langle \hat{a} \rangle$. The Dot-dashed curves are for the heterodyne phase quadrature detection, $\langle -i(\hat{A} - \hat{A}^\dagger) \rangle$. Traces that peak at low probe power are for the resonant condition and those that peak at higher power represent detection in the detuned region marked C in figure 3.6, and B in figure 3.8. In figure 3.9(a), the comparison is between ideal direct detection and ideal heterodyne detection, using photon detectors with 100% QE. For resonant detection the maximum signal-to-noise ratio is similar in both intensity detection schemes, although the probe power that is necessary to achieve it varies somewhat, whereas the signal (and signal-to-noise ratio) for resonant phase detection is zero.

Figure 3.9(b) includes the quantum efficiencies of real detectors; APD efficiency is 50% and the photodiodes used in the heterodyne set-up are assumed to be 95% efficient. The shaded region indicates the probe powers that are inaccessible to real APDs due to their flux-limit. These realities show a significant difference between the two detection schemes. On-resonance, the best signal-to-noise ratio for the flux-limited APD is about 8, whereas using heterodyne detection at a higher power can achieve a signal-to-noise ratio of approximately 12 for power, or > 15 for phase quadrature detection.

The maximum signal-to-noise ratio of APD and heterodyne detection are in principle very similar. However, since the maximum occurs at high power, APDs are not appropriate for detection in that regime.

3.4.4 Noise Susceptibility

The signal-to-noise ratios presented in our data are determined using photon statistics that are always shot-noise limited. The ability to achieve this depends on the stability of the system as well as the choice of operating regime. For probe intensity (or amplitude) measurements, the operating condition least sensitive to frequency noise is the resonant position ($\Delta_c = 0$) at the peak of the cavity transmission line since here small changes in detuning have little effect on the transmitted power. Detuned detection at the side of the transmission line, as suggested in figure 3.6(d), is more sensitive to frequency noise since here the gradient on the amplitude is large, so even small fluctuations in cavity detuning can significantly influence the power transmitted.

In the previous sections, two broad detection regimes have been presented. Section 3.3.1 covered the signal-to-noise ratio behaviour for resonant detection where the observed signal is seen as a significant drop in amplitude at the transmission peak due to Jaynes-Cummings mode splitting. In section 3.3.2 the signal is observed due to a small frequency shift of the resonance that causes a change in transmitted light at the detuned detection frequency, or a phase shift in the probe laser with respect to a LO.

Frequency noise enters the system *via* variations in the probe laser frequency as well as the cavity length. To eliminate noise (in the measured amplitude, intensity or phase), these components must be extremely stable. The cavity design emphasised in this work has a length of 100μm and finesse $\mathscr{F} = 10^4$, giving a linewidth of 150MHz. Assuming frequency locking on the order of 100kHz (easily achieved with a diode laser and low locking bandwidth), amplitude fluctuations at the position of the signal marked by the short arrow in figure 3.6(d) are roughly one part in 1000. The transmitted power at this position is approximately

5000 photons/μs, with shot noise of about one part in 100, so the amplitude fluctuations due to frequency-locking limitations are well below the shot noise limit.

Measuring phase rather than intensity in the detuned regime is also sensitive to frequency noise at the transmission resonance since the gradient of the cavity phase response on the resonance transmission peak is zero, as discussed in sections 3.4.2 and 2.2.

For longer cavities or for cavities with higher finesse, the transmission linewidth decreases, so the frequency stability needs to be improved. For some operating conditions and cavity designs, therefore, the influence of frequency noise may become difficult to eliminate. In such cases, if the noise can be measured, it can be simply subtracted from the signal. Measuring the noise *via* an error signal is an ideal solution, since a possible mechanism for locking the laser, atom and cavity set-up involves the use of a far-detuned stabilisation laser and 'transfer cavity' in addition to the probe beam. This technique is described in reference [104], and will be covered in chapter 5.

3.4.5 Detection Efficiency

Discriminator Position

Having identified regions of parameter space that maximize the signal-to-noise ratio, a further question for signal analysis regards the separation of a detection event from the shot-noise of the empty cavity transmission, indicated with the dotted 'discriminator' line in figure 3.1(b).

Variations in the number of photons counted in a measurement interval of 20μs, for an empty cavity, are photon shot-noise fluctuations. So far, we have considered the same to be true of the number of counts from the cavity during an atom transit, and the two Poissonian distributions are related by the signal-to-noise ratio. The quantum efficiency and false count rate of the atom detection depend on the value chosen to distinguish between these photon distributions. As an illustration, for a resonant signal (where the detected photon number during an atom transit is less than that of an empty cavity) *raising* the discriminator increases the efficiency since it includes more of the distribution of 'signal' counts, but more of the empty-cavity counts are also included, so the false counts increase. A detailed discussion of this concern is the subject of the following chapter.

Limits to Efficiency

It is important to note the limitations of our model with respect to detection efficiency. We have considered maximal coupling between the atom and cavity field ($g(\boldsymbol{r}) = g_0$), neglecting any variation in coupling strength (and corresponding signal strength) that occurs when the atom transits the cavity away from the intensity maximum of the light field. In a real system, this variation critically affects the quantum effiency. If the low field intensity around the nodes of a standing-wave cavity can be avoided, the coupling strength seen by each atom can be made substantially more uniform. This can be achieved in two ways:

(i) For a non-resonant red-detuned probe, the electric dipole force can be used to pull the atoms through the intensity maxima of the cavity mode. The dipole potential is proportional to the field gradient, so the rapid intensity changes of a standing-wave can create a strong force along the cavity axis. On the basis of our modelling, we expect the regime of point B in figure 3.6 would provide both a strong axial dipole potential and a reasonable signal-to-noise ratio that is reduced by a factor of about 1.4 compared to best case resonant detection. There is also a weaker dipole force in the radial direction due to the Gaussian beam profile. In principle, this could increase the effective width of the atom detector. Assuming reasonable atom speeds of about 1 m/s, however, the radial dipole force is not strong enough to substantially influence the atom trajectories. This is true both for the regimes considered here and in other work [104].

(ii) Only linear cavities have axial mode structure. A travelling-wave ring cavity has a field that is uniform along the cavity axis. Consequently all atoms transiting the field on-axis generate signals of the same strength. In this configuration, there is little to be gained from using red-detuned light since the dipole force acting on the atoms will only be in the radial direction, and, as discussed above, unable to significantly influence atom trajectories. A travelling-wave cavity therefore seems highly suited to resonant detection where the signal-to-noise ratio is maximised. The only downside is that the lack of standing-wave structure yields a mode volume twice that of a linear cavity with the same round-trip length. This reduces g_0 by a factor of $\sqrt{2}$. Our modelling indicates that for both resonant and detuned detection with optimum probe power, travelling-wave cavities lose a factor of 1.3 to 1.5 in signal-to-noise ratio compared to standing-wave cavities with otherwise identical properties.

In summary, non-resonant detection allows one to use a linear cavity with a standing wave and higher g_0, but one is forced to consider red-detuned detection, which has lower potential signal-to-noise ratio than the resonant system. Alternatively, a ring cavity with no standing wave, is better suited to resonant detection, but comes at a cost of potential signal-to-noise ratio due to the reduction in g_0. The end result is that both options give similar performance.

Although there are many experimental details that we have not considered in the present work, our model is still useful for comparing real set-ups. For example, Öttl *et al.* detected single atoms in a rubidium 87 atom laser beam using a high finesse ($\mathscr{F} = 3.5 \times 10^5$) optical standing-wave cavity, with $L = 178\mu$m, w$_0$ $= 25.5\mu$m [104]. Their detection made use of the dipole force to channel the atoms through antinodes of the cavity field, and optimum detection efficiency occured for detunings of $\Delta_a = 3\gamma$ and $\Delta_c = 0.5\kappa$ with a driving photon flux of 70 photons/μs. In our simulations, these cavity parameters and operating conditions suggest an ideal signal-to-noise ratio for single atom detection of about 10. Their cavity is appropriate for many experiments besides single atom counting since it accomplishes strong coupling conditions [103]. The cavity design that we have discussed here has a finesse that is an order of magnitude lower ($\mathscr{F} = 10^4$) than the cavity presented in the work by Öttl *et al.* Nonetheless, we have demonstrated that for our moderate finesse, there exist operating regimes, in both resonant and detuned conditions, where the achievable signal-to-noise ratio is as good as that of the higher finesse cavity. The critical difference between the optimum operating regimes used in reference [104] and those shown in this work, is the use of high probe powers necessitating detection with a heterodyne set-up.

3.5 Conclusions

In this chapter, we have presented a thorough analysis of factors influencing the signal-to-noise ratio for single atom detection using optical cavities. The parameter space considered includes cavity-probe and atom-probe detunings as well as variable probe power, and we have shown that the signal-to-noise ratio for single atom detection is critically dependent on the choice of operating regime within this space.

Our modelled data suggest the parameter space be divided into two regimes: resonant and non-resonant detection. Resonant detection with moderate to high-finesse cavities (systems with low critical atom number) is best described with the Jaynes-Cummings mode-splitting. Non-resonant detection results in a frequency-pulling of the cavity transmission line that can be observed *via* a change in transmitted power, or phase.

The best signal-to-noise ratio occurs on-resonance. However, very reasonable signal-to-noise ratios are also available with non-resonant conditions, provided the atom and cavity detunings are chosen wisely and combined with appropriately high probe powers. With a standing-wave configuration, red-detuned detection brings the benefit of the dipole potential that improves the effective atom-cavity coupling, however, equivalent signal-to-noise ratios are achieved with resonant detection in a travelling-wave ring cavity.

We have shown that accessing the maximum values for the signal-to-noise ratio for both resonant and non-resonant conditions requires photon fluxes that are in excess of APD saturation limits, so heterodyne detection is a more desirable detection technique, as well as allowing the possibility of phase measurements. Working in high power regimes means that for a cavity of moderate finesse, $\mathscr{F} = 10^4$, we can achieve a signal-to-noise ratio comparable or better than those achieved in previous experiments using cavities with significantly higher finesse.

In the next chapter, we will extend our analysis to atom trajectories through the cavity field, taking into account the dipole force as well as the cavity mode structure and experimental data for the spatial profile of our atom laser beam.

CHAPTER

FOUR

DETECTION QUALITY: MEASURING SQUEEZING IN AN ATOMIC BEAM

In this chapter, we analyse the quantum efficiency and dark noise of our modelled single-atom detector, with particular emphasis on the ability to measure number squeezing in an atom laser beam. We consider the influence of the electric-dipole force on an atom in a red-detuned detection beam, and discuss the much improved detection efficiency for detuned probes, with respect to resonant probes, resulting from this influence. We find that for the detection scheme introduced in chapter 3, and working in the regimes suggested from the data presented there, a noise-floor clearance of more than 20dB is achievable. Cavities allow real-time monitoring of atomic flux, with single-atom resolution, but they are much slower than their analogue in photonics - the avalanche photodiode, so flux limits must be imposed. The proposed detector operates at a maximum flux of 5000 atoms/second, but with the available shot-noise clearance, the full advantage afforded by number squeezing in particle flux can be observed.

4.1 Introduction

Interferometry using massive particles is receiving increasing interest as a means to precision measurement because of the possibility of hugely improved precision offered by devices using massive particles over their traditional photonic equivalents [59]. At its core, atom-interferometery relies on a quantum system that is prepared in a super-position of two states which evolve under a given Hamiltonian at different rates [39]. After some free evolution the populations of each state are measured. The key observable is then inferred from the measured population difference between the two.

As with optical measurements, signal-to-noise ratios - and the resulting interferometric sensitivity - improve with increasing particle flux. Sensitivity can be enhanced using 'squeezed' states in which the fluctuations in a particular variable are below the standard quantum limit [57]; the corollary being that they are larger in the conjugate variable, in accordance with Heisenberg's uncertainty principal [41, 84]. Although squeezing the quantum noise on optical lasers has been an active field of research for more than 20 years, and the field has produced many beautiful results, it has never improved the sensitivity of a practical measurement apparatus. The reason is simple. Coherent photons are cheap and easy to produce, and it has always proved better to turn up the photon flux rather than squeeze the source to improve the precision and accuracy of a measurement. This may change in the near future with the implementation of squeezed sources in advanced LIGO [50, 54]. Atom sources are somewhat different, and the prospects for exploiting squeezing in practical measurements look rather more promising since cold atoms are expensive to produce.

A laser pointer that you can buy for a few dollars produces 10^{16} photons per second and fits in the palm of your hand. In contrast, a cold atom source appropriate for precision measurement has a flux eight orders of magnitude below the laser pointer, a cost five orders of magnitude higher and the apparatus is three orders of magnitude larger. Unless we find new technology to increase the flux of cold atom sources, whether they are Bose condensed or cold thermal sources, it is unlikely that we will be able to substantially increase the signal-to-noise in atom based measurements simply by turning up the atom flux.

Squeezing becomes a viable candidate with such a set of conditions. There are other aspects that make squeezing look promising. Mechanisms for squeezing proceed *vai* interactions or non linear terms in the Hamiltonian. Photons do not interact with photons in vacuum and require a substantial engineering effort to produce a non-linear medium capable of substantial squeezing. Atoms interact with each other and squeeze for free, and a variety of mechanisms has been proposed for the production of squeezing in atomic beams [62, 26, 43, 132, 90, 84]. A further complexity in optical squeezing is the immense susceptibility to loss due to scattering and absorption in a typical lab environment. The vacuum chamber required for a cold atom experiment is a sunk cost. We may as well take advantage of it and use this low loss, clean environment with squeezed atomic sources. The realisation of spin-squeezed states of a two-component Bose Einstein condensate have recently been demonstrated experimentally [57, 116].

As well as interferometric measurements, there is great interest in the production of entangled atomic beams for quantum-information processing and fundamental tests of quantum mechanics with massive particles. In quantum optics, many important validations of quantum mechanics have occurred using photons and photon counters including Bell state measurements and realisation of the EPR gedanken experiment [12], quantum teleportation [20] and Bell-type inequality violation for single particles [89]. In contrast to interferometric set-ups that use photodiodes (PDs) to measure high photon fluxes, these exotic quantum phenomena are observed with the aid of single photon detectors such as avalanche photo diodes (APDs). Demonstrations of such effects using atomic sources require the atom-optics equivalent of an APD. Micro-channel plate detectors are a good option for energetic atoms [127, 148], but currently no options exist for neutral atomic species.

One standard tool for detecting cold atoms, is absorption imaging, a technique that might be considered analogous to PDs used in quantum optics since imaging of large numbers at the shot-noise-limit is possible. With sufficient optical depth and an optimised imaging set-up, fluxes of 10^7 atoms/sec have been measured [8]. However, the technique does not lend itself well to the detection of dilute atomic samples, so cannot be extended to the regime of high efficiency single-atom counting. Also, unlike PDs, absorption detection is not continuous, as the acquisition of an image takes on the order of 100ms, limited by the download time of the camera used.

In this chapter, we will show that cavity-based atom detection could fill this technological gap. Additionally, even relatively moderate finesse cavity detectors can be designed to have a quantum efficiency close to unity, compared to 80% for the best available single photon detectors. Consequently, cavity-based detectors could also be used for continuous variable quantum measurements (e.g. squeezing) where high quantum efficiency is crucial [13].

No matter what its nature, in any device aiming to probe the statistics of an atomic ensemble, it is important to detect atom numbers at the shot-noise limit. The head-room between the atomic shot-noise and the inherent noise of the detector - the 'noise-floor clearance' - will determine the sensitivity of the device. This will be our figure of merit in analysing our detector. Cavity-based single-atom detectors have already been successfully used to probe the statistics of a coherent atomic source in real-time [103], but a clear demonstration of their further potential has yet to be presented.

In the previous chapter, we investigated the signal-to-noise ratio for the detection of an atom *maximally* coupled to the single-mode of an optical cavity. In reality, not all atoms falling through a detection cavity experience maximal coupling, and an analysis of the atomic trajectories is important in determining the quantum efficiency of the detector and its ability to measure number squeezing. Our aim in this chapter is to develop our understanding of the optimal signal-to-noise ratios into a full discussion of the achievable noise-floor clearence offered by this system of single-atom detection.

- We begin in **section 4.2** with a general discussion of squeezing measurements, considering the variance of a Poisson distribution as compared with a squeezed source of any quanta - atoms, or photons.
- In **section 4.3** we outline the sequence of processes used in our modelling to determine the quantum efficiency and dark noise of the detector.
- In **section 4.4** forces influencing the atomic trajectories through the cavity are discussed.
- The role of these trajectories in optimising the detection efficiency is presented in **section 4.4.3**.
- **Section 4.4.4** discusses the use of a discriminating threshold for signal determination and **section 4.4.5** its influence on noise-floor clearance.
- We finish the discussion in **section 4.5** by consideration of the geometric overlap of the atom laser beam and optical detection mode.

In the work presented in this chapter, where reference is made to 'resonant' and 'detuned' detection, it is to the following operating regimes, determined from the investigations of chapter 3, that we refer: for resonant detection, where

$\Delta_c = \Delta_a = 0$, the optimal operating power is roughly 40 photons/μs or an intracavity photon number of $n_0 = 0.08$, and the best attainable snr is about 13. Nonresonant, or 'detuned' detection can give good snrs provided the probe power is increased. Detuned detection covers a large parameter space. Here we refer to the values: $\Delta_c = -1\kappa$, $\Delta_a = 25\gamma$ and an input photon flux of ~ 6300 photons/μs ($n_0 = 6.7$), giving an optimal detection snr of approximately 8.

4.2 Measuring Squeezing

An atom-laser beam, like an optical laser, exhibits a Poisson distribution in the number of particles measured in a fixed time [85]. Indeed, the following discussion concerning squeezing measurements merely follows statistical arguments. The nature of the particles (photons or atoms) is irrelevant, and the analysis applies to any detector that displays the usual physical constraints of limited efficiency and fidelity, and saturation.

4.2.1 Counting Statistics: What Do We Measure?

The mean number of particles, N, counted in a fixed measurement period (let us say one second of data collection) depends on the power in the atom-laser beam - that is, the atomic flux. The fluctuations in this number, over repeated measurements, are given by its variance, V. For a coherent source, exhibiting Poissonian statistics, the variance is equal to the mean, whereas in a squeezed beam it is reduced, so that the numbers found in each measurement are more closely distributed about the mean. It is convenient to define the normalised variances for coherent and squeezed sources as $V_c = 1$ and $V_s < 1$. With this representation, the real variance, which scales with the power, is $V_1 = NV_s$ for a squeezed source, and $V_2 = NV_c$ for a coherent source.

To measure squeezing it is necessary to determine the difference in observed variance to that of a Poisson distribution, and the parameter of interest is the ratio V_1/V_2. For a coherent source, $V_1/V_2 = 1$, and the ratio decreases as the squeezed variance is reduced. The amount of squeezing on the atomic source can be defined in decibels by the parameter

$$S = -10\mathrm{Log}_{10}(V_1/V_2)\mathrm{dB}. \tag{4.1}$$

However, the variance that is measured at the detector differs from the actual variance of the atomic source: False, or 'dark', counts occur at a rate that is influenced by the position of a discriminating threshold, illustrated in Fig. 3.1(b). They have a Poisson distribution, with variance V_{dark}, since the probe laser in the empty cavity is itself a coherent source. Also influencing the measured statistics, is the fact that some atoms are not counted if the quantum efficiency, η (whose value is also determined with the position of the discriminator) is not 100%.

The observed variance of a squeezed source, measured with imperfect efficiency η, is therefore given by [25]

$$V_1 = V_{\text{dark}} + \eta N(\eta V_s + (1-\eta)V_c) \tag{4.2}$$

As squeezing is reduced to zero, $V_s \to V_c$. For a coherent source the measured variance becomes

$$V_2 = V_{\text{dark}} + \eta N V_c \tag{4.3}$$

The Poissonian statistics of the dark counts will dominate if the false-count rate is too high or the detection efficiency, η, is too low, and deviations in the atomic flux statistics will be obscured. The squeezing parameter S, is therefore an indicator of the amount of squeezing *measured* for a given squeezed source. Our aim is to find a position for the discriminating threshold that results in the best measurement for a fixed amount of squeezing in the source by optimising the squeezing parameter.

4.2.2 Detector Saturation: Limiting the Atomic Flux

Since the measured statistics depend on the atomic flux, we first need to choose a reasonable value of N to suit the detector. We consider a coherent source of atoms and a 'perfect' detector with no dark noise ($V_{\text{dark}} = 0$), and an efficiency of 100% ($\eta = 1$). The limitation to the performance of such a device is the measurement time in the detection process. A reasonable integration time for the cavity-detector that we model is 20μs [55]. Faster detection times are certainly possible, but require higher-finesse cavities.

For $\tau = 20\mu$s, there are 50000 measurement 'bins' per second of data collection, each of which we assume can count the presence of at most one atom. This does not mean we can accept a flux of 50000 atoms/s, since for a source with a Poissonian distribution, this would result in multiple atoms arriving at the cavity in the same time bin, and unresolved transits.

The probability, P, that an individual time-bin measures a transit, increases with the atomic flux as

$$P = 1 - \left(\frac{m-1}{m}\right)^{N} \tag{4.4}$$

where N is the number of atoms arriving at the cavity per second, and m is the number of time bins per second, which we have fixed to 50000, for our $20\mu s$ detection time. Here, the denominator accounts for the m^N possible ways that an atomic transit can be distributed into a random time bin: the distribution is random since we start by considering the Poissonian distribution of a coherent atomic source. The numerator counts the number of possible distributions into remaining empty bins after N such randomly distributed transits.

Alternatively, the probability $P' = 1 - P$ that there remain unfilled, or empty, time bins (that the detector is not 'saturated') decreases with flux:

$$P' = \left(\frac{m-1}{m}\right)^{N} \tag{4.5}$$

As the atomic flux increases, the detector saturates, and the measured variance ($P' \times V$) drops to zero. This is because when all the time bins are filled, increasing the atomic flux does not change the number of counts. We know that the *real* variance for a Poisson distribution must grow continually, since $V = V_c N = N$. Figure 4.1 shows the deviation of the measured variance from the real variance, for a perfectly efficient, noiseless detector. If we use a high atomic flux that saturates the detector, the measured variance is lower than that of a Poisson distribution, despite the lack of squeezing in the source.

We would like the atomic flux to be the highest possible before the detector saturates, since the signal-to-noise ratio improves as $N^{1/2}$. The optimum value is established when the measured variance does not deviate too far from the actual value: the inset in Fig. 4.1 shows where the difference between the measured variance and the actual variance starts to become significant. At a value of $N = 5000$ (ie: a flux of 5000 atoms/s) the deviation is about 5%.

We emphasise this flux-limit: restricting flux will limit the atomic signal-to-noise ratio of a measurement, and sensitivity of an interferometric measure. If a squeezed source is used (and provided the squeezing can be measured at the

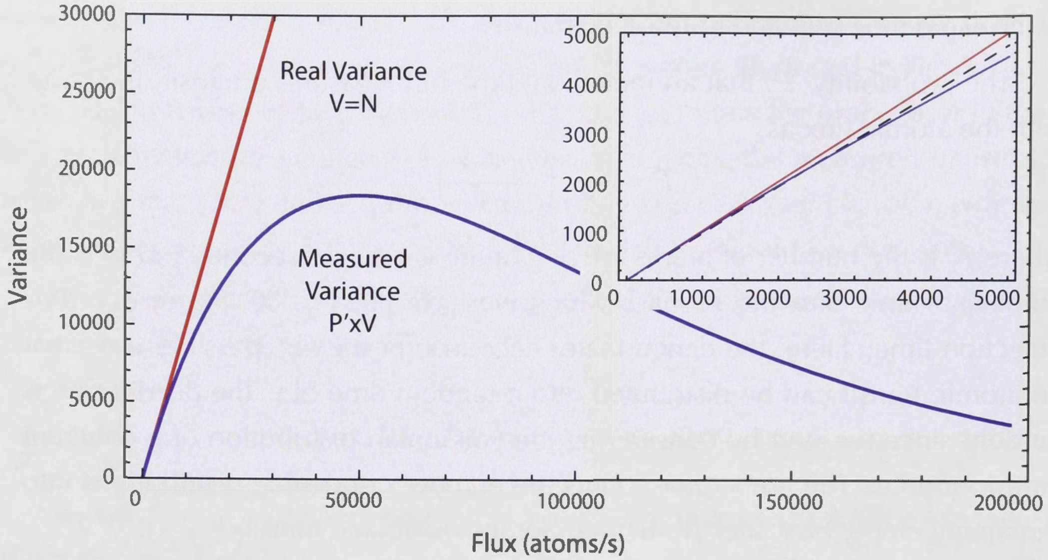

Figure 4.1: Measured and actual variance of atoms for one second of measurement time, as a function of atomic flux. The inset indicates the atomic flux at which these values begin to differ significantly. The dashed line indicates deviation of 5% from the actual variance.

detector) then the signal-to-noise ratio can be regained, and even improved. The experimental difficulty is therefore transferred from one challenge to another: rather than striving for high atomic-flux, we require squeezed sources.

It is worth noting that our imposed atomic flux-limit is much lower than photon fluxes measured with instruments such as avalanche-photo diodes. However, APDs *do* saturate and are limited to lower photon-fluxes than photodiodes used in heterodyne/homodyne set-ups. Ultimately the limitation arises from the detector measurement time, τ. The cavity-based detector discussed here is slow (20μs) in comparison to photon detectors, but dramatically faster than other atom-detection processes, such as absorption imaging, and they allow continuous monitoring in real-time. A higher finesse cavity can operate with a faster detection time [110], potentially allowing much less restrictive limitations on the atomic flux.

4.3 Modelling Detection Quantum Efficiency

Having established an acceptable value for atomic flux, we return to equations (4.2) and (4.3), to evaluate the ratio V_1/V_2 for our real detector - with false counts and limited quantum efficiency included. These imperfections are variables influenced by the chosen position of the discriminating threshold, illustrated in Fig. 3.1(b). To quantitatively determine the optimal position, an understanding of the statistical distribution of real and false signals is required.

The modelling of these quantities is involved. Let us summarise the sequence of procedures used in characterising the detector:

1. The photon number in the cavity is calculated (using equation (3.1), and the process described in section 3.2.1), for a three-dimensional grid of atom positions in the cavity mode. Interpolating these values gives a function for the field intensity. That function includes changes in the intensity due to the presence of the atom, as well as the Gaussian, standing-wave structure of the cavity mode.

2. An atom is assigned an 'entrance position' to the cavity mode, at some position in the x, y-plane. The height above the cavity axis at which we consider 'entrance' is twice the cavity beam-waist size: $z(0) = 2\mathrm{w}_0$.

3. A trajectory (and its resulting signal strength) is calculated for this atom, taking into account the deterministic forces as well as the stochastic spontaneous emission events, and a 'mean' path is determined by averaging several such stochastic paths. The process is repeated for a range of atomic entrance positions.

4. The likelihood of each entrance position depends on the transverse spatial profile of the atomic source. Taking this into account we can assign a probability of a given signal strength.

5. Quantum efficiency and false counts are established by considering signal strength in conjunction with a discriminating threshold.

4.4 Forces: Atomic Trajectories

The position- and consequent time-dependent forces on the atom, and the resulting centre-of-mass motion during a transit, are calculated using a series of steady-state solutions to the master equation. This is therefore a *semi*-classical model in which the exchange of energy quanta between the cavity field and atom is treated quantum mechanically using equations (2.25) and (2.15), but the atomic motion is found using classical formulae for the gravitational and electric-dipole forces, discussed in the following sections. The approach is justified because the localisation of the atom upon entering the cavity mode is rapid with respect to its motion and transit time [19, 117]. In other words, the atom enters the cavity as a waveform that is spatially extended over the cavity mode, with a probability distribution determined by the atom laser beam profile. However, once the first photon is scattered during the detection process, the atom can be thought of as a classical particle, localised within the cavity. The process can be considered as an unread measurement: if the scattered photon were to be detected (for example, with a fluorescence detection set-up), the atomic wave function would be projected onto a particular location. Thus classical parameters describing the atomic motion are appropriate. The greater the scattering decoherence term, γ, the faster this localisation occurs, even when the photon is not detected.

4.4.1 The Gravitational Force and Spontaneous Emission

In the simplest model, corresponding to resonant detection, the gravitational force determines the centre-of-mass motion of atoms in the cavity volume, providing a constant acceleration in the downwards vertical direction. The atom also experiences 'kicks' in random directions due to the conservation of momentum during spontaneous emission. In our system, the number of spontaneous emission events during a transit is not so large as to result in significant accumulated momentum, but kicks do have the ability to skip atoms the small longitudinal distance between nodes and antinodes. The spontaneous emission rate (proportional to the atomic saturation) scales with the field intensity, so it changes during the transit, as the atom passes through different positions within the mode.

Figure 4.2(a) shows example transits of atoms through different regions of the cavity mode, with a resonant probe beam. The variations of paths demonstrate the stochastic influence of spontaneous emission on atoms entering the cavity at the position of an antinode ($0.1\lambda/4$ from a node) in blue (red). In the case of atomic transits that pass close to a node, the field amplitude and atom-field coupling strength are near zero, and such transits are detected only weakly if at all. For optimum detection efficiency then, it is clearly important to avoid the nodes of the cavity mode.

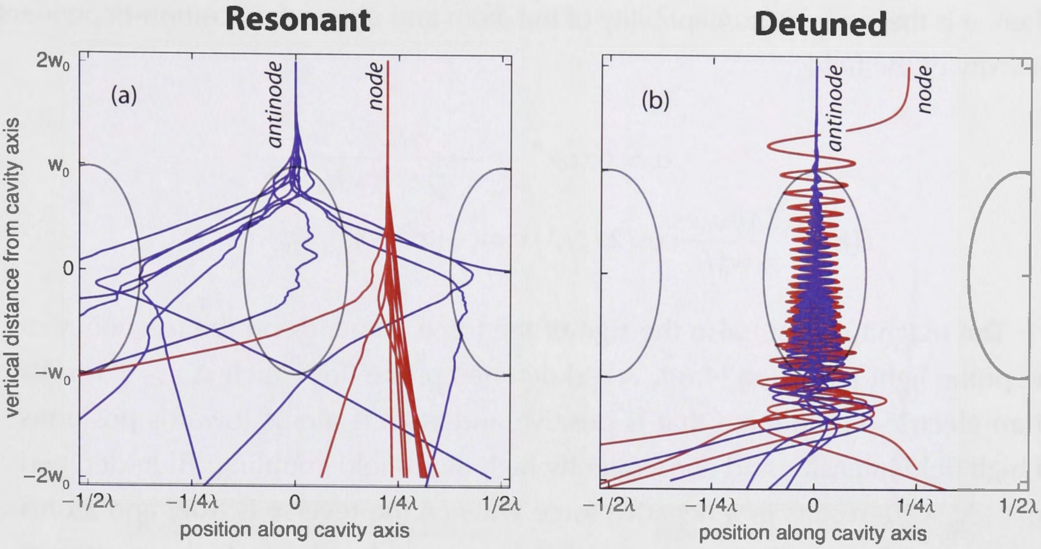

Figure 4.2: Atom trajectories through the resonator mode. The conditions modelled are for (a) resonant and (b) detuned detection. The atom entrance velocity is $\boldsymbol{v} = -1(m/s)\hat{\boldsymbol{y}}$. Blue traces are trajectories of those atoms entering the mode directly above an antinode, and on-axis in the radial direction, while red traces show atomic transits for atoms entering the cavity a longitudinal distance of $0.1\lambda/4$ from a node. Ellipses represent the cavity mode at positions where the field intensity is half its maximum. Note the vastly different scales on the plot axes: the cavity waist, $w_0 = 20\mu$m, while the standing-wave structure is on the order of the wavelength used (less than one μm).

4.4.2 The Electric-Dipole Force

Generally, atomic trajectories are influenced by more than the gravitational force and spontaneous emission alone. When the probe light is detuned from the atomic transition, atoms may experience a strong electric-dipole force resulting from the interaction between their induced dipole moment and the electric field. This force is important to inspect since it can be large, and is influenced directly by the field intensity and by the detuning of the probe from the atomic transition. Classically, it is given by [56]

$$\boldsymbol{F}_{\text{dip}}(\boldsymbol{r}) = \frac{1}{2\epsilon_0 c} Re(\alpha)\nabla I(\boldsymbol{r}) \tag{4.6}$$

where α is the complex susceptibility of the atom and $I(\boldsymbol{r})$ is the position-dependent intensity of the field:

$$\alpha = 6\pi\epsilon_0 c^3 \frac{\gamma/\omega_a^2}{\omega_a^2 - \omega_0^2 - i(\omega_0^3/\omega_a^2)\gamma}$$

$$I(\boldsymbol{r}) = \frac{4n\hbar\omega_0 c}{\pi \mathrm{w}_0^2 L} \cos(2\pi z/\lambda) \exp(-(x^2+y^2)/\mathrm{w}_0^2).$$

The magnitude, but also the sign of the force, depends on the frequency of the probe light [equation (4.6)]. A red-detuned probe (for which $\Delta_a > 0$) results in an electric-dipole force that is positive and attracts atoms towards positions of high field intensity, and consequently high atom-field coupling. Blue-detuned light ($\Delta_a < 0$) results in a negative force whence the reverse is true, and atoms are repelled from such regions. For the situation at hand, in which we attempt to avoid the nodes of the resonator mode to increase the quantum efficiency, we will consider only red-detuned light.

The net force on the atom during its transit is a combination of the constant gravitational force and the dipole force that varies with field intensity and therefore with atomic position, as well as the stochastic spontaneous emission events. The complexity of the situation is compounded by the fact that the intra-cavity photon number (intensity) is itself influenced by the coupling of the atom to the field, the strength of which we know to be position-dependent.

An atom falling *directly* through nodes or antinodes sees no longitudinal force, since the gradient of the potential is zero at these positions. For all other positions, the dipole potential provides a restoring force towards the nearest intensity maximum (for a red-detuned field), and the atom oscillates about that antinode as it falls through the mode.

Figure 4.2(b) shows examples of atomic transits of the cavity mode for a red-detuned probe laser. We find that for the beam parameters modelled, *all* near-axial atoms falling through the detuned beam are channelled into local intensity maxima (antinodes) of the field, even when the longitudinal entrance position is very close to a node (red traces). This is important: consider, for example, comparing the red traces in figure 4.2(b) with 4.2(a). With a detuned probe, the average coupling strength experienced by an atom during its transit is higher than that for the transit of a resonant probe beam, with an identical entrance position. The effect has been observed experimentally in the group of Tilman Esslinger,

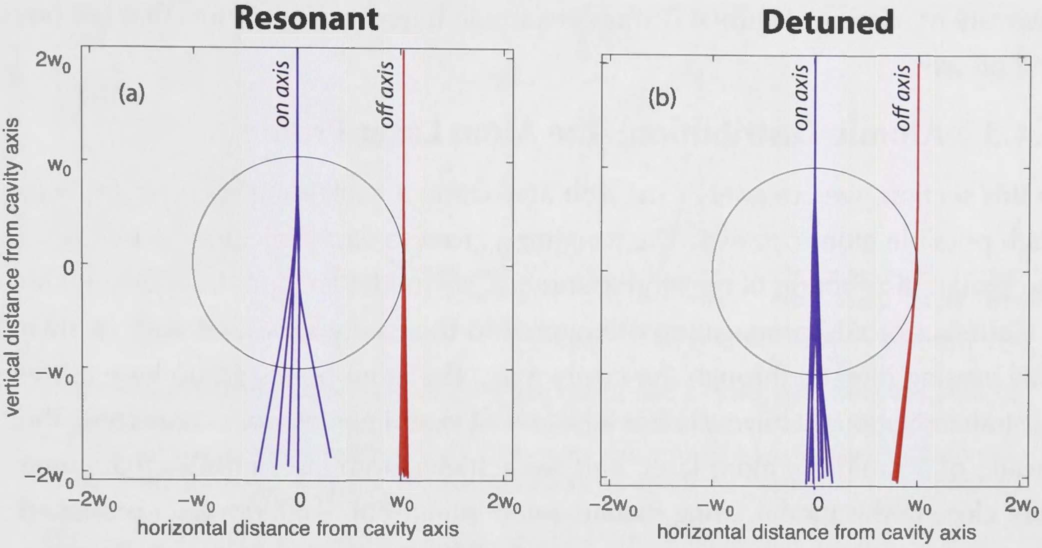

Figure 4.3: Atom trajectories through the resonator mode. The conditions modelled are for (a) resonant and (b) detuned detection. The atom entrance velocity is $\boldsymbol{v} = -1(m/s)\hat{\boldsymbol{y}}$. Blue traces are trajectories of those atoms entering the mode directly above an antinode, and on-axis in the radial direction, while red traces show atomic transits for atoms entering the cavity a radial distance of one cavity-waist from the axis. The view is shown looking down the cavity axis, and the circles represent the cavity mode at positions where the field intensity is half its maximum.

that reported improved detection efficiency for red-detuned probes, on account of effective channelling of atoms into cavity antinodes [104].

The dipole force *along* the cavity axis can be tremendously significant, since the intensity of the field varies rapidly with the standing-wave structure of the mode, resulting in a large value for $\nabla I(\boldsymbol{r})$. The scale of the standing-wave is determined by the wavelength, λ, of the light used, which at optical frequencies, is less than one micrometer. In the radial direction, perpendicular to the cavity axis, the field strength changes less rapidly, dropping to the half-maximum intensity at $r = \mathrm{w}_0$. Consequently the force is much weaker in that direction.

For the system we consider, w_0 is typically around 20μm, and $\lambda = 780$nm. The maximum dipole force in the radial direction is numerically determined to be on the order of 10^{-22}N, while along the cavity axis it can be up to 10^{-19}N, except at the exact positions of nodes and antinodes where the potential has zero gradient. The gravitational force is about 10^{-24}N for a rubidium 87 atom, which weighs 10^{-25}kg. In the radial direction, the dipole force deflects some atomic transits, but is not sufficient to channel far-off-axis atoms through the radial intensity maximum. Figure 4.3 shows example trajectories of atoms that fall on- and off-axis.

4.4.3 Atomic Distribution: The Atom Laser Profile

In this section, we are concerned with attributing a 'weighting' or probability to each possible atomic transit. The weighting given to each trajectory depends on the spatial distribution of the atomic source. We model an atom laser beam with a Gaussian profile propagating orthogonal to the cavity axis, and with its own axis passing directly through the cavity axis. The atom optics group here at the Australian National University has a history of experimental work concerning the profile of a rubidium atom laser, and we achieve atom laser profiles that come very close to this model, using Raman outcoupling [78]. An atom laser produced *via* an optical Raman transition, rather than radio-frequency (rf) outcoupling, can have a high beam quality and avoid the significant divergence that usually results from the lens effect of the condensate on the outcoupled atoms: by using near-counter propagating Raman beams, the momentum transferred to the outcoupled atoms approaches $2\hbar k$, rather than the zero momentum transfer of rf outcoupling. This means that atoms leave the condensate much faster than if they are simply falling under the influence of gravity, and there is no substantial time for the condensate mean field to interrupt the outcoupled beam profile.

Figure 4.4 shows a histogram of the relative probability of transmitted photon numbers measured at the cavity output mirror during an atomic transit from a Gaussian atom laser beam with a waist of 10μm (half the cavity waist size). The atoms are travelling at 1m/s. We also show the histogram for photon numbers from the empty-cavity.

These plots contain a lot of information. The empty-cavity photon distribution (red, dashed trace) is Poissonian, reflecting the fact that we have modelled the probe as a coherent, shot-noise limited beam. The histogram for photon numbers measured *during* an atom detection event (solid, blue trace) includes the Poissonian statistics of the probe beam but is convoluted with the distribution of effective coupling strengths, determined by the atomic entrance positions and resulting trajectories. In the case of a resonant probe beam [figure 4.4(a)], the histogram for detection events is a good indication of the variation in coupling- and signal-strengths experienced by atoms whose transits are *not* influenced by a dipole force. A large range of possible output photon numbers may be mea-

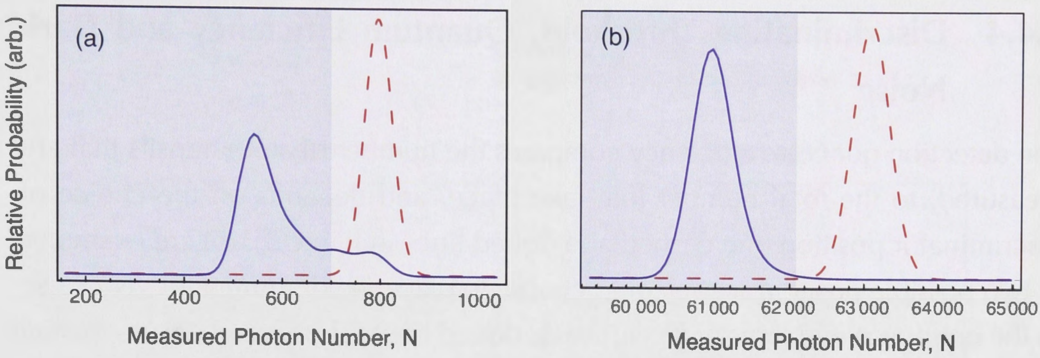

Figure 4.4: Photon distributions for an empty cavity, and a cavity with weighted atom transits. The y-axis shows the relative probability of measuring a certain photon count (x-axis) within the set integration time. The cavity mode waist is $w_0 = 20\mu m$ and atom laser beam waist $w_a = 10\mu m$. The dashed traces represent the Poissonian distribution of photons measured in $\tau = 20\mu s$ from the empty cavity. The solid, blue traces are for (a) resonant detection, and (b) detuned detection. The solid trace is a convolution of Poissonian distributions about the various output values for different atom transits, and the probability distribution of those transits. Shaded regions represent discriminating detection thresholds placed (a) ~ 3.3 and (b) ~ 3.9 standard deviations below the mean photon number of the empty-cavity.

sured, depending on the atom entrance position. The significant distribution of weak signal strengths (close to the empty-cavity photon number) reflects the fact that there are more possibilities of an atom transit experiencing weak coupling, rather than strong. Strong coupling is achieved only *on-axis and* in the vicinity of an antinode, whereas weaker coupling results from the wide range of off-axis positions, regardless of longitudinal location with respect to the standing-wave structure.

In figure 4.4(b), the advantage to signal strength afforded by the dipole force is evident. In this scenario, most atoms experience similar coupling strengths, close to the maximum value, g_0, regardless of their entrance position, since they are very effectively channelled into oscillations about the high-intensity, high-coupling locations in the resonator mode, as shown in figure 4.2(b). There is consequently very little variation in the signal strengths, and the histogram for these detection events is much less extended, and more closely represented by a Possionian distribution centred on a unique value.

4.4.4 Discriminating Threshold, Quantum Efficiency and Dark Noise

The detection quantum efficiency compares the number of atom transits that are measured, to the total number that take place, and depends on the choice of discriminator position (the dashed and dotted lines in figure 3.1(b) are examples of two possible positions). We could choose to place the discriminator very close to the empty-cavity intensity level (heavy, dotted line). This would ensure that *all* atomic transits are counted, since even those that experience only weak coupling, will generate signals that lie below the chosen threshold. Clearly, this is not a reasonable procedure. Although the quantum efficiency is increased, so too is the false-count rate: shot noise from the empty-cavity photon signal may also fall below the discriminating value, and contribute to 'false', or dark, counts that do not correspond to real transit events. To reduce these false counts, it is preferable to move the discriminating threshold *away* from the empty-cavity intensity level (light, dashed line in figure 3.1(b)). The chosen discriminating threshold position must be a compromise of these considerations. A good compromise requires the distributions of power levels from the empty-cavity and the cavity during an atom transit, to be well separated. This allows us to achieve high quantum efficiency in conjunction with a low false-count rate.

The shaded regions in the plots of figure 4.4 indicate discriminating thresholds at roughly 3.3 standard deviations below the mean empty-cavity photon number for the resonant probe beam, and 3.9 standard deviations below the mean for detuned detection. That is to say that even when the atomic flux is zero, and the cavity is definitely empty of atoms, $< 0.1\%$ of the time the measured photon intensity will be recognised as corresponding to an atom transit. These signals are the false counts. The particular choices of discriminating threshold values stated here will be discussed in the following section. The reader is reminded of the difference between detection efficiency and fidelity, as defined in chapter 1. The importance of choosing a discriminating threshold that is a compromise between the conflicting requirements of these parameters will be discussed shortly. A different choice may be made, depending on the requirements of the detector.

For the resonant probe, in figure 4.4(a), the distributions of photon numbers for the empty cavity, and for the cavity during atom transits are not well separated, and with the discriminator position indicated by the shaded area, the quantum

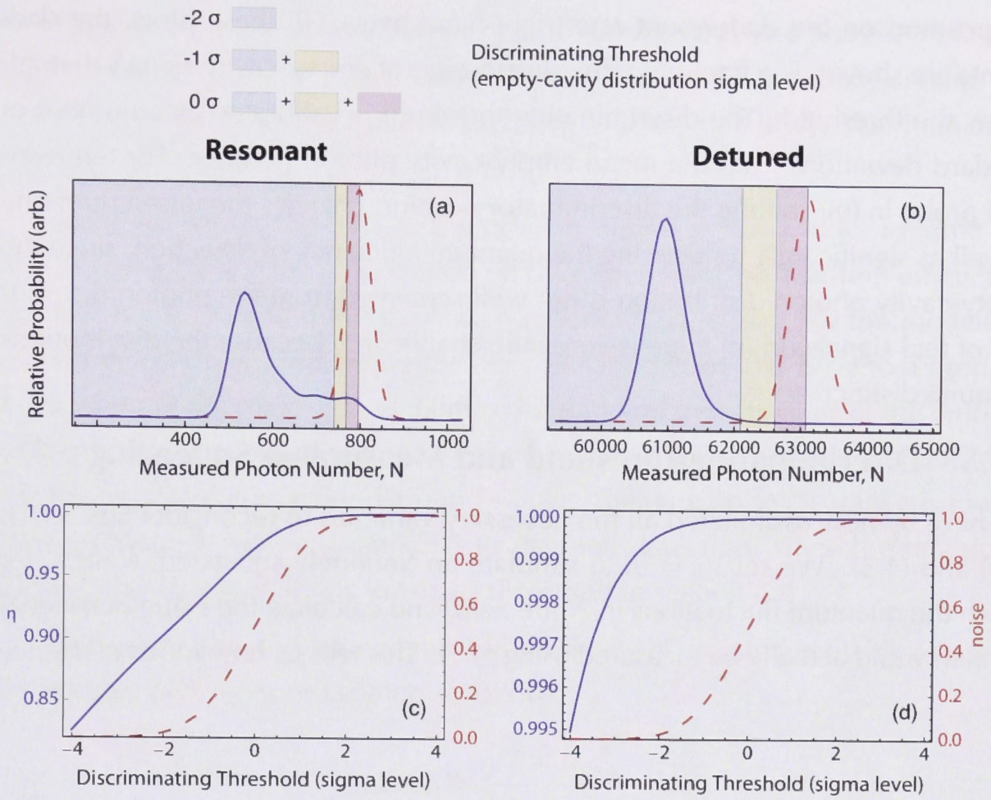

Figure 4.5: Variation in quantum efficiency, η, and dark noise, as a function of discriminating threshold position for detection parameters as in figure 4.4. In (a) and (b), the shaded regions represent a discriminating detection thresholds at positions -2, -1 and 0 standard deviations below the empty-cavity mean photon number. In (c) and (d) the quantum efficiency is seen to increase as the false-count rate increases, although for the *detuned* probe in (b) and (d) it is already very high, even at a threshold position with negligible false-counts.

efficiency is $\eta \sim 0.86$. With the detuned probe [figure 4.4(b)] the distributions are very much more distinct. This means that a threshold photon number lying between the distributions can be chosen to give low false-counts and high quantum efficiency. For the discriminating threshold at the chosen level, almost all ($\eta > 99.5\%$) of the real atom transits are measured.

Figures 4.5(a) and (b) indicate how shifting the position of the discriminator (the shaded region in photon number histograms) changes the percentage of transits that are measured; that is, the quantum efficiency, for (a) a resonant probe, and (b) detuned detection. In figures 4.5(c) and (d) these data are represented graphically (left-hand axes), as well as the influence of the discriminating threshold position on the dark count rate (right-hand axes). In these plots, the dark counts are shown as a fraction of the distribution of *empty-cavity signals* that fall below the threshold. The discriminating threshold is calibrated as a number of standard deviations from the mean empty-cavity photon number. For the resonant probe in (c), shifting the discriminator position changes the false-count rate as well as significantly influencing the quantum efficiency of detection, since the empty-cavity photon distribution is not well separated from the photon distribution of real signals. In (d) there is very little change in η because the distributions are quite distinct.

4.4.5 Discriminating Threshold and Measurable Squeezing

We have by now assimilated all the necessary variables to reconsider Eqs. (4.1), (4.2) and (4.3). We set $V_s = 0$, to simulate an 'infinitely squeezed' source, for which the quantum fluctuations in N are zero, and calculate the value of squeezing that would actually be measured using (4.1). This tells us how much clearance

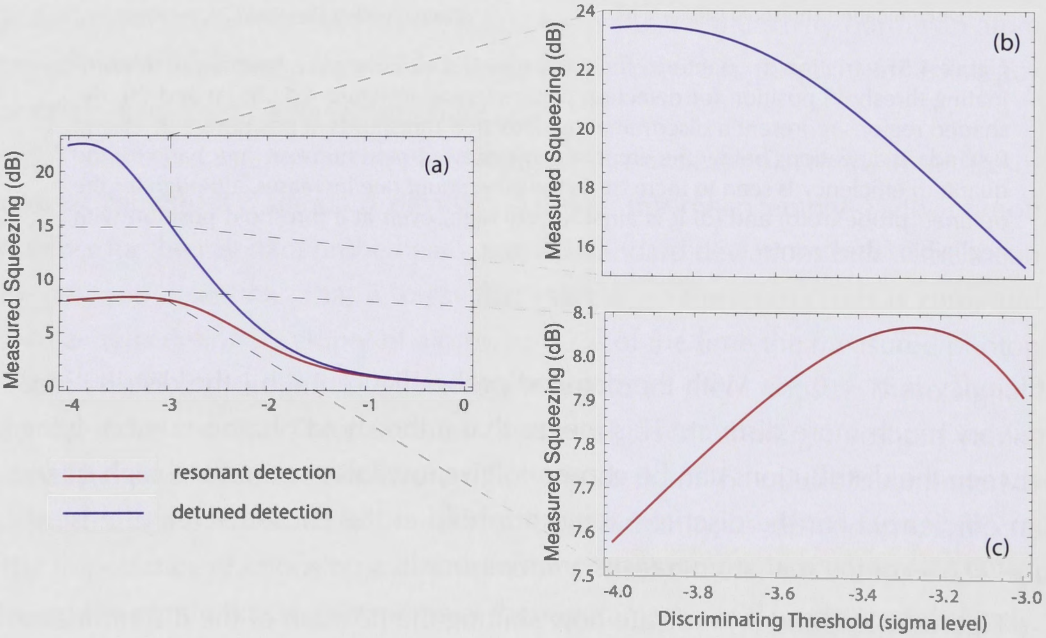

Figure 4.6: Measurable squeezing for a detection integration time of $\tau = 20\mu$s and an atomic flux of 2400 atoms/s. (a) shows the dark noise clearance using resonant and detuned detection, with parameters as in figure 4.4. (b) and (c) show the discriminating threshold positions at which the squeezing measurement is optimised, for these two detection schemes.

we have over the dark-noise of the detector. From the previous section we know that the values for η and V_{dark} depend on the position of the discriminator, so we need to consider the measured squeezing as a function of the discriminating threshold.

Figure 4.6 shows the data in the plots in figures 4.5(b) and (c) in terms of the squeezing parameter, S [equation (4.1)], rather than the quantum efficiency and dark noise. We find the maximum measured squeezing for the modelled detuned detection is 23dB, when the discriminating threshold is set to a drop in transmission of approximately 3.9 times the standard deviation (σ) of the empty-cavity photon shot noise. For resonant detection the maximum value is about 8dB, with the discriminator position around -3.3σ. The dark noise clearance is lower using resonant detection, compared to detuned detection, since the quantum efficiency for that scenario is lower, as discussed in section 4.4.4.

We can consider the improvement in sensitivity of an interferometric measure with the use of a squeezed source as follows:

$$\text{SNR} = \frac{\eta N + N_{\text{dark}}}{\sqrt{V_1}} \tag{4.7}$$

This relation must be solved numerically since η, N_{dark} and V_1 are implicitly connected *via* the position of the signal discrimination threshold.

Figure 4.7 shows the atomic signal-to-noise ratio using the cavity detector with a squeezed source. The detection conditions are the same as those already defined for (a) resonant and (b) detuned detection. As one would expect, in both cases, the signal-to-noise ratio improves as the atomic squeezing is increased. The dashed horizontal line in these plots indicates the experimentally feasible value of 10dB of squeezing on the atomic beam ($V_1 = 0.1$). 8.2dB of squeezing has recently been observed in a BEC [57]. We note that for a perfect detector, where all the squeezing on the source is measured, 10dB squeezing results in a signal-to-noise ratio corresponding to a flux an order of magnitude greater SNR $= \sqrt{50000} \sim 224$. As it is, the measured squeezing depends on the position of the discriminating threshold and the resulting noise-floor clearance of the detector. In the case of detuned detection where we have seen the noise-floor clearance can be significant, the atomic signal-to-noise ratio goes from 70 for an unsqueezed beam ($N = 5000$), up to ~220 for 10dB of squeezing: close to the theoretical

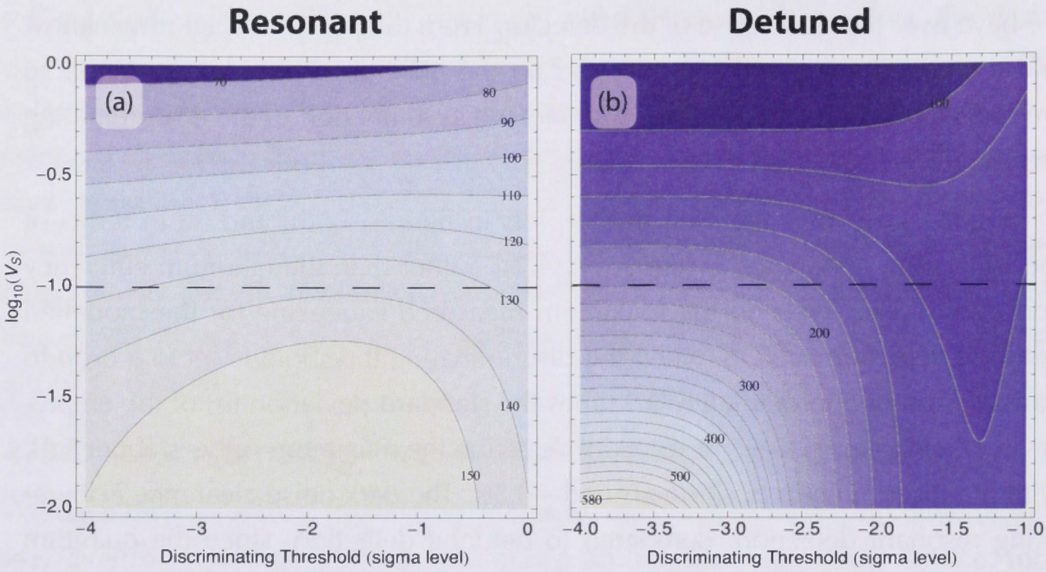

Figure 4.7: SNR for different squeezing levels and varying positions for the signal discrimination threshold. The squeezing level is parameterised with the normalised variance, V_S, as defined in Sec. 4.2.1. The 'discriminating threshold' represents a number of standard deviations below the empty-cavity photon number. (a) Resonant and (b) detuned detection conditions are the same as Fig. 4.2.

maximum. For resonant detection the increase can be up to SNR ~ 140.

4.5 'Mode-matching': Atomic Beam Waist

We have discussed the strength of the dipole force in the axial direction, and the data presented in section 4.4.4 show how beneficial this force can be in improving the atom-field coupling, and detection quantum efficiency. The efficacy of this longitudinal force drops with the radial position of the atom, since the field and coupling strength diminishes as $\exp\left(r^{-2}\right)$. It is therefore important to ensure the atom laser profile is positioned carefully within the Gaussian distribution of the resonator mode, and is not too large for the probe beam waist. Although the physical mechanism if entirely different, one might consider this process as analogous to the mode-matching of a signal-beam and local-oscillator in photon quantum-optics: a necessary procedure for quality detection.

Figure 4.8 shows how the distribution of detection signals changes when the ratio of the atom laser beam width to the cavity mode width is varied. In our modelling, we fix the optical waist, and vary the atom laser beam profile, since this process rather than the inverse is experimentally easier to perform. For fixed discriminating thresholds (established for both resonant and detuned detection in the previous section), the proportion of real atom transit signals that pass the threshold, and are measured, changes as the overlap between the atom laser beam and cavity mode is varied. In figures 4.8(a) and (b) the atom laser waist is $w_a = 10\mu$m, half the cavity waist size, and the quantum efficiency is

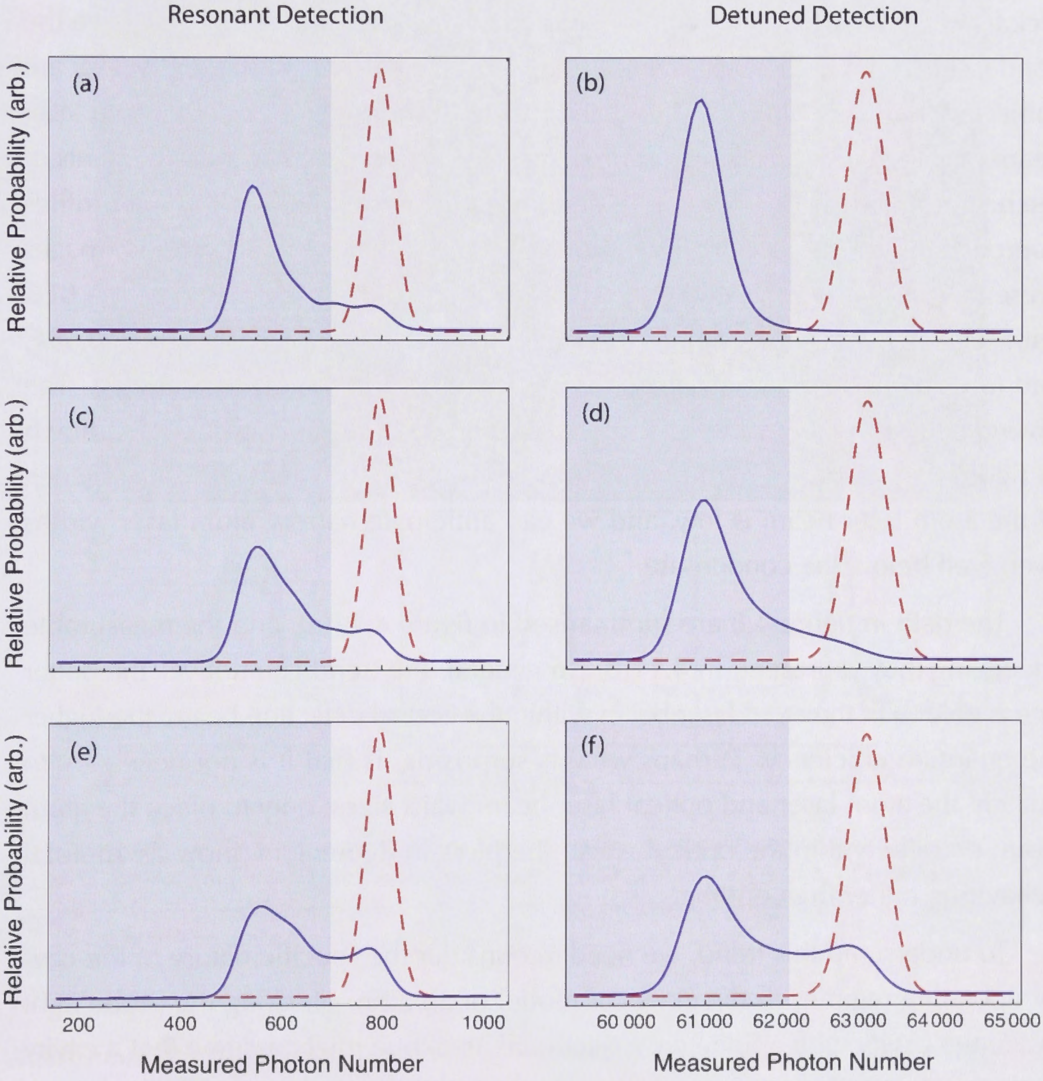

Figure 4.8: Photon distributions for an empty cavity (dashed traces), and a cavity with atom transits through all possible positions (solid traces), for cavity mode waist $w_0 = 20\mu$m and atom laser profile waist of w_a (a)-(b)10μm, (c)-(d)20μm and (e)-(f)30μm.

approximately 85% for resonant detection and $> 99\%$ for detuned detection. In figures 4.8(c) and (d) the atom laser waist is $w_a = 20\mu$m, and in (e) and (f)30μm. The respective quantum efficiencies are 81% (88%) and 73% (71%) for resonant (detuned) detection.

Real atom lasers are produced with either a radio frequency (rf) or a coherent multiphoton (Raman) transition to out-couple from a BEC, and the beam profiles can differ markedly depending on the method used as well as the nature of the atomic species [78, 115]. Using a Raman transition, atoms receive a momentum kick from the absorption and emission of photons. This causes them to leave the condensate more quickly than when using an rf transition. Consequently they are subjected to mean-field repulsion of the BEC for a shorter time, and the atom laser beam profiles show substantial improvements. In reference [78] measurements of the beam quality using Raman outcoupling show atom laser beams with profiles approaching the Heisenberg limit. Figure 4.9 is a sequence of absorption images presented in that work. Atom lasers are outcoupled from the centre of the BEC with (a) negligible momentum kick - rf outcoupling - and (b) a kick of $0.5\hbar k$, and (c) $1.9\hbar k$, using Raman beams at angles of 30° and 140° respectively. The divergence of the atom laser beams for these outcoupling conditions is shown in figure 4.10. For the high-momentum transfer Raman beams, the divergence of the atom laser beam is low, and we can anticipate narrow atom laser widths even well below the condensate.

The data in figure 4.8 are summarised in figure 4.11(a), and the measurable squeezing they represent, in 4.11(b). In general, the trend is intuitive: the better one is able to fit the atom laser beam within the optical detection beam, the higher the quantum efficiency. Perhaps what is surprising, is that it is not necessary to 'match' the atom laser and optical laser beam waist sizes, only to place the atom beam entirely within the optical waist; the plots in figure 4.11 show asymptotal behaviour, rather than optima.

To understand this trend, we need to consider the specific nature of the cavity operating regime: In the classical model of an atom blocking the probe light inside the cavity with a finite cross-sectional area, one might assume that a cavity waist any larger than the atomic beam waist will lead to excess photon noise. Yet this is not the case. It is important to remember that the atomic-beam waist, and the atomic cross-sectional area are two separate things. The beam waist

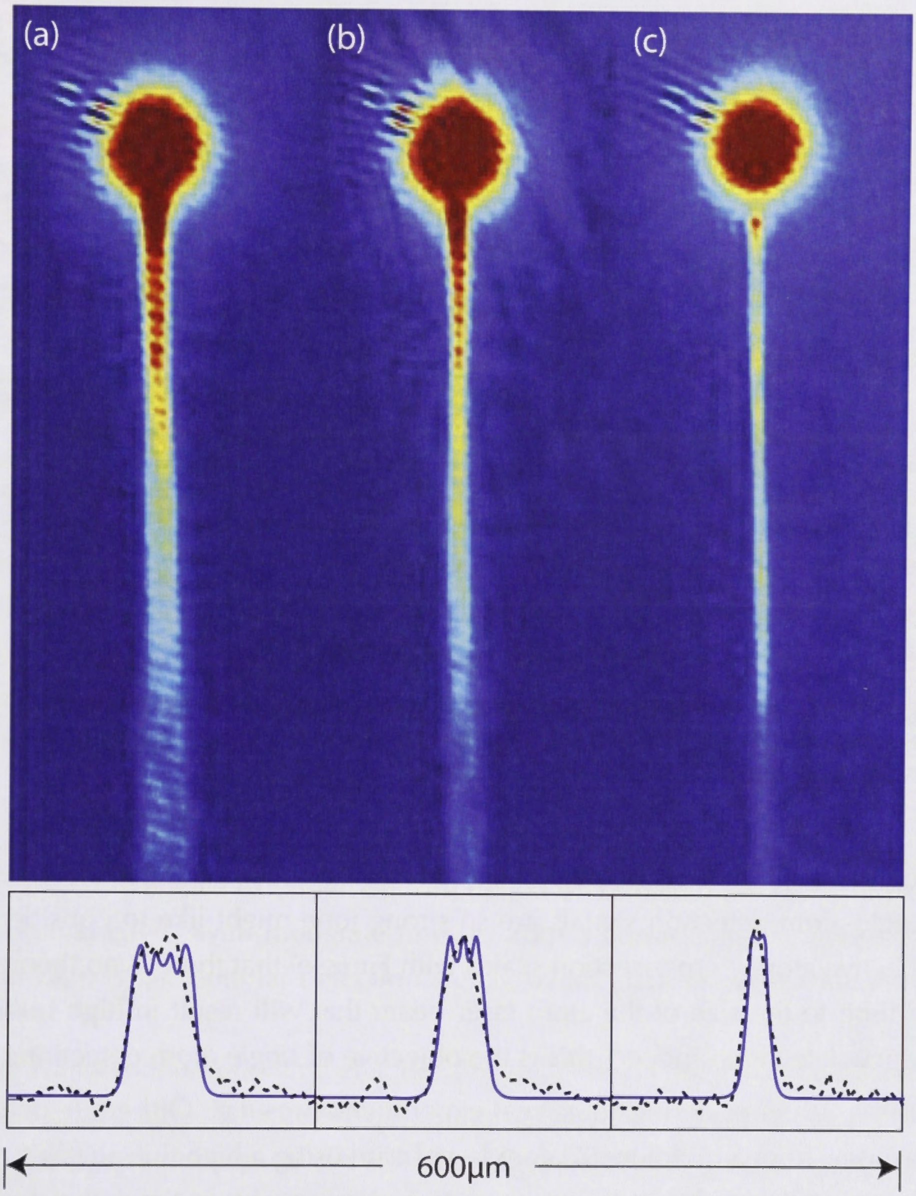

Figure 4.9: Atom laser beam profiles. The beams are produced with (a) rf outcoupling, and Raman outcoupling with photon kicks of (b)$0.5\hbar k$ and (c) $1.9\hbar k$. Experimental (dashed) and theoretical (solid) beam profiles 500μm below the condensate are shown in the lower sequence.

determines the probability distribution for atomic entrance positions, while the cross-sectional area is a classical measure of the 'size' of a single atom. In the operating regimes that we consider in this work, that classical model simply does not apply for cavities above a certain finesse; the reader is referred to our dis-

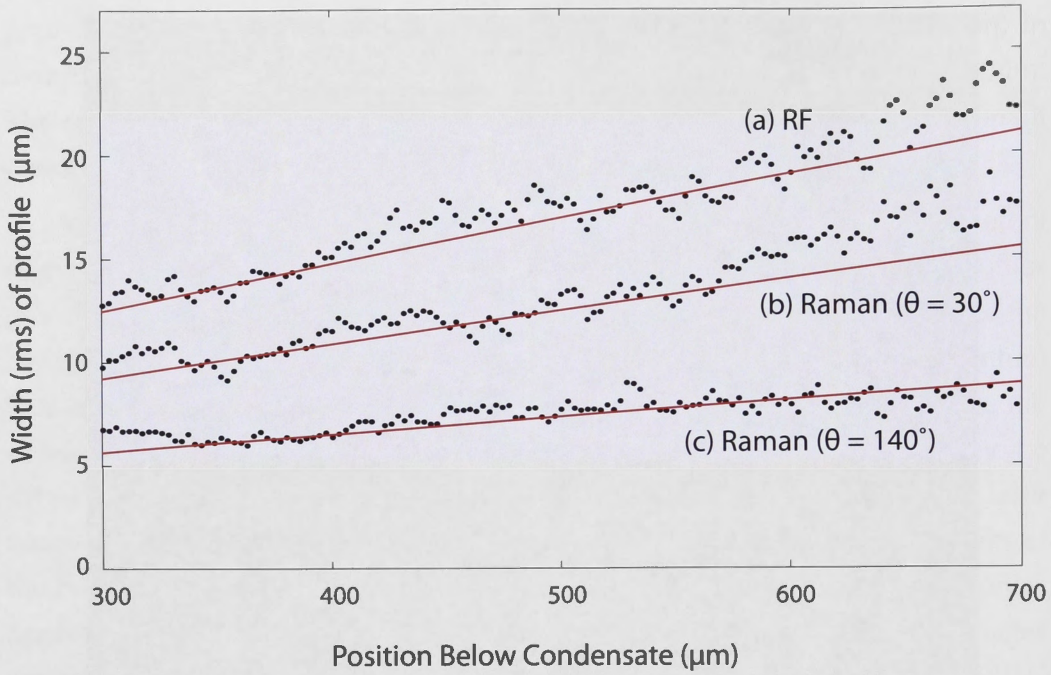

Figure 4.10: Atom laser beam profiles for (a) rf outcoupling, and (b)-(c) Raman cout-coupling with photon kicks of $0.5\hbar k$ and $1.9\hbar k$ corresponding to Raman laser beams at angles of 30° and 140° respectively.

cussion of the limitations of the classical model, in section 3.3.1. For our work, the single-atom detection signals are so strong (one might like to consider that the effective atomic cross-section scales with Finesse) that there is no theoretical lower limit to the size of the atom laser beam that will result in high quantum efficiency detection - indeed, this is the objective of *single*-atom detection.

It is worth considering some real experimental results. Öttl *et al.* detected single atoms from a rubidium 87 atom laser beam using a high finesse cavity, with the detection threshold set to a drop in transmission of four times the standard deviation of the empty-cavity photon shot noise [104]. For the detection power used, this discriminating value gave a false atom-detection rate of less than $0.5s^{-1}$. The probe beam used was red-detuned by three atomic linewidths, in an attempt to channel atoms into the antinodes of the resonator mode. Even so, the overall detection efficiency of atoms extracted from a BEC was measured to be roughly 25%. This was recognised as due almost entirely to poor overlap of the atom laser beam profile with the cavity mode. The 1/e-diameters of the atom laser beam were determined to be 80μm and 110μm (the beam cross-section was elongated,

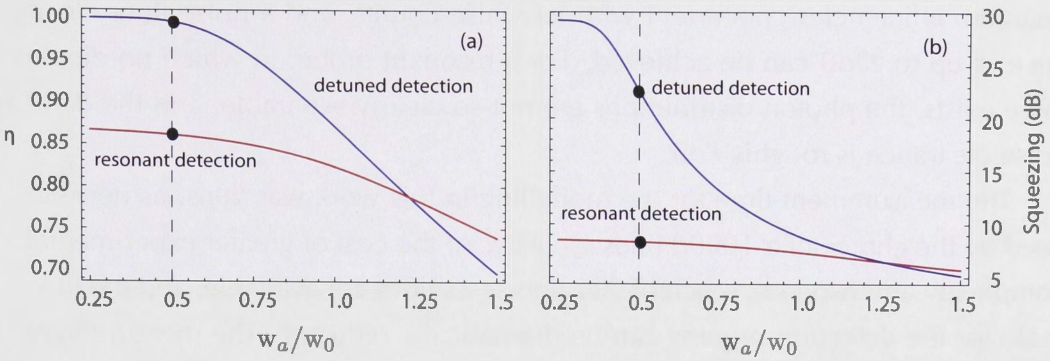

Figure 4.11: Variation in (a) quantum efficiency and (b) the *measured* squeezing for an infinitely squeezed source, as a function of cavity and optical mode over-lap. The discriminator threshold is -3.9σ (-3.4σ) of the empty cavity photon distribution for detuned (resonant) detection. The optical mode waist, w_0, is 20μm. The dashed lines correspond to the parameters used in figure 4.6: an atomic beam waist of 10μm

not circular), while the cavity mode waist was $w_0 = 25.5\mu$m. In this case many atoms enter the mode far off-axis. The radial dipole force is not enough to deflect transits into high-coupling (axial) regions, so the effective coupling and signal strength remain negligible.

4.6 Conclusions

In this chapter, we have extended our discussion of a single-atom detector based on an optical cavity with moderate finesse, from a consideration of the signal-to-noise ratio of an optimal detection signal, to an analysis of less ideal atom transits.

The ability to measure number squeezing depends on the detection efficiency and false count rate. In a cavity-based atom-detection system, these are both influenced by the position of a discriminating threshold that determines which values of photon counts are considered to correspond to atom transits and which to the empty cavity power level. We have analysed hypothetical measurements on an atomic beam using resonant and detuned detection. The optimal positions for the discriminator were determined numerically by finding the highest values for the squeezing parameter, in these two regimes.

We found in the case of detuned detection, atoms experience a strong electric-dipole force that channels them efficiently into regions of strong coupling, leading to distinctly separated photon distributions for empty-cavity and detection events. The separation allows us to define a threshold value that produces high detection quantum efficiencies concurrent with low false-counts, and a noise-floor clearance of up to 23dB can be achieved. For a resonant probe, in which no dipole force exists, the photon distributions are not so clearly separable, and the dark-noise clearance is roughly 8dB.

The measurement time for the modelling in this work was $20\mu s$, as necessitated by the choice of a 10000 finesse cavity. At the cost of greater experimental complexity and expense, much higher finesse cavities are available, and the time scale for the detection process can be dramatically reduced. The measurement time limits the allowable atom flux, and for $\tau = 20\mu s$ we accept only 5000 atoms per second, since higher fluxes saturate the detector. Nevertheless, if a squeezed source can be used, cavity detection is capable of signal-to-noise ratios comparable fluxes an order of magnitude great, and has the advantage of operating in real-time with a continuous rather than pulsed source.

Part II

Experimental Practicalities and Results

CHAPTER

FIVE

EXPERIMENTAL APPARATUS AND CONTROL

One of the goals for our preliminary modelling work was to deduce whether a cavity of only moderate finesse could be used successfully for high quantum efficiency single-atom detection. The presumption was that such a cavity would be both cheaper to build and easier to work with than the ultra-high-finesse resonators of cavity QED experiments. While this is indeed the case, the complexity and expense of any cold-atom experiment should not be underestimated. Vacuum requirements make for intriguing architecture - with often restrictive optical access - and polarisation, power and frequency of light generally need to be carefully controlled. This chapter outlines the practicality of the design and operation of the experiment, with a particular focus on frequency control of key components.

- We begin in **sections 5.1** and **5.2** with a description of the configuration of the optical components and the locking procedure we use for stabilising the detection cavity.

- An overview of the detection cavity is given in **section 5.3**.

- **Sections 5.4** and **5.5** detail the data acquisition process, including a description of the photon detection method and the digital demodulation procedure, as well as a preliminary power calibration routine.

5.1 Optical Layout

Ultimately the detection cavity must have its frequency (cavity length) stabilised to the rubidium 87 transition with which we are concerned, but the process is not as straight forward as locking the cavity directly to the spectroscopy-stabilised 780nm probe laser. There are two reasons for this: firstly, the ideal amount of power in the probe laser is on the order of a few to hundreds of picoWatts, depending on the detection regime that is chosen, as discussed in chapter 3. While it *is* possible to lock to very low light levels [102], it is by no means an easy feat, and much more stable locks are achieved when more power is used, generating better signal-to-noise on the error signal. Secondly, in order to have the two detunings (cavity-probe $\Delta_c = \omega_0 - \omega_c$ and atom-probe $\Delta_a = \omega_0 - \omega_a$) variable and independent, the cavity cannot be locked directly to the probe laser.

Some cavity experiments are performed without active locking, when the passive stability of the system is sufficient and frequency drifts occur much slower than the relevant time scales of the experiment [138, 24, 72]. For the system that we are investigating, atom transits of the cavity mode are predicted to take no longer than $20\mu s$. We expect the passive frequency stability of our detection cavity and probe laser to be maintained on this time-scale. However, for a versatile system to measure an atom flux on time scales anywhere from milliseconds to hours or days, active locking is desirable.

Generally the solution to the problem of detection cavity locking is to use a second laser with a substantially different frequency as a 'stabilisation' laser [104, 135, 23, 70, 100]. Provided it is far-detuned from the atomic resonance, this laser can have more power in it than the probe laser - in order to achieve a good cavity lock - but will not interfere with atom transits. This second laser also needs to be frequency-stabilised.

The stabilisation laser can either be locked to an 'absolute' frequency reference, such as a different atomic transition (for example using caesium spectroscopy), or have its frequency stability transferred from the probe laser. We use a locking chain that employs a so-called 'transfer cavity' to link the frequencies of the two lasers. We subsequently make use of a fibre electro-optic modulator (EOM) to allow a sufficient frequency tuning range of the stabilisation laser in order to achieve co-resonance in both cavities. The locking chain is discussed in the next section.

A simplified schematic diagram of the layout of the optical components of the experiment (as opposed to the components comprising the atomic source) is shown in figure 5.1 and a photograph of the real optics table in figure 5.2.

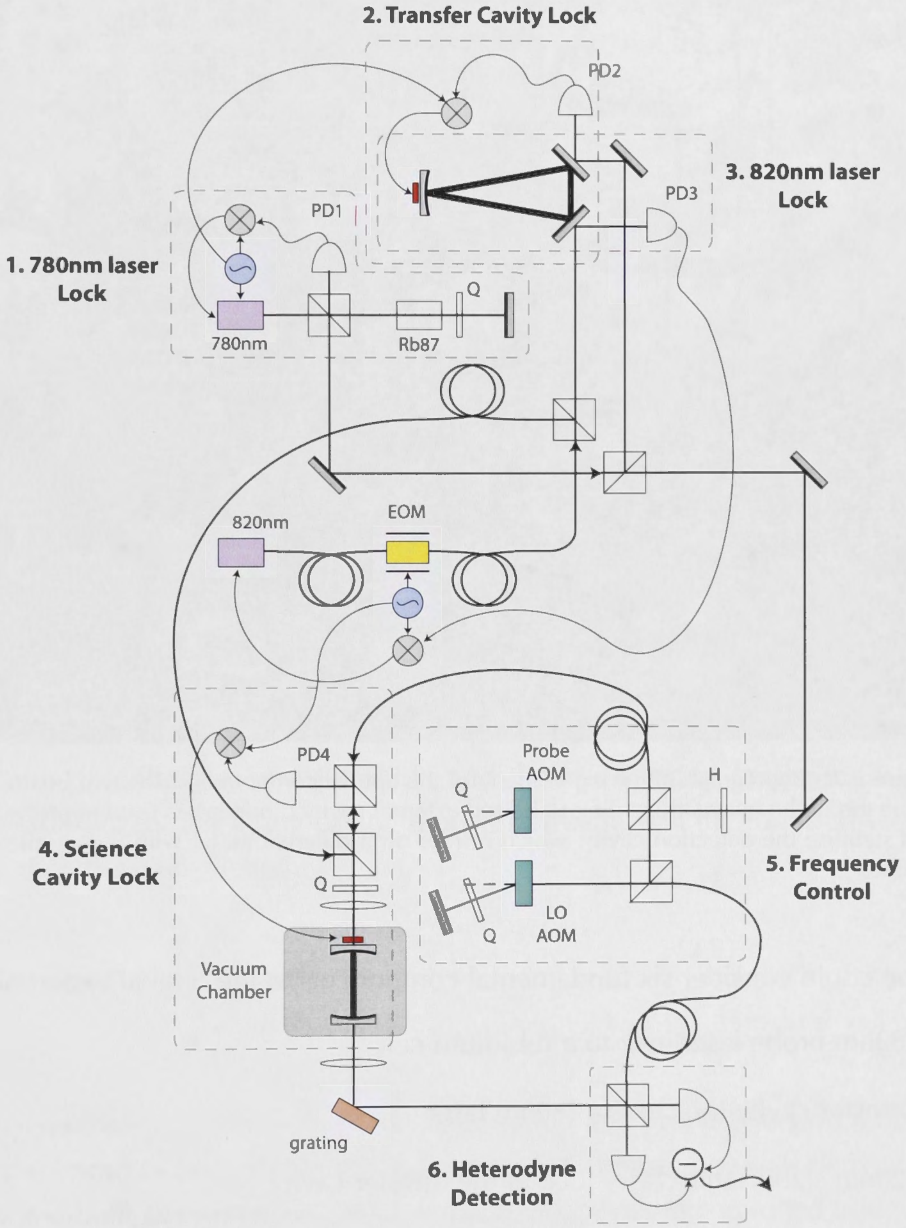

Figure 5.1: Simplified layout of the optical experimental set-up. Important components are the Accousto-Optic Modulators (AOMs) and the Electro-Optic Modulator (EOM). Half and quarter wave-plates are labelled H and Q, and photodiodes, PD. Other elements are named. Two modulations are used to provide the error signal for four locks.

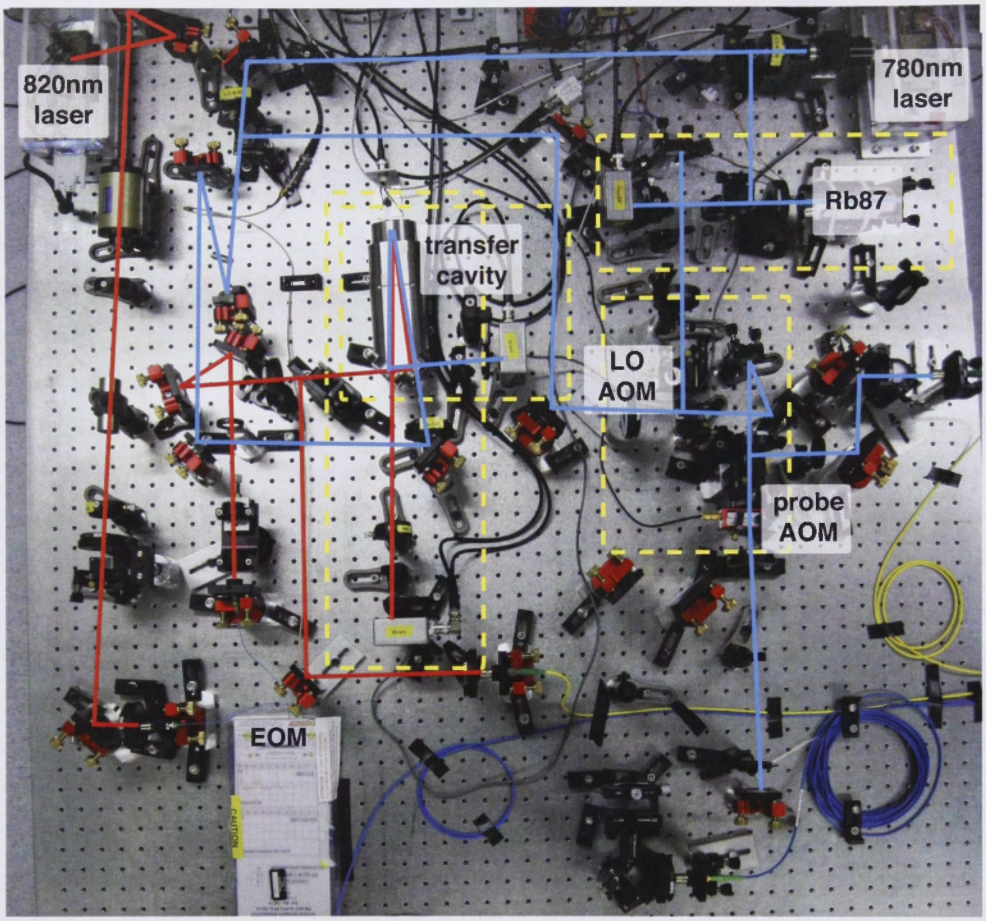

Figure 5.2: Photograph of the experiment for the optical components. The two boxes at the top of the image are grating stabilised external cavity diode lasers used to probe and stabilise the detection cavity, which resides on a different table, with the atomic source.

One could consider six fundamental components to the optical experiment:

1. 780nm probe laser lock to a rubidium cell
2. Transfer cavity lock to the 780nm laser
3. 820nm stabilisation laser lock to the transfer cavity
4. Science cavity lock to the 820nm stabilisation laser
5. Frequency (and power) control of the probe and local oscillator beams
6. Heterodyne detection of the probe beam

Function generators provide modulation frequencies at approximately 9MHz and 23MHz for our locking loops. Each signal is then split with analogue voltage dividers, and used to create frequency modulation on the two lasers beams *via* current modulation for the 780nm beam and electro-optic modulation on the 820nm light. The remaining modulation signals from the output of the two initial splitters are then split again and passed to analogue mixers - one for each lock - to be multiplied with the ac component of the relevant photodetector current. Thus the four unique error signals used in the locking of two cavities and two lasers are generated with two distinct frequency sources. The particular frequencies for these locking modulations are not important, provided they are independent, and do not share strong higher-order harmonic frequencies.

Our transfer cavity is a three-mirror 'ring cavity' with a path length of approximately 40cm. The input and output mirrors are planar dielectric mirrors, custom coated for a finesse of 1000 for s-polarisation and about 100 for p-polarisation (*ATFilms*). The third cavity mirror is a high finesse, ultra-low loss, spherical mirror (*Newport 'SuperMirror' 10CV00SR.40F*), with a reflectivity of about 99.9%, and radius of curvature of 1m. The mirrors are mounted in an invar spacer, which has a low coefficient of thermal expansion (approximately 1.2ppm/K) to provide low temperature sensitivity of the cavity length. The finesse of a ring cavity is related to its linewidth and free spectral range in the same way as for a Fabry-Pérot resonator described by equation (2.9) and the free spectral range is still given by equation (2.8). For a ring-cavity, L now represents half the round-trip length, rather than the cavity length:

$$\nu_{FSR} = \frac{c}{2L} \tag{2.8}$$

$$\mathscr{F} = \frac{\nu_{FSR}}{\Delta\nu} \tag{2.9}$$

A selection of resonances of the stabilisation and probe lasers on reflection from the transfer cavity are shown in figure 5.3. Our laser power is derived from two home-built external cavity diode lasers (ECDL) that are controlled using commercial *MOGLabs* controllers [3]. These controllers include an internal locking servo that stabilises the laser frequency with feedback to the diode current and voltage across the piezoelectric transducer on which the grating is mounted. Our 780nm probe laser uses a 90mW diode (*Roithner ADL-78901TX*), and the stabili-

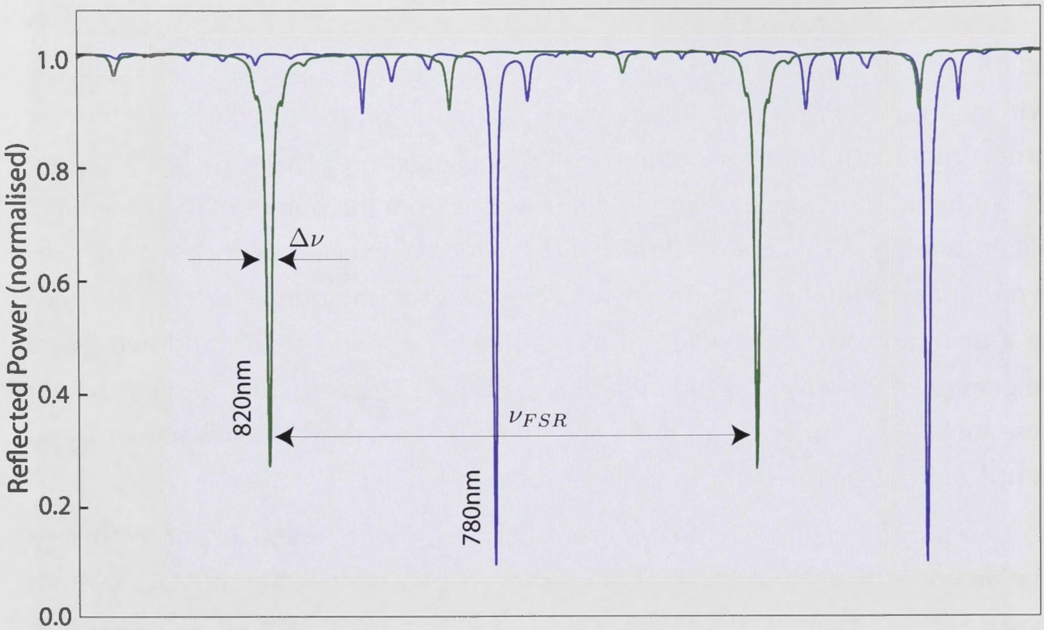

Figure 5.3: Transfer cavity resonances. Sidebands produced with the fibre EOM on the stabilisation laser (not switched on in this scan) are used to measure the free spectral range, and calibrate the other cavity parameters.

sation laser is currently running with an anti-reflection coated 100mW diode (*Eagle Yard EYP-RWE-0840-06010-1500-SOT02-0000*). We have found the diodes for the stabilisation wavelength more problematic and more variable than the 780nm model, with some diodes operating better at 840nm and others closer to 820nm. Nevertheless, for our purposes the specific wavelength of the stabilisation laser is not important provided it is sufficiently far-detuned from the atomic resonance.

5.2 Locking Chain

The ultimate reference frequency for the experiment is the $|F=2\rangle \rightarrow |F'=3\rangle$ hyperfine transition in rubidium 87. In figure 5.4 the saturated absorption spectrum for the 5S1/2 to P3/2 transition in rubidium 87 is shown. The 780nm probe laser is current-modulated and locked to the $|F=2\rangle \rightarrow |F'=1\rangle$, $|F=2\rangle \rightarrow |F'=3\rangle$ hyperfine cross-over line (the 1,3 cross-over) in a rubidium 87 vapour cell saturation absorption spectroscopy set-up. The probe laser frequency is later up-shifted by $(212+\Delta_a)$MHz with an acousto-optic modulator to the required frequency for

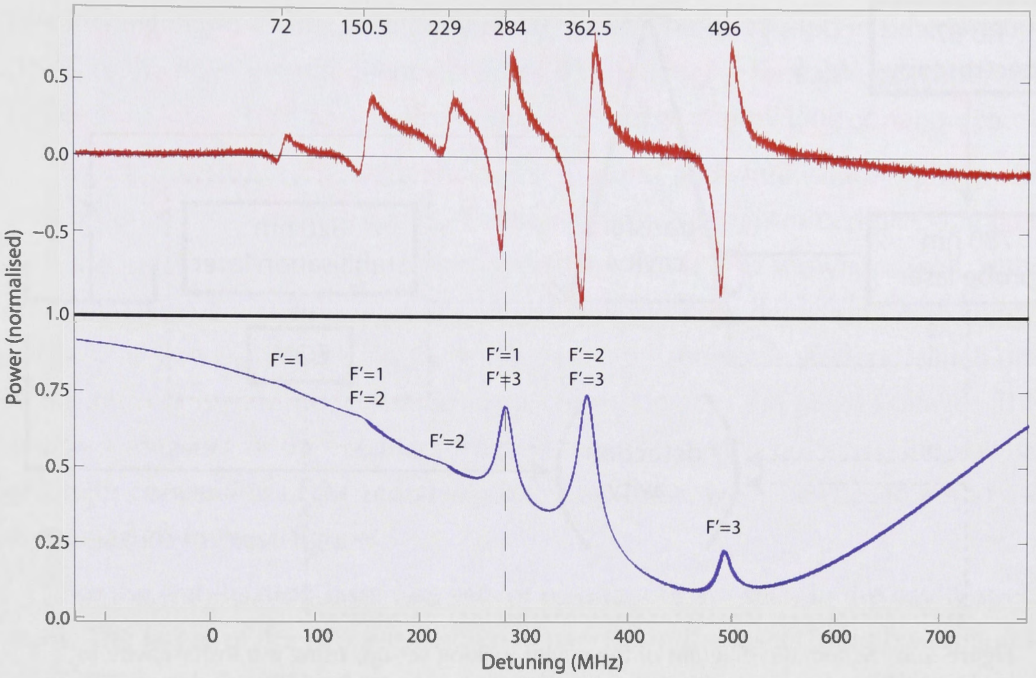

Figure 5.4: Saturated absorption spectrum for the 5S1/2 to P3/2 transition in rubidium 87(below) and the error signal used to lock the probe laser (above). The abscissa measures the frequency above the $|F' = 0\rangle$ state, with the frequency of each hyperfine resonance and 'cross-over' labelled on the upper axis. (The reader may wish to compare this spectrum to the energy level structure shown in figure 2.1). The laser is locked to the 1,3 cross-over indicated with the dashed line.

resonant or detuned detection. $\Delta_a = \omega_0 - \omega_a$ is the detuning of the laser detection frequency from atomic resonance.

Figure 5.5 shows a schematic of the chain of locks. The resonance of the stabilised probe is observed on reflection from the transfer cavity which is then locked to the laser. The detection cavity length is then tuned to transmit the probe laser, and the stabilisation frequency is tuned so that it, too, is resonant in the detection cavity.

Since both lasers need to be resonant in the detection cavity and the transfer cavity simultaneously, we must be able to tune at least one of them independently in *both* cavities. To achieve this required tuning flexibility, we add strong high frequency sidebands to the stabilisation laser using a fibre-coupled electro-optic modulator (EOM) (*ultra low-loss Lithium Niobate phase modulator: EOSpace PM-0K5-10-PFA-PFA-852*). These sidebands are typically at radio frequencies (rf) -

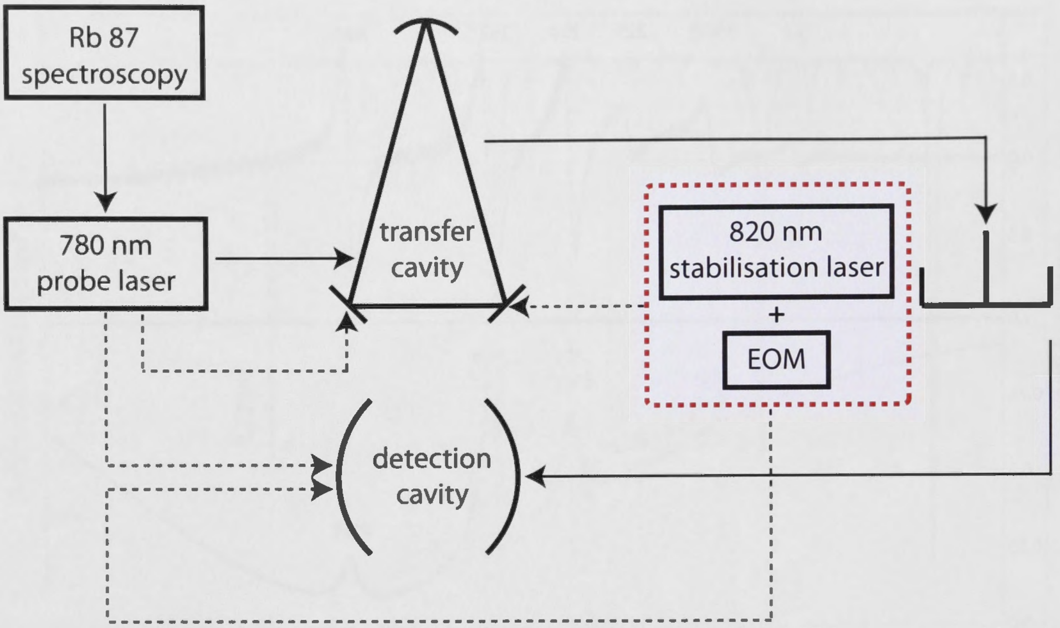

Figure 5.5: Schematic diagram of the cavity locking set-up, using a transfer cavity to bridge the large frequency difference between the probe and stabilisation lasers. The solid arrows represent the stabilisation processes, with the arrow heads pointing towards the component that is to be locked, while the dashed arrows indicate the transmission of both lasers in both cavities.

well outside the cavity linewidth - and the ability to tune the frequency is important. We use the laser current control to shift carrier and sidebands together until the carrier is resonant with the detection cavity. A small modulation at much lower frequency is also added to the EOM control voltage in order to generate the required error signals.

The detection cavity is locked to the carrier of the stabilisation laser light. We then tune the relative frequency between the stabilisation sidebands and carrier using the EOM controller so that one of the sideband frequencies is resonant in the transfer cavity (remember, the transfer cavity is already locked to the probe laser) and lock the stabilisation laser to the transfer cavity using this frequency. We need the EOM because we have no other way of tuning the stabilisation laser to the transfer cavity once the detection cavity is locked. The transfer cavity free spectral range is approximately 800MHz, and the function generator (*Hameg HM8134-31.2 GHz RF-Synthesizer*) with which we drive the EOM allows us first order sidebands from zero to 1.224GHz, giving more than sufficient tuning range.

This locking chain avoids additional phase-locked lasers as used in other set-ups [104], or the need for a frequency comb [105] or a highly tuneable but expensive Ti:Sapphire laser [100] to stabilise frequencies separated by tens of nanometers.

Figure 5.6 shows the resonance of the probe and stabilisation light on reflection from the detection cavity. The signal from the transmitted probe, mixed with the local oscillator at the heterodyne detectors is also shown, as well as the error signal on the stabilisation laser. For these plots the detection cavity length is changed slowly by scanning the voltage on a piezoelectric stack on which one of the mirrors is mounted. The abscissa corresponds to the piezo voltage. This is also a measure of the resonant frequency of the cavity, but since the voltage to length conversion of the piezo is not strictly linear, we have chosen not to use that measure in these figures.

For the stabilisation laser two sets of resonances are seen in the cavity spectrum. The larger of the two sets (shown expanded in the insets in both subfigures) is the TEM_{00} mode and the set at lower voltage is a higher-order mode due to misalignment of the laser with the cavity mirrors. With the term 'set', I refer to the collection of features comprised of the carrier frequency as well as first order and weaker second order sidebands of each mode. Note that the strong rf sidebands on the stabilisation laser are those introduced with the fibre EOM as discussed previously. These sidebands are well outside the cavity linewidth and are not the modulation used to generate the error signal. That modulation is much weaker and at a frequency of roughly 20MHz: within the cavity linewidth. The modulation is carried on all components of the stabilisation light, so that each of the EOM sidebands as well as the carrier frequency generate a unique error signal.

The traces in figure 5.6(a) show the carrier of the stabilisation laser and the (weaker) probe light are resonant at different cavity lengths. After tuning the stabilisation laser current, the two are co-resonant and cannot be resolved on the cavity spectrum in (b).

Once the co-resonance condition is achieved, the cavity scan is stopped and its frequency (length) is locked. Figure 5.7 shows the corresponding power and error signals and the beatnote signal of the probe and local oscillator. When performing the atom-detection experiment, the power in the probe laser is too small to be seen on the reflected signal, and too weak to produce visible heterodyne fringes. However, it is necessary to use enough power to observe these manifes-

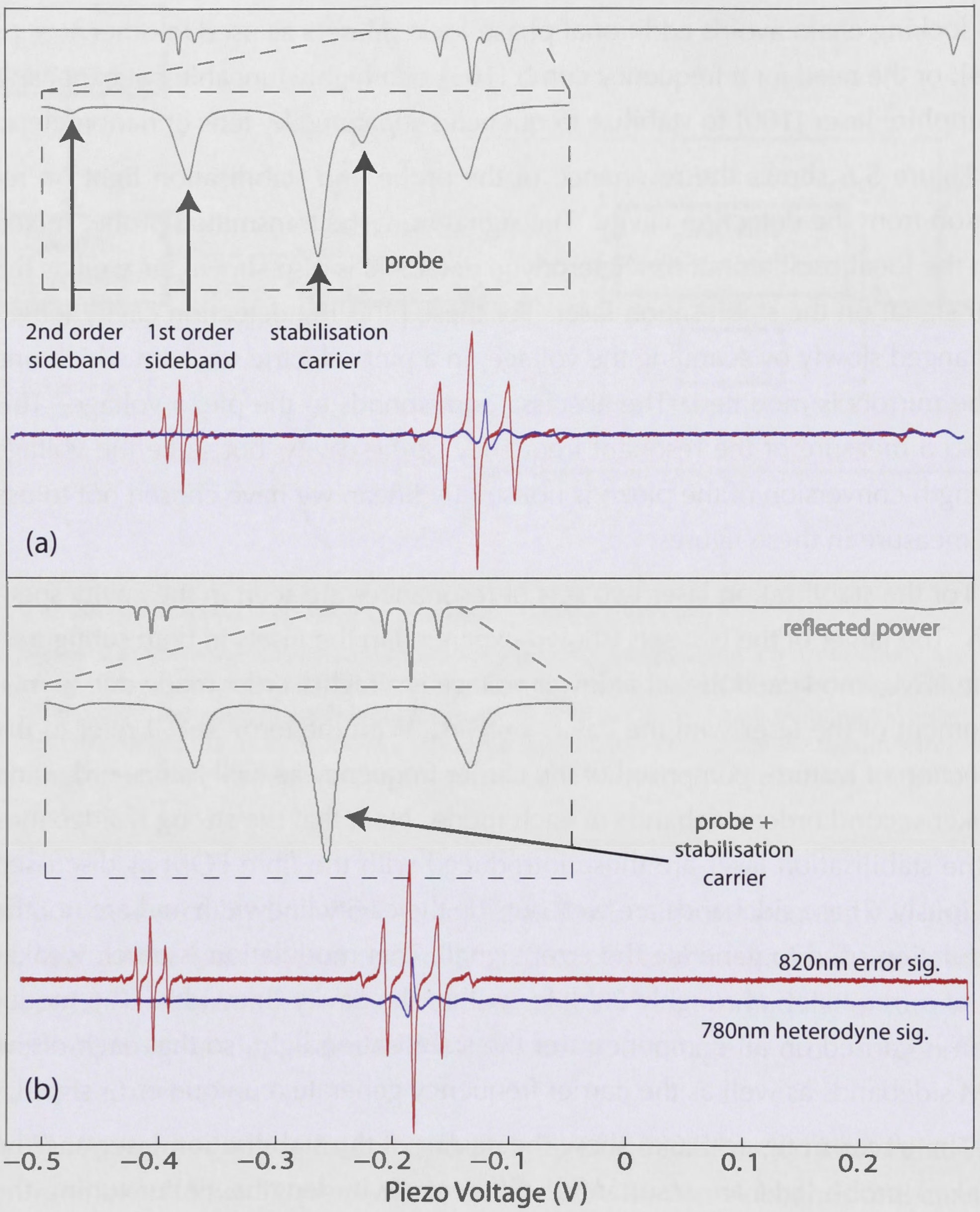

Figure 5.6: Resonances in the detection cavity. In (a) and (b) the upper traces are the reflected signals containing both probe and stabilisation laser power. The red trace is the error signal of the stabilisation laser obtained by demodulating the reflected signal at the modulation frequency carried on this laser. The blue trace is not an error signal, but a few fringes from the heterodyne signal of the transmitted probe laser beating with the local oscillator. In (a) the two lasers are resonant at different cavity lengths, while in (b) they are co-resonant: the reflected carriers are unresolved, and the transmitted probe signal peak overlaps with the centre of the stabilisation error signal.

tations of the probe while searching for the co-resonance condition. The probe power is reduced to the detection level after the locking chain is completed.

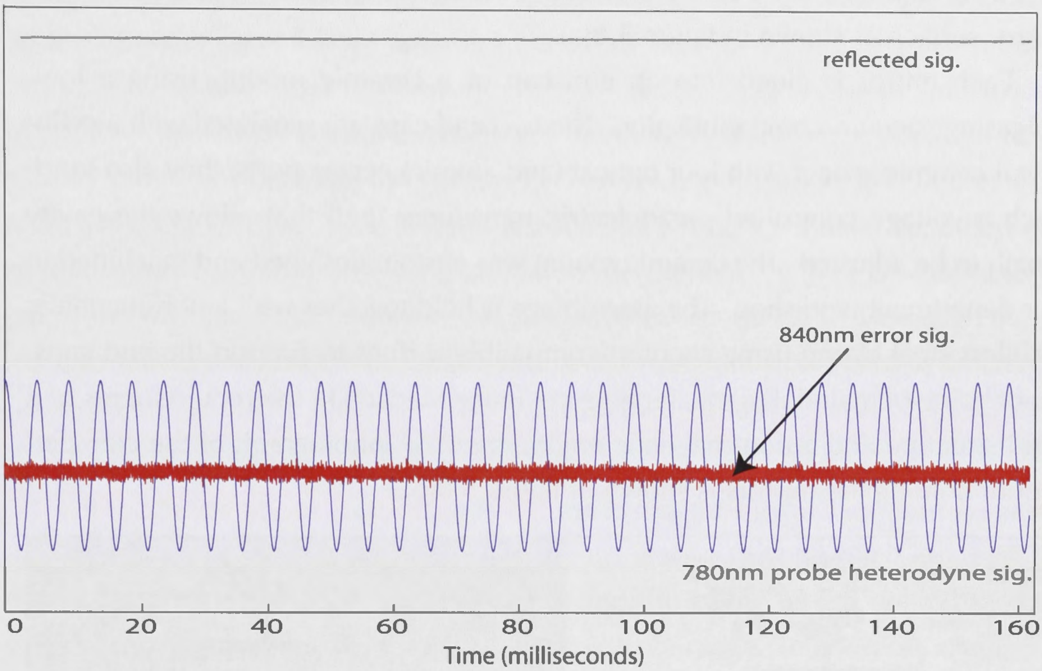

Figure 5.7: The locked cavity signals: the upper trace and error signal are stable in time - since the cavity is held on resonance - with a steady power reflected (and transmitted). The fringes in the heterodyne signal are due to the transmitted probe beam mixed with the local oscillator. For these fringes to be visible the probe power is well beyond that which is used in the detection experiment.

5.3 The Detection Cavity

5.3.1 Apparatus and Assembly

The input and output mirrors of our detection cavity have different transmission coefficients giving an 'under-coupled' Fabry-Pérot cavity with the output mirror transmission three times higher than the input. This reduces the loss of intra-cavity photons *via* decay through the input mirror. Mirror substrates and coatings were custom designed and machined at *ATFlims* [2]. The input mirror transmission was designed with a coefficient of transmission $T \sim 0.0105\%$ and the output $T \sim 0.0314\%$ at 780nm, and similar values for the far-detuned stabilisation wavelength. Appendix B shows one of the preliminary modelled transmittance curves for the lower finesse (output) mirror substrate. The mirrors have a radius of curvature of 50cm that gives a mode waist of 40μm when they are separated by 200μm, following equation (2.10). They are 5mm in diameter, 'coned' to 2mm at the mirror surface as shown in figure 5.8(a).

Each mirror is glued into an end cap of a ceramic mount, using a low-outgasing vacuum-compatible glue. The two end caps are separated with a cylindrical ceramic spacer with four optical (and atomic) access ports; they also sandwich a voltage controlled piezoelectric transducer (pzt) that allows the cavity length to be adjusted. The ceramic mount was custom designed and machined in our department workshop. The assemblage is held together with a non-magnetic stainless steel clamp using vacuum-compatible o-rings to support the end caps. Our choice of material (a machinable ceramic: Macar®) fit the requirements of a rigid structure and a non-magnetic environment. A photograph of the clamped mount holding the mirrors is shown in figure 5.8(b).

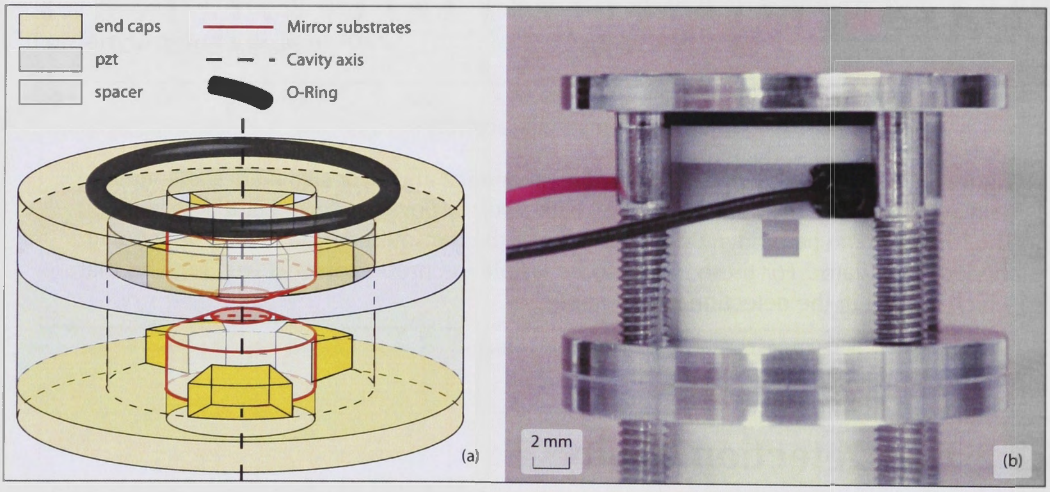

Figure 5.8: (a) A schematic of cavity mirror substrates with their mount and pzt and (b) a photograph of the mount and clamp. Four windows in the mount [one shown in (b)] provide atomic and optical access orthogonal to the cavity axis.

5.3.2 Cavity Parameters

From equations (2.8) and (2.9), we can deduce the length and finesse of the detection cavity if we measure the linewidth and free spectral range, by calibrating the frequency axis of the cavity spectrum. The easiest way to do this is to put known 'frequency markers' on the cavity spectrum using the sidebands from the

EOM on the stabilisation light and higher order spatial modes resulting from sub-optimal mode-matching. Examples of these markers are shown in the spectra of figure 5.9. First-order sidebands with a frequency of 1.2GHz are used to deduce (a) the linewidth and (b) the apparent frequency separation of the TEM_{00} mode from higher spatial order resonances. In figure 5.9(b) the third-order sidebands of adjacent transverse modes overlap. We therefore determine the apparent frequency difference between the carriers of the TEM_{00} mode and the TEM_{10} mode to be $6 \times 1.2 = 7.2$GHz. Note that this is not a *real* frequency difference; different spatial orders have the same longitudinal mode number - which is what determines the wavelength or frequency - as discussed in section 2.2.2. However, they are resonant at different cavity lengths and are consequently observed at different positions on the cavity spectrum. These mis-alignement modes are subsequently used in (c) to measure the FSR of the cavity.

Although the above procedure is the most straight forward method for frequency measurements, it is not particularly accurate. The approach assumes a linear conversion between the pzt voltage and the cavity length, which is not strictly true, particularly at the extent of the voltage range. In addition, changes in cavity length due to thermal effects in the mirror substrates when the cavity is filled with high intensity resonant light have been observed in high finesse cavities [117]. However, for a finesse of only 10^4 we do not expect the intra-cavity power to be so high as to induce an observable effect - even with our use of higher probe powers. In any event, such an effect is a minor perturbation when compared to the uncertainty introduced with the non-lineararity of the pzt. Scanning at low voltages, where the voltage-to-length conversion on the pzt is most linear, as well as taking several spectral measurements and averaging, minimises the measurement uncertainty.

A similar process using frequency markers is employed to determine the parameters of our transfer cavity. This cavity is so much longer than the detection cavity and consequently the entire free spectral range can be scanned *directly* with the sidebands from the EOM on the stabilisation laser. The first-order sidebands from adjacent modes are co-resonant in the transfer cavity when they are 394.5MHz from the 820nm carrier frequency. The free spectral range of the cavity is therefore twice this frequency: $2 \times 394.5 = 789$MHz.

For our measured detection cavity parameters, we can deduce the various

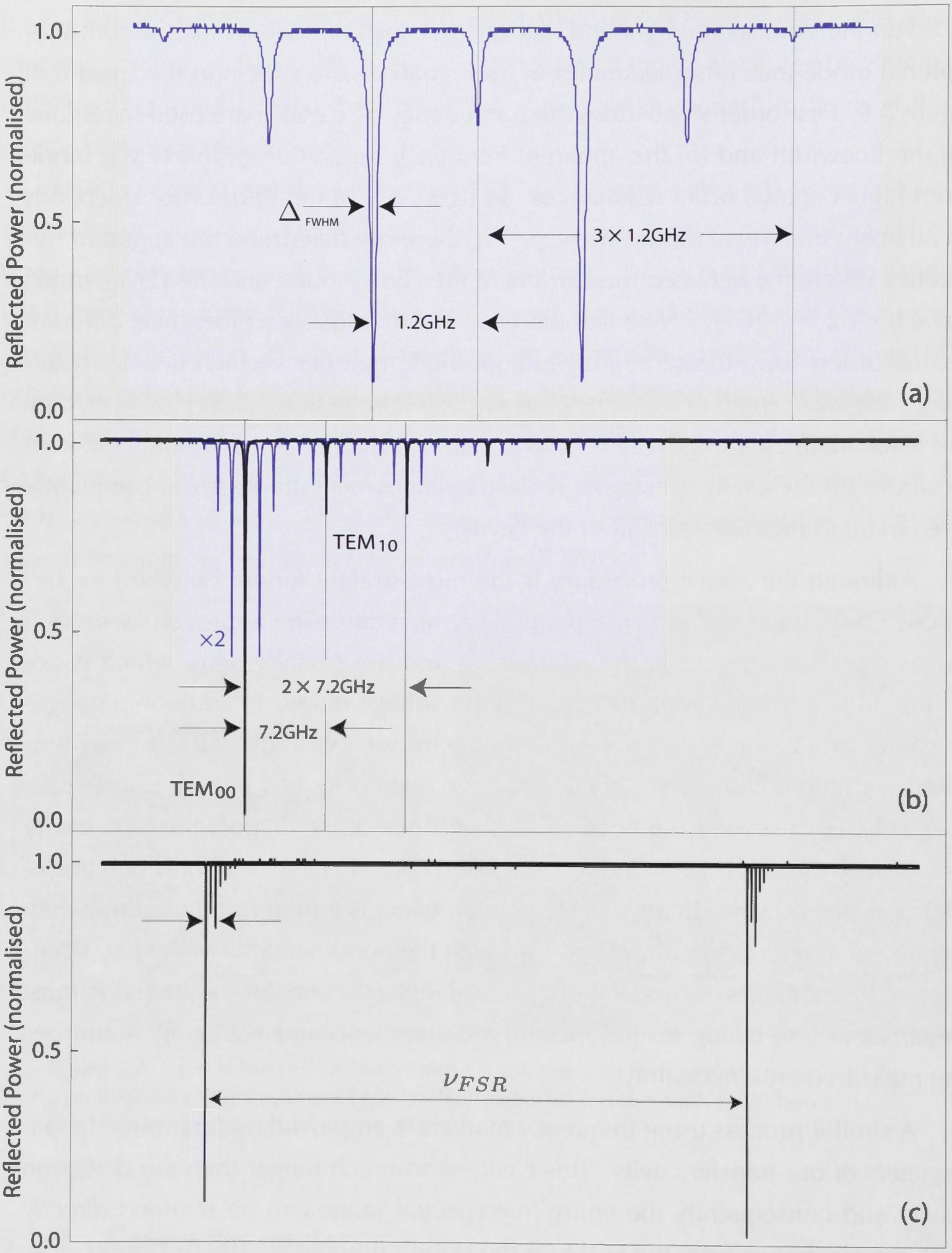

Figure 5.9: Detection cavity spectra with 'frequency markers' derived from the EOM sidebands. First-order sidebands with a frequency of 1.2GHz are used to deduce (a) a linewidth of 86MHz (b) the apparent frequency separation of the TEM_{00} mode from the next higher spatial order resonance, 7200MHz, and subsequently (c) the FSR of the cavity: about 820GHz.

atom-cavity coupling variables, using the relations given in chapter 3. Our detection cavity does not operate in the strong coupling regime; that was not the intention of this experiement. The parameters for both cavities, and the decay and coupling rates are summarised in table 5.1:

	Detection Cavity	**Transfer Cavity (p-polarisation)**
linewidth (MHz)	86	8
FSR	820GHz	789MHz
cavity length	180μm	38cm
Finesse	9500	100
mirror curvature	50cm	1m
waist size (μm)	41	300
g_0 (MHz)	$9.45 \times 2\pi$	
κ (MHz)	$83.3 \times 2\pi$	
Γ (MHz)	$6 \times 2\pi$	

Table 5.1: Cavity parameters as detailed in text

5.4 Cavity Control

The length of our detection cavity is controlled by applying a voltage to a piezoelectric ring actuator (*Piezomechanik HPSt 150/15-8/3*) that sits between the cavity mirrors (see figure 5.8). These actuators are vacuum compatible (so can withstand the 'baking' of our vacuum chamber at several hundred degrees) and have a ring geometry that is necessary for optical access along the cavity axis.

The actuator is operated between -30 and 150V and the data sheets for the device suggest a maximum stroke of $3 - 4\mu$m. When we scan the full voltage range of the actuator, we measure just over seven free spectral ranges on the detection cavity using the 780nm probe laser. This tells us the maximum stroke is indeed of the suggested approximate length: $7 \times \lambda/2 = 7 \times$ 780nm$/2 \sim 3\mu$m.

We control the piezo voltage source and monitor the cavity response using a field-programmable gate array (FPGA) card (*NI PXI-7852R*). A real-time code written in LabVIEW® acts as an interface between the user and the FPGA. Signals are sent from a low speed (750kHz) analogue output channel on the FPGA to the cavity pzt *via* a high-voltage amplifier, and the dc component of the photodiode that monitors the cavity response is sent to a low speed analogue input. The output signal can be operated in 'scan' or 'lock' mode. In scan mode, the interface allows the user to adjust the amplitude and speed of a triangular voltage scan. In lock mode the scan is stopped, and the gain and polarity of the offset and the proportional (P) and integral (I) feedback can be adjusted.

Appendix C provides detail of the front-face of the LabVIEW user interface.

5.5 Data Acquisition

5.5.1 Laser Frequency Separation

All our locking and preliminary monitoring of the detection cavity resonance conditions are observed on the beams *reflected* from the cavity input mirror (PD4 in figure 5). The output mirror is then used as the port at which to collect probe photons for signal analysis. That analysis requires us to separate the co-propagating stabilisation and probe beams before detection. This can be achieved with (1) a diffraction grating or (2) optical frequency filters:

(1) Diffraction gratings obey the 'grating equation' (5.1), which governs the angular positions of intensity maxima for a given wavelength, λ

$$m\lambda = d(\sin\alpha + \sin\beta). \tag{5.1}$$

Here, α is the incident angle, measured from the grating normal, β is the refracted angle, m is the diffraction 'order', and d is the groove spacing - or the inverse of the groove frequency G. From this relation we can derive the angular dispersion of co-propogating polychromatic light, that is, the change in diffracted angle per unit wavelength, for constant α:

$$D = \frac{d\beta}{d\lambda} = \frac{mG}{\cos\beta} \tag{5.2}$$

In our apparatus, we use a planar holographic grating with $G = 2000$ grooves/mm (Newport Catalog $\#33056FL02 - 059H$) and an incident angle of $\alpha \sim 40°$. This gives us a dispersion of about one fifth of a degree between the first order diffraction of the 780nm probe light and the 820nm stabilisation light: more that sufficient to spatially separate the two beams after a small propagation distance.

The *efficiency* of a diffraction grating - how much power from the incident beam is distributed into a given spectral order - depends on many parameters: polarisation and power in the incident beam, angles of incidence and diffraction as well as the grating blaze angle and material all play a part. A complete treatment of the grating efficiency has not been deployed here, since it is of minor relevance for this work. Instead, we found the optimal incident angle experimentally to give the best (spatially undistorted) beam parameters and distributing roughly 70% of the probe power in the first diffracted order for $s-$polarisation.

(2) A different option for separating the two frequencies is to use a filter to block the stabilisation laser, and pass only probe light to the detection system. The probe and stabilisation lasers have well-separated frequencies that do not demand an exceptionally 'sharp edged' filter, however, the power in the stabilisation laser is significantly stronger than that of the probe beam: milliWatts in comparison to picoWatts. Consequently the filter requirements become rather strict, since *extra* photons contribute to a noisy signal to the same degree as *lost* photons. Thus the rejection of 820nm must be extremely good, while the transmittance of 780nm is also required to be high. Compared to the 70% efficiency of our diffraction grating, we infer that an equivalent system using filters would require that the number of stabilisation photons reaching the detection system be no more than 30% of the number of probe photons: For the given power ratio, this requires an optical filtering system that passes only 3×10^{-10} of the stabilisation power.

The above discussion is concerned with the physical separation of the co-propagating frequencies. For photon detection that relies on direct photon counting, consideration of lost and residual photons and the power ratios in the two beams is very important. Amplitude (and subsequent power) measurements, using heterodyne detection, offer substantial additional effective filtering (to be discussed in the following section), and exploiting this property means that purification of the probe prior to detection is not so critical.

5.5.2 Heterodyne Photon Detection

Procedure

In chapter 3, we considered the use of two types of detection for the probe laser: (i) an avalanche photodiode (APD) - also referred to as a single photon counting module (SPCM) - and (ii) heterodyne detection. The advantage of an APD is that it is a single device that is reasonably straight-forward to set up. On the other hand, it is power-limited. That is to say that such a device saturates so only very low probe powers are acceptable. While it is true that the power used in the single atom detection process is generally low, we found that in the case of *detuned* detection the probe power necessary to obtain a good signal-to-noise ratio exceeds the saturation limit of a typical APD (approximately 20 photons/μs). Heterodyne detection is consequently much more versatile and, in addition, has a higher efficiency (the quantum efficiency of an APD is generally limited to less than 50% at 780nm). In chapter 3, section 3.4.2, we presented a schematic diagram and mathematical argument for the demodulation of a heterodyne detection set-up without the need to phase lock the LO:

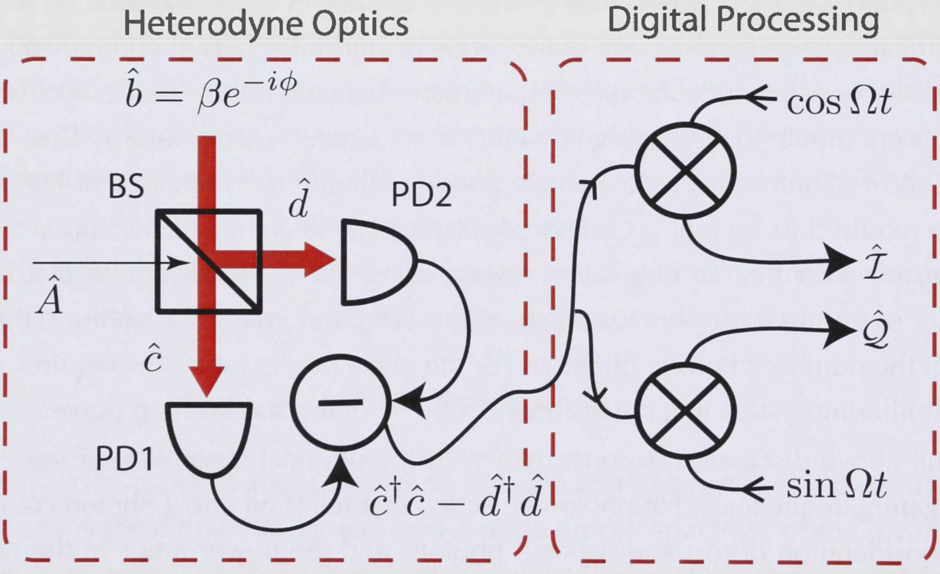

Figure 5.10: Schematic diagram of two stages of the data acquisition process.

The weak field to be measured interferes on a balanced beamsplitter with a strong local oscillator (LO) with a well defined frequency offset. We use the same ECDL to provide both the LO and probe light in our set-up (see **Frequency Control** section of figure 5.1). After a small amount is picked off for spectroscopy and transfer cavity locking, the laser light is passed through two 'cascaded' acousto-optic modulators (AOMs), each running in a double-pass configuration. The power ratio between the output of these AOMs can be varied with a half-wave plate that proceeds them and more delicately with the independent radio frequency driving powers controlling each.

We drive the AOMs using signals derived from a single clock frequency controlled *via* a field-programmable gate array (FPGA) card (*NI PXI-7852R*) so that they are frequency-locked, and we run the local oscillator AOM about 12MHz below the probe AOM frequency. This means that in the double-pass configuration we have a 24MHz frequency offset between the LO and probe and this is the frequency at which we demodulate the heterodyne signal.

The LO and transmitted probe beam interfere on a 50:50 beamsplitter and the 24MHz beat frequency between them is measured at detectors on each beamsplitter port. The measurements on the detectors are subtracted on a power splitter with a π phase offset, and yield a signal that is proportional to the probe beam amplitude ready for digital processing (figure 5.10).

Efficiency and Filtering

In contrast to an APD, photodiodes used in heterodyne detectors can have efficiencies around 95%. As well as the relatively small losses in these detectors, the heterodyne efficiency is dictated by the spatial mode-matching of the probe beam and local oscillator on the 50:50 beamsplitter that proceeds the detectors, and the matching of the polarisations of the two beams. It is related to the fringe visibility by

$$\eta_{het} = \mathcal{V}^2$$

where the visibility $\mathcal{V}$ is defined as

$$\mathcal{V} = \frac{P_{\text{max}} - P_{\text{min}}}{P_{\text{max}} + P_{\text{min}}}.$$

P_{max} and P_{min} are the maximum and minimum power in the fringes, corresponding to constructive and destructive interference.

In our set-up, we measured a fringe visibility with a maximum value of $\mathcal{V} = 0.98$, suggesting a heterodyne efficiency of 96%, however the visibility was not constant over extended observation periods. We surmise that the fluctuations in our heterodyne detection efficiency are one of our principle noise sources.

Further to the high efficiency that it offers, another advantage of heterodyne detection is the effective frequency filtering it provides. Since the frequency offset between the LO and the 820nm stabilisation laser is *not* 24MHz as it is between the LO and the probe laser, any residual stabilisation light should be rejected in the heterodyne demodulation. Thus the rejection criterion for 820nm light is not, in fact, as important as the passing of 780nm light at the grating or filtering stage discussed in section 5.5.1. Our photodetectors are optimised for low power, so we need to block a sufficient amount of the stabilisation laser so as not to saturate the detectors, but a well optimised heterodyne system can itself supply significant common mode rejection so that residual 820nm photons do not interfere with the signal. We measured up to 40dB of attenuation at the modulation frequency; an effective filtering that suppresses any residual stabilisation light power by a factor of 10000. We conclude that frequency filtering combined with heterodyne detection, may in fact have been a better choice than a diffraction grating for probe and stabilisation light separation.

5.5.3 Digital Demodulation

The experimental realisation of the demodulation method was carried out digitally in a program written in LabVIEW 2010® (32 bit). The program was derived from the digital locking code developed in reference [133], and appendix C includes an illustration of the LabVIEW® block diagram of the code showing the components of the processing. The subtracted analogue signal from the two output ports of our heterodyne beamsplitter is processed in a high speed analogue-digital converter (ADC) to produce a 16 bit signal that is sent to a digital input channel on the FPGA. The processing then involves mixing - or demodulating - at the appropriate offset frequency, and executing the subsequent mathematical operations.

The LabVIEW® code consists of two loops: (1) a high speed loop at 80 Mega-samples/second; (2) a low speed loop at 500 kilo-samples/second. The demodulation occurs in the high speed loop where the digitised modulated signal from the ADC is multiplied separately by sine and cosine functions each generated using a look-up table. These functions have the same frequency as the modulation that is derived internally on the PXI (*NI PXI-5404*). The data are then down-sampled in a two-stage Cascaded Integrator Comb (CIC) filter: a digital equivalent of an analogue low-pass filter [69].

Once filtered, the two sets of data - multiplied by the sine and cosine functions respectively - are squared and summed in the low speed loop, to produce a signal that can be monitored in real-time and recorded for subsequent analysis. After digital processing, the signal is proportional to the LO power level,

β^2, rather than the field amplitude, β that is initially measured in the heterodyne process:

$$\langle \hat{\mathscr{I}} \rangle^2 + \langle \hat{\mathscr{Q}} \rangle^2 = \beta^2 \langle \hat{A} \rangle \langle \hat{A}^\dagger \rangle.$$

5.5.4 Calibration

There are several arbitrary gain factors between the detection of photons at the heterodyne photodetectors and the digital signal displayed and recorded in our data collection program. To calibrate this signal, we measure the raw photocurrent - that is, the subtracted output of the heterodyne set-up prior to digital processing - on an electronic radio frequency spectrum analyser. We see a peak at the modulation frequency whose amplitude is proportional to the power in the probe. The reader is reminded from chapter 3 equation (3.5) that the photocurrent (I_{photo}) is proportional to the product of the detected probe and LO field amplitudes,

$$\begin{aligned} I_{\text{photo}} \propto & \quad \hat{c}^\dagger \hat{c} - \hat{d}^\dagger \hat{d} \\ = & \quad \beta(\hat{A}^\dagger e^{-i\phi} + \hat{A} e^{i\phi}). \end{aligned}$$

Since the probe field amplitude is equal to the square root of the optical power ($\hat{A} = \sqrt{P_{\text{probe}}}$), the photocurrent is proportional to the square root of the probe power (and indeed, also the square root of the LO power). The size of the beatnote measured on the spectrum analyser is proportional to the electrical power (P) generated by this current and since $P = I^2_{\text{photo}} R$ the signal is also proportional to the optical power of the probe:

$$P \propto P_{\text{probe}}. \tag{5.3}$$

By taking a series of measurements at different low but measurable probe powers, we map the amplitude shown on the spectrum analyser to the value measured with a power meter. It is necessary to keep to low optical powers when carrying out this calibration procedure so as not to saturate the operational-amplifiers in the heterodyne photodiodes (since the photodiode circuits are designed for high gain). Satisfying this requirement, the relationship between the measurements on the power meter and the spectrum analyser is linear, and we can extrapolate the correlation as a convenient way to measure the power in the probe beam when it

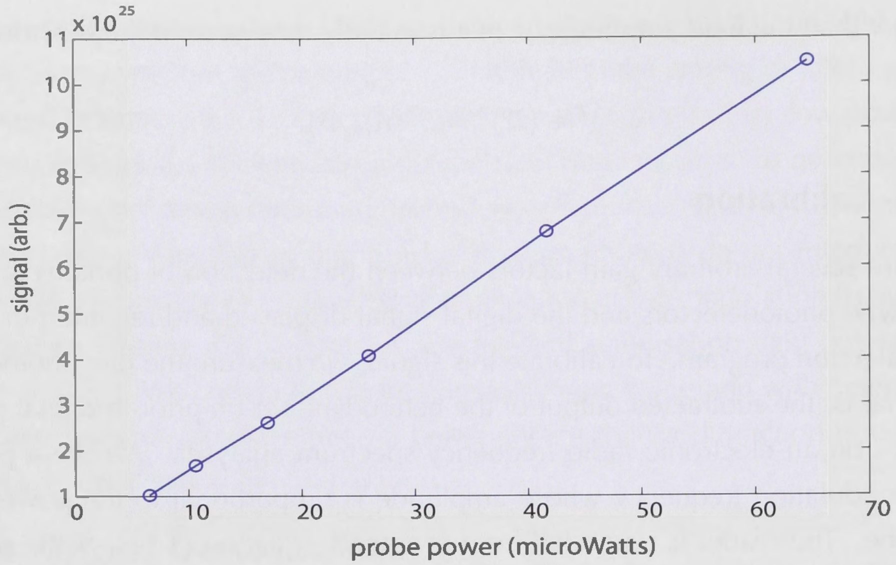

Figure 5.11: Calibration of data collection units. The probe power is varied over a low, but measurable range, and the arbitrary units on the data logging system are recorded.

is too small to observe on a power meter. We can similarly translate this mapping to the measurements shown in our data logging program, whose arbitrary units are also proportional to the optical power. Figure 5.11 shows the mapping of power measured with a power meter in front of the heterodyne detector, to the arbitrary units of the data logging program. The proportionality also applies to the power in the LO, and so the calibration of the signal units is not unique. The plot shown here is an example of the scaling measured, but the calibration needs to be repeated if ever the power in the local oscillator is changed.

5.5.5 Noise Sources

In our system, we were able to achieve good spatial mode-matching at the heterodyne detector and measured an optimal fringe visibility of 98% and noise suppression at 24MHz of 40dB. However, we found that the visibility and the attenuation it afforded drifted substantially over time due to fluctuations in probe and LO polarisation. Both these beams are fibre-coupled to the atom-detection table using polarisation-mantaining (PM), single mode fibres (*Lastek P3-780PM-FC-5*). While there will always remain a minimal degree of cross-talk between orthogonal polarisations in a PM fibre, aligning the axis - or 'key' - on the fibre-coupler to the polarisation axis of the input beam removes the polarisation rotation that enters when the axes are not coincident. Alignment of polarisation sensitive devices is such a common undertaking in optical experiments that substantial efforts have been devoted to mitigating the task [5]. Despite continuous efforts, however, we struggled to achieve acceptable alignment of some of our PM fibres and consequently suffered considerable power fluctuations in the polarisation-sensitive components following their outputs. It remains unclear why alignment of these fibres persisted as such a problem.

CHAPTER

SIX

ATOM TRANSITS

6.1 Introduction

In part I of this thesis, I presented results of the modelling work that was performed in order to determine the best experimental parameters for cavity *single* atom detection. Those parameters included the physical characteristics of the cavity as well as its operating regime with regards to probe power and probe and cavity frequencies. One important variable is the detection time - chosen to match the mode-transit time and therefore dependent on the speed that atoms have when transiting the cavity mode as well as the mode size. Another is the intra-cavity atom number that was implicitly taken to be one. In practice, these values depend on the geometric details of the experimental set-up. The atom number is found with the density of atoms at the cavity and the cavity volume and the velocity can vary greatly depending on the atomic source.

This chapter presents a discussion of the nature of atoms from our chosen source - a two-dimensional magneto-optical trap - as well as an analysis of the cavity detection signals of these atoms.

6.2 Sources of Atoms

Several different sources are available for supplying cold atoms to optical cavities. In their apparatus documented in reference [104], the cold-atom research group at ETH use condensed atoms from a BEC dropped into a high finesse cavity as an atom laser beam. Atoms were moving at about 1m/s as they transited the cavity mode. Other experiments observe single atoms from an un-condensed source - a three-dimensional (3D) MOT - either dropped from above the cavity [60, 138] or propelled upwards in an atomic fountain from below [102]. One of the appealing characteristics of launching atoms from below is that the velocity and density of atoms at the cavity can be fully controlled by adjusting the momentum transfer imparted on the atoms with appropriate laser 'push' beams. While it is equally feasible to apply push beams to downwards propagating atoms to influence their velocity (this technique is applied with the out-coupling beams of a Raman atom laser in reference [78] in order to deliver *faster* atoms that experience the condensate mean field for a shorter time), the control is not absolute, since *some* non-zero speed will be acquired in the distance that atoms fall to reach the cavity. In contrast, a fountain of upwards propagating atoms, derived from a source of stationary atoms can be designed to have particles with zero velocity in the detection region, if the apex of their trajectory is there.

Another option for a source of cold atoms is to use a *two*-dimensional (2D) MOT. This was the choice in the present experiment because it offered the most simple experimental configuration. To drive atoms from the trap to the detection region a push beam on the 2D MOT axis transfers upward momentum to the atoms along this unconfined dimension. An analysis of the velocity distribution of cold atoms from such a source is given in reference [129]. In that work, atoms as slow as 25m/s were produced with a high flux ($5-9\times10^8$atom/s) and narrow velocity distribution ($\sim$ 7.5m/s). The peak velocity can be varied considerably with the power in the push beam. Here, our intention was to achieve substantially lower velocities, on the order of 1m/s, resulting in considerable cavity transit times. The following section discusses the 2D MOT atom source and delivery system for our set-up.

6.2.1 Vacuum System Architecture

For our detection experiments, we mount the cavity in an ultra high vacuum (UHV) chamber and launch atoms into it from an atom source *below*. The source is a 2D MOT made in a quartz glass cell that forms a separate high vacuum (HV) compartment with optimal optical access.

The vacuum chamber configuration used is shown in figure 6.1(a), and a sketch of the set-up in 6.1(b). This architecture was used because we wanted to ensure the background pressure in the detection chamber is not so high as to

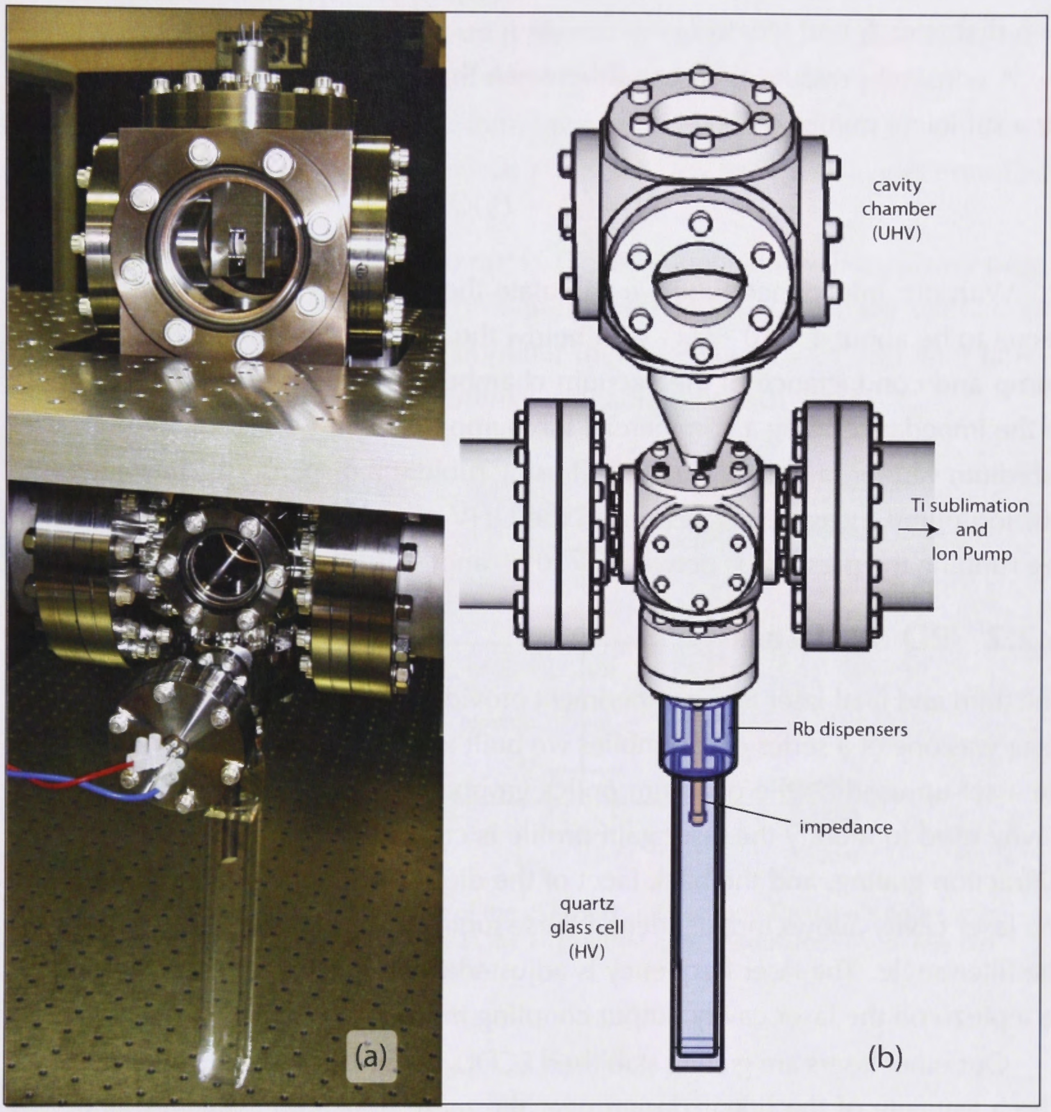

Figure 6.1: Vacuum chambers used for the atom detection experiment.

saturate the cavity detection signal, while we require a reasonable pressure to form the 2D MOT. The vacua are separated by an 'impedance': a 10mm long tube with a diameter of 0.7mm that links the two chambers. The 'conductance' of the impedance is measured in $litres/sec$ and in the molecular flow regime (appropriate for the pressures with which we are concerned) it is given by [1]

$$C = 12D^3(\frac{1}{L}) \tag{6.1}$$

for a diameter D and length L.

A constant pressure differential between the two is held by the impedance for a sufficient pumping speed, Q:

$$Q = (P_1 - P_2)C. \tag{6.2}$$

With our impedance tube we calculate the conductance between the two vacua to be about $4 \times 10^{-5} l/s$ - well below the volume flow rate of the vacuum pump and conductance of the vacuum chambers. We pump on the UHV side of the impedance using a commercial ion pump (*Gamma Vacuum®*), and release rubidium vapour in the HV quartz cell using rubidium dispensers. The gauge on our ion pump measures a pressure in the UHV chamber. When the dispensers are running the pressure is between $\sim 10^{-10}$ and $\sim 10^{-9}$torr.

6.2.2 2D MOT Laser

The third and final laser in our experiment provides the light for our 2D MOT. This laser was one of a series of assemblies we built to test a new ECDL design, based on a set-up used by the quantum optics group in Hannover [53]. The external cavity used to modify the laser gain profile is created using a mirror rather than diffraction grating, and the back facet of the diode. An interference filter within the laser cavity allows independent, course tuning of the wavelength, by rotating the filter angle. The laser frequency is adjusted *via* current control and feedback to a piezo on the laser cavity output coupling mirror.

Our other lasers are grating stabilised ECDLs in the Littrow configuration [66]. The advantage of the linear design over the more typical Littrow and Littman-Metcalf configurations is that the laser beam is neither translated nor tilted with piezo movement. The interference filters, however, are expensive to source and very sensitive to angular placement.

The 2D MOT trapping laser is operated approximately 12MHz below the $|F = 2\rangle \rightarrow |F' = 3\rangle$ transition in the rubidium 87 D2 line. This is achieved by down-shifting part of the laser light using a double-pass AOM configuration within the locking loop; the down-shifted beam is stabilised directly to the 1,3 cross-over line in a Zeeman modulated saturation absorption lock, leaving the light that does not pass through the AOM close-to-resonant with the desired transition. The detuning of the trapping light can be adjusted by changing the AOM frequency. A schematic of the set-up is shown in figure 6.2, and the reader may also wish to refer to the saturated-absorption spectrum shown in figure 5.4.

Re-pump light is added to the trapping laser with the addition of very small sidebands from a fibre EOM, driven at about 6.8GHz with a voltage controlled oscillator (VCO).

We use a 90mW laser diode in our ECDL. After optical isolation, power pick-off for locking, and transmission through the fibre EOM, we are left with about 8mW of laser power. A tapered amplifier increases the power, and after fibre-coupling we have approximately 50mW available for the 2D MOT.

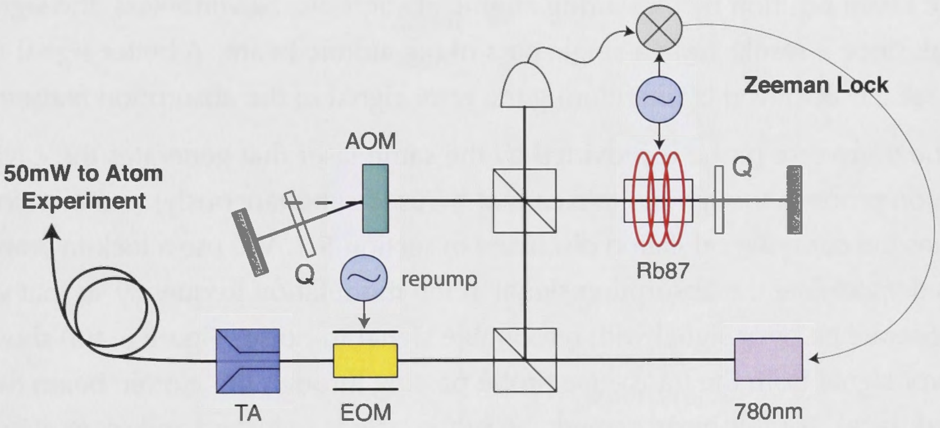

Figure 6.2: A simplified schematic of the 2D MOT light set-up. The labels codes are: AOM = Acousto-Optic Modulator, EOM = Electro-Optic Modulator, TA = Tapered Amplifier and Q = Quarter-wave plate.

6.3 Finding Atoms

6.3.1 Transverse Probe

The geometry of our apparatus was discussed in the previous section and figure 6.1 shows the arrangement of the 2D MOT chamber below the cavity chamber, connected *via* a narrow impedance. For alignment of the impedance and cavity we rely on careful machining and construction of the vacuum chambers and cavity mount. The 2D MOT position can be manipulated with the current in the MOT coils and the push beam is controlled with steering mirrors. Small windows in the cavity mount [see figure 5.8(b)] allowed us to observe the push beam scattering off the cavity mirrors as an indication that we had (at least roughly) aligned the beam with the detection region. At this stage we did not observe any atom signal in the cavity probe. We continued to initially check the coarse alignment *via* absorption in a 'transverse probe': a beam placed immediately below and orthogonal to the cavity axis (figure 6.3).

Because the transverse probe beam is not required to match the small cavity waist size (it is positioned directly *below* the cavity mount, rather than through the waist), it intersects a much larger cross-section of the atomic beam than does the longitudinal probe that populates the cavity mode. Consequently this beam is easier to align than the cavity probe and is used as an initial indicator of the atomic beam position by measuring atomic absorption. Nevertheless, the signal is weak since it results from a single pass of the atomic beam. A better signal-to-noise ratio is achieved by monitoring the error signal of the absorption feature.

The transverse probe is provided by the same laser that generates the cavity detection probe (although the two cannot be used simultaneously) and therefore contains the current modulation discussed in section 5.2. We use a lock-in amplifier to demodulate the absorption signal at the modulation frequency so that we can generate an error signal with reasonable signal-to-noise. Figure 6.4(a) shows the error signal from the transverse probe passing through the atomic beam (upper, red trace). For this measurement the probe laser is unlocked and scans slowly over the broad doppler feature containing the atomic transitions. The abscissa in figure 6.4 is measured in time but also represents the frequency of the laser. Part (b) and the lower (blue) trace in (a) show the reference absorption signal from the rubidium cell that is used to lock the 780nm laser. The two resonances in the vapour cell reference spectrum correspond to the 1,3 and 2,3 cross-over transitions within the 5S1/2 to P3/2 doppler-broadened transition line. Atoms travelling through the transverse probe beam only experience a single laser excitation - there is no 'pump' beam, only the probe - and so no 'cross-over' transitions are observed in their spectrum.

There is a substantial offset between the frequency of the $|F=2\rangle \rightarrow |F'=3\rangle$ transition observed in the rubidium vapour reference cell and that in the atomic beam below the cavity chamber. This could be caused by a number of conditions: one possibility is a Doppler shift due to angular discrepancies between the interrogating beams: in the saturated absorption configuration, the observed hyperfine transitions are for atoms with zero velocity in the direction of the probe

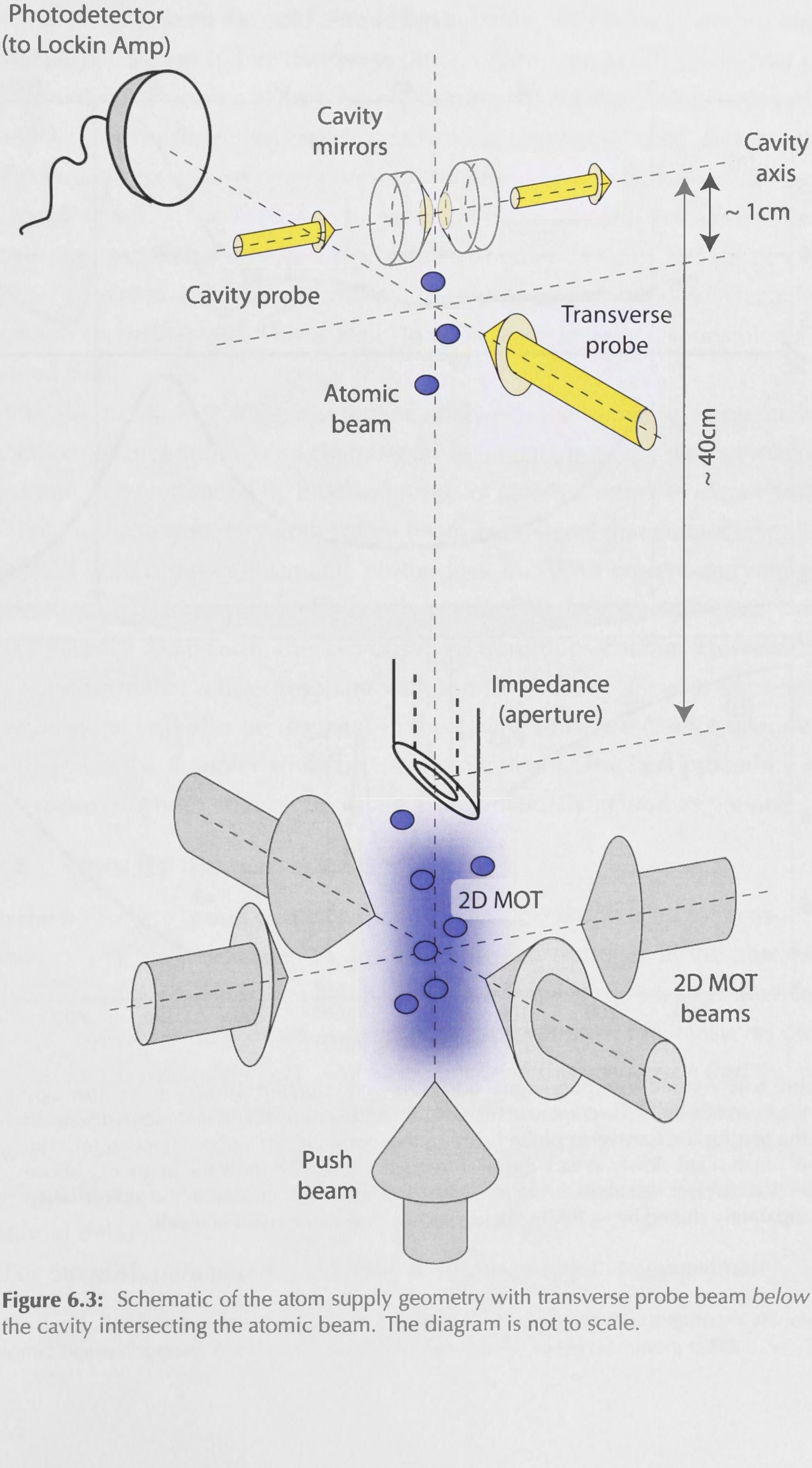

Figure 6.3: Schematic of the atom supply geometry with transverse probe beam *below* the cavity intersecting the atomic beam. The diagram is not to scale.

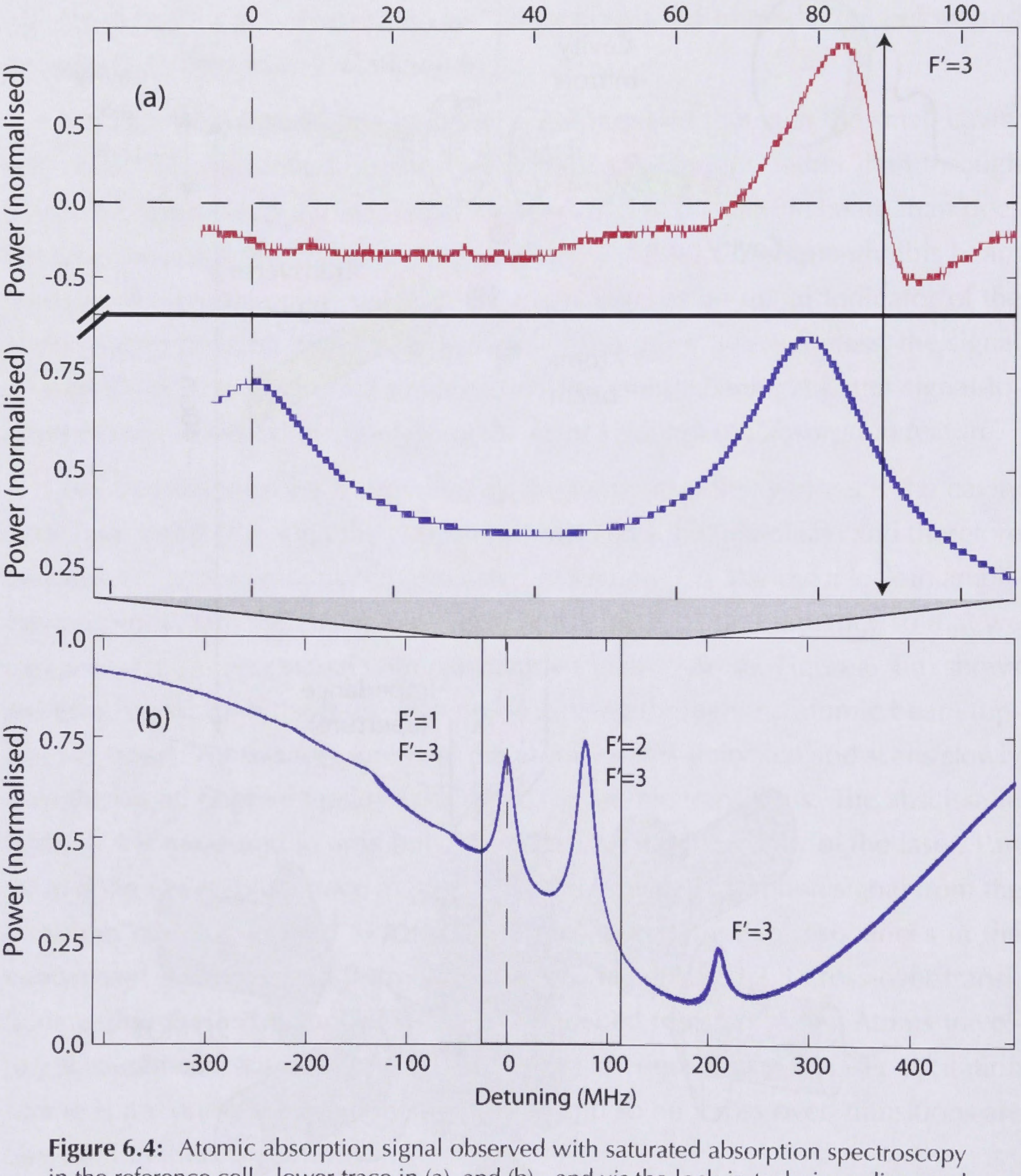

Figure 6.4: Atomic absorption signal observed with saturated absorption spectroscopy in the reference cell - lower trace in (a), and (b) - and *via* the lock-in technique discussed in the text for the transverse probe beam in the atomic beam - upper trace in (a). The laser piezo scans slowly to vary the laser frequency (the axes show the frequency above the 1,3 cross-over feature in the vapour cell). The $|F' = 3\rangle$ transition in the atomic beam is apparently shifted by $\sim$ 70MHz below its position in the reference cell.

laser. In the signal from the cold atomic beam below the cavity, atoms are ideally moving perpendicular to the 'transverse probe'. However, in this single-pass configuration, there is no mechanism for confirming the accuracy of this geometry[1]. In the instance that the orthogonality condition is not well satisfied, and that there is a reasonable transverse component to the atomic velocity, we would expect the Doppler shift on the hyperfine transition to be significant. For atoms moving approximately orthogonally to the probe, an angular offset of 10° (a generous estimate) results in a frequency shift of roughly of several hundred MegaHertz, dependent on their speed. This is likely to be at least partially responsible for the observed shift.

It is also possible that the discrepancy between the transition frequencies in the vapour cell and the vacuum chamber arises, in part, from the distinct magnetic environments experienced by the two groups of atoms. Further evidence for this is in the unusual asymmetry in the atom beam error signal that cannot be entirely eliminated with phase-adjustments on the lock-in. With current-carrying coils around the rubidium vapour cell we can manipulate the magnetic environment of the reference atoms until the two observed transitions concur. However, this does not ensure that a laser resonant with the $|F=2\rangle \rightarrow |F'=3\rangle$ transition at the vapour cell will also be resonant in the cavity, since we cannot deduce the importance of the Doppler effect on the atomic beam. The best procedure is to try to ensure that both environments are as magnetically neutral as possible.

6.3.2 Velocity measurements

With the transverse probe on-resonance, it is re-locked and used to measure the velocity of our atomic beam. Figure 6.5 shows an example of the absorption signal we see for a pulsed push beam. The trace acquisition is triggered with the switching 'on' of the push beam and shows the absorption in the transverse probe, averaged for 20 measurements. The delay between the absorption and the push pulse allows us to estimate the atom speed in the cavity. Rather than using the electronic signal that controls the pulses, the triggering is activated by monitoring stray light from push beam optical components. This avoids the possibility of additional delays.

For the push parameters used here, the time-of-flight is approximately $16 \pm$

---

[1] We might also consider the influence of any transverse component to the atom's velocity, as the atomic beam disperses, but this will result in a broadening of the transition, rather than a shift.

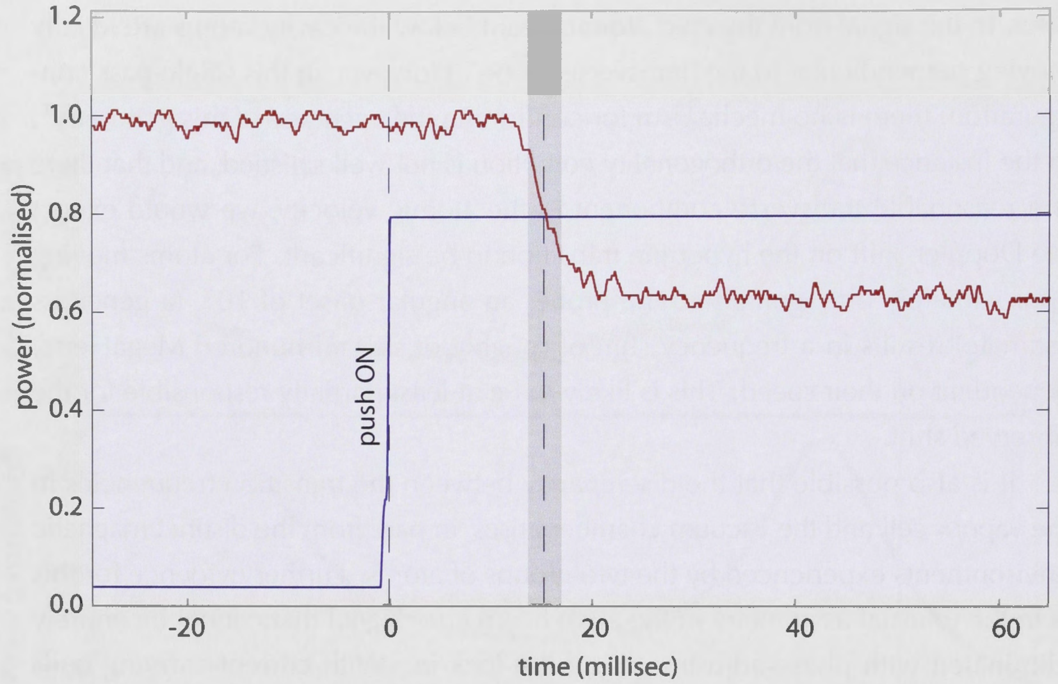

Figure 6.5: Atom absorption signal, transverse to the cavity axis (red trace). The blue trace shows the triggering of the push beam pulse. The absorption is maximum $\sim 16 \pm$ 3ms after the pulse is switched on.

3ms corresponding to a longitudinal velocity of about 25±5m/s. The power in the push beam and the length of time for which it operates influences the velocity distribution of the atoms once they reach the cavity. More power and longer pulses mean more photon absorption and emission processes each imparting a momentum 'kick' of $2\hbar k$.

6.3.3 Atom Flux and Intra-cavity Atom Number

Figure 6.6 shows a plot of how we might expect the number of atoms in the cavity volume to scale with their initial longitudinal velocity, $v_l(0)$ for an ideal 2D MOT source. The conditions modelled are for a transverse temperature in the 2D MOT of $T = 200 \pm 50\mu$K giving a transverse velocity of $v_{trans} = \sqrt{kT/m}$, where k is the Boltzmann constant ($k = 1.38 \times 10^{-23}$J/K) and $m = 1.44 \times 10^{-25}$kg is the mass of a rubidium atom. An estimate of the flux of atoms along the MOT axis is $F = 5 \times (10^7 - 10^8)$ atoms/s.

The red line in figure 6.6 shows the scaling of intra-cavity atom number for our best estimates of F and T while the shaded region indicates the uncertainty

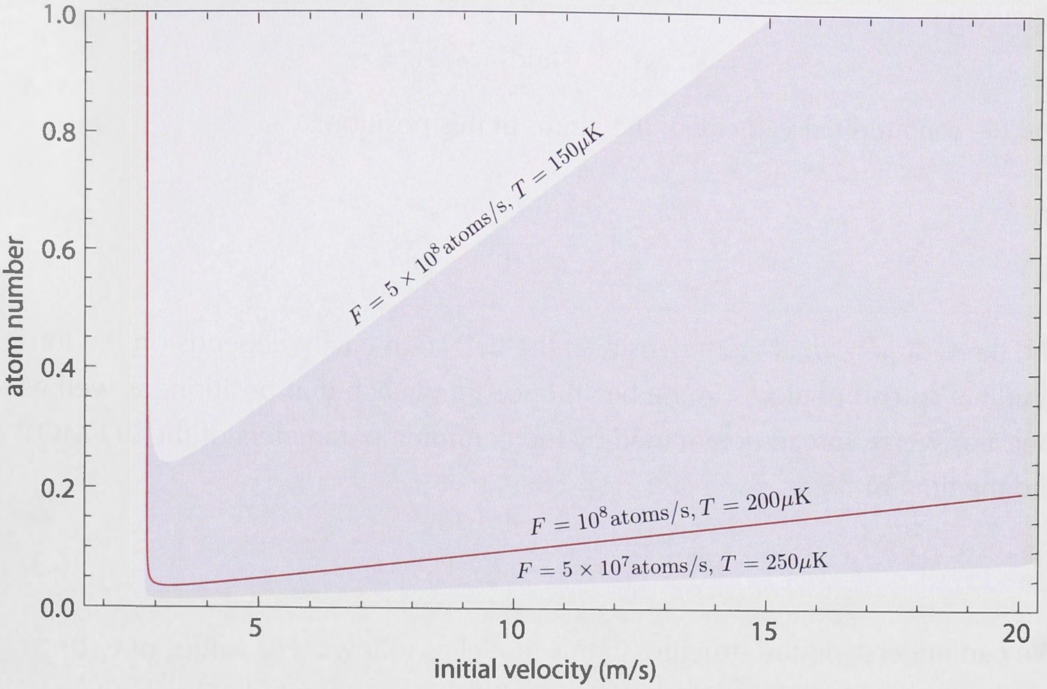

Figure 6.6: Linear scaling of atom number in the cavity volume as a function of initial longitudinal velocity. We model a 2D MOT with transverse temperature $\sim 200\mu$K, and longitudinal atom flux of 10^8atoms/s. The atom density scales as equation (6.3), and the number is given for the cavity mode volume defined by the parameters in table 5.1.

in this scaling due to the lack of precise values for F and T with plausible limits to these parameters indicated. The estimated values for F and T are based on models and measurements conducted on similar apparatus in a different cold atom experiment. The geometric layout of the present apparatus does not allow us to perform measurements to acquire the data necessary to determine these values for this experiment, but we believe they will be similar since the relevant conditions and those observations we *can* make are much the same.

The time-of-flight of the atoms from the trap to the cavity is related to their initial velocity, imparted by the push beam, with:

$$t = [v_l(0) - \sqrt{v_l(0)^2 - 2gd}]/g$$

Here d is the distance of the cavity above the trap (40cm) and g is the acceleration due to gravity. For the absorption signal shown in figure 6.5, $v_l(0) \sim 25 \pm 5$m/s.

We can calculate the radius and cross-sectional area of the atomic beam at the cavity;

$$r = v_{trans}t \qquad \text{and} \qquad A = \pi r^2$$

and the longitudinal velocity of the atoms at this position:

$$\begin{aligned} v_l(t) = & \quad v_l(0) - gt \\ = & \quad \sqrt{v_l(0)^2 - 2gd}. \end{aligned}$$

The three-dimensional atom density at the detection cavity depends on the longitudinal spread of atoms in the beam once they reach that position, as well as their transverse spread determined by the confining parameters of the 2D MOT and the time-of-flight:

$$n(\text{atoms/m}^3) = (F/A)/v_l(t) \tag{6.3}$$

We can understand the structure in this model as follows: For values of $v_l(0) \gg gd$, the term $1/A$ scales with the square of the initial longitudinal velocity and the final longitudinal velocity scales linearly with it. Since the density scales inversely with the cross-sectional area and the longitudinal velocity the number of atoms in the cavity scales linearly with $v_l(0)$. The behaviour shown at low velocity results from conditions where $v_l(0) \simeq gd$. For initial velocities below about $v_l(0) = 2.8$m/s atoms do not reach the cavity before turning around under the influence of the gravitational force.

Returning to our simulations of the signal-to-noise ratio presented in chapter 3, we can consider the influence of the atomic velocity by taking into account its affect on the atom trajectories, integration time (matching the transit time) and the mean number of atoms in the cavity, which scales linearly with the velocity as in figure 6.6. Figure 6.7 shows the modelled signal-to-noise ratio as a function of the longitudinal velocity of the atoms for resonant detection using all the same conditions deduced for optimum detection in chapter 3. The scaling limits relating the atom velocity and intracavity atom number are the same as those indicated in figure 6.6. The influence on the signal-to-noise ratio entering *via* the intracavity atom number scales the signal proportionally. For example, an intracavity atom number of 0.2 can be modelled as the average of one measurement of a single atom in the cavity to four measurements of an empty cavity signal. De-

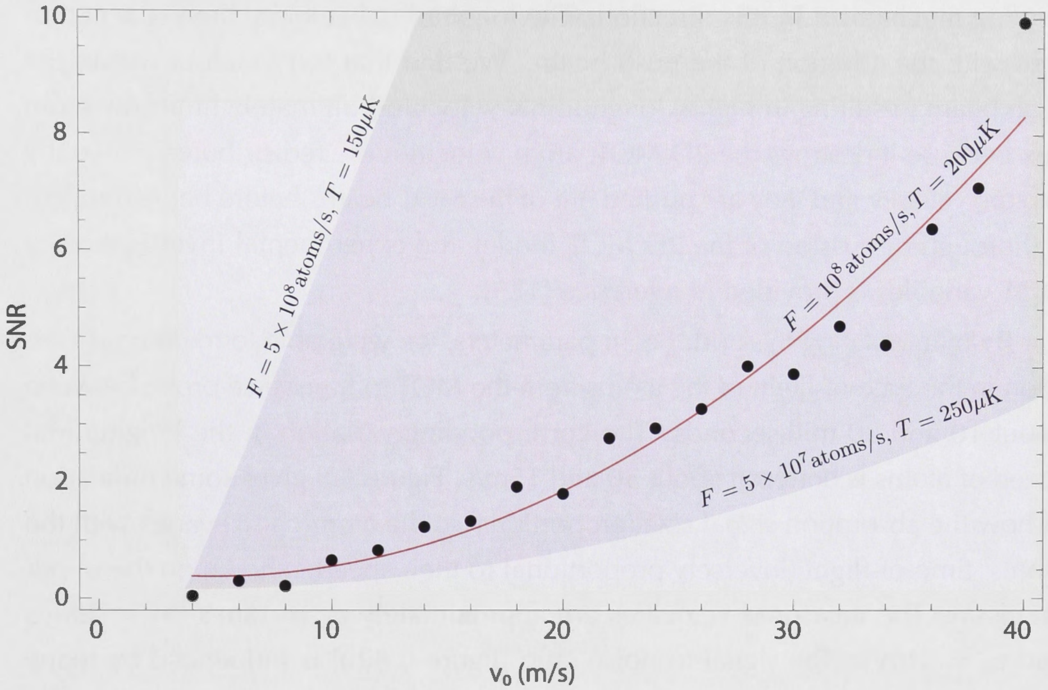

Figure 6.7: Modelled variation of signal-to-noise ratio with atom velocity. The simulation takes into account the scaling of the intra-cavity atom number with velocity, as well as the cavity transit times.

spite this proportionality, the relationship between the signal-to-noise ratio and the atomic velocity is quadratic rather than linear. This suggests that the nonlinear behaviour enters with the changing atomic transits and transit times as the longitudinal velocity is changed.

In fact, the scaling of the atomic flux with velocity is not so straight forward as that indicated in figure 6.6. It is not only the momentum imparted by the push beam but also the two-dimensional configuration of the source itself that determines the atoms' speed in the longitudinal dimension. In an ideal 2D trap we might imagine that atoms travel with a thermal (Maxwell-Boltzmann) velocity distribution in the third, untrapped dimension. However, since real MOTs are constructed with finite beam diameters, atoms in the high-velocity tail of the distribution move out of the trapping beams before they are substantially cooled in the transverse dimensions. Consequently only atoms that are initially slow enough in the longitudinal direction can be captured. The velocity distribution is truncated above this so-called 'capture velocity' even though there is no direct cooling mechanism in this direction. The longitudinal velocity limit is accentuated with the addition of the push beam. We find that too much power in the push beam (resulting in higher longitudinal velocities) ultimately limits the atom flux because it destroys the 2D MOT: atom velocities are redistributed above the capture velocity and they are pushed out of the MOT beams before being trapped. A thorough discussion of the 2D MOT model and experimental investigation of MOT variables is provided in reference [129].

By manipulating the push beam parameters, we were able to measure a variation in the time-of-flight of the atoms from the MOT to transverse probe between about 10 and 30 milliseconds. The corresponding variation in the longitudinal speed of atoms is between about 30 and 15m/s. Figure 6.8 gives some indication of how the absorption signal size (proportional to the atomic flux) varies with the atoms' time-of-flight (inversely proportional to their speed - shown on the upper abscissa). The measured velocities are approximately $v_1 = 15$m/s, $v_2 = 20$m/s and $v_3 = 31$m/s. The signal-to-noise ratio [figure 6.8(b)] is influenced by many parameters of the signal acquisition process, but for the traces shown in this plot all conditions of the data acquisition process were identical and only the push beam parameters were varied. We therefore presume that changes in the signal-to-noise ratio are an indication of changes in the atomic flux through the beam area.

The push beam pulse length could be varied using an electronic switch controlled with a programmable function generator and power was changed by rotating a wave plate in front of a polarising beam-splitter. For the measurements in figure 6.5 we used 10 millisecond pulses and adjusted the power.

At low velocities the drop in signal-to-noise ratio is a result of the scaling indicated in figure 6.6 and at high velocity it is due to the breakdown of the 2D MOT capturing ability. The optimum atomic flux - resulting in the best signal-to-noise ratio - occurs at a compromise of these behaviours.

6.4 Results: Pulsed Cavity Probe Beam Signal

Once the lock-in signal observed with the transverse probe has been optimised, we return to searching for an atom signal in the longitudinal cavity probe beam. From this point, very subtle adjustments of the alignment of the push beam eventually yielded a weak signal, best observed as the differential power change as

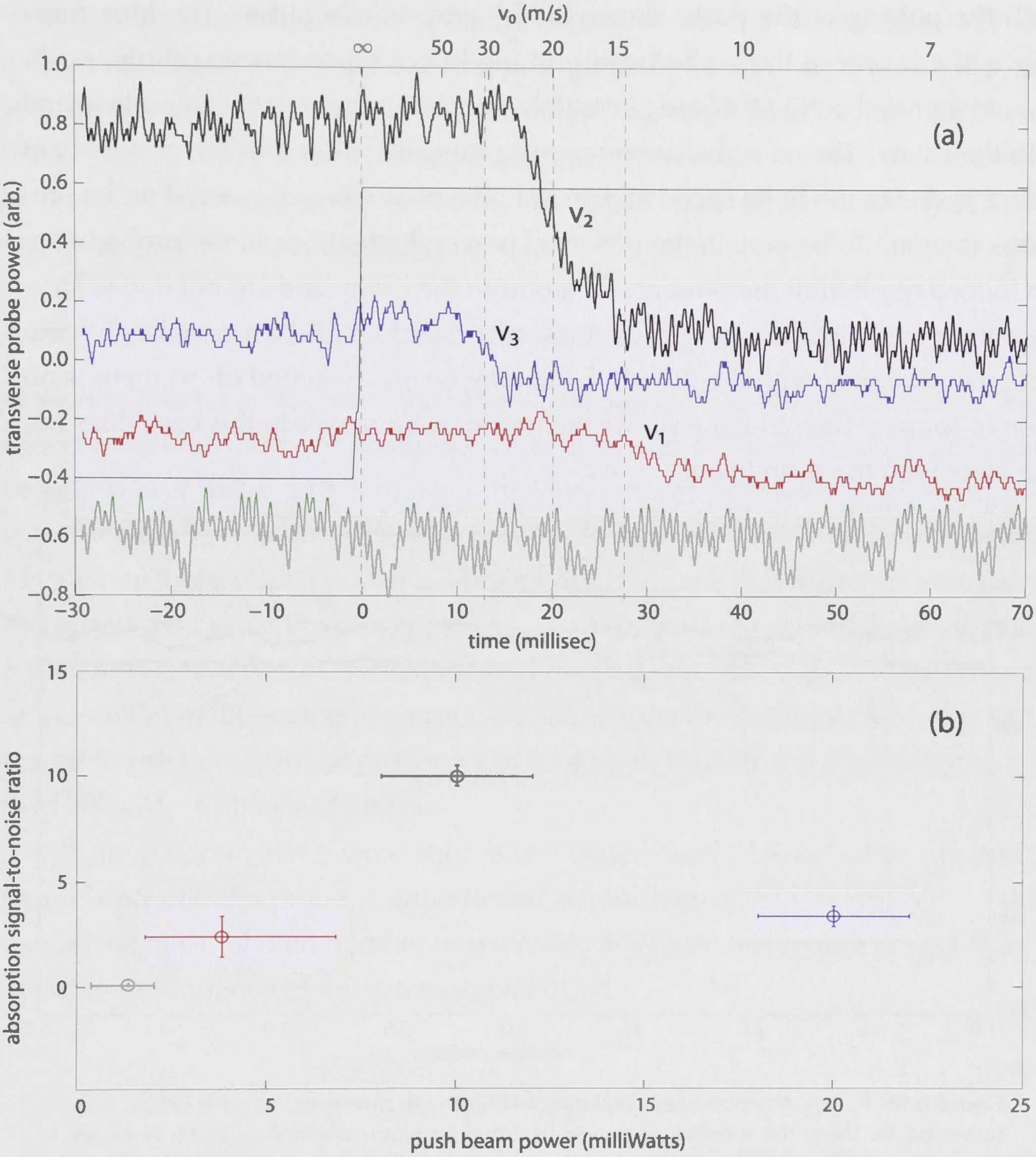

Figure 6.8: Variation in absorption signal strength with atom speed. Push beam power was adjusted to achieve a variation in atom speed. In (a) the changing strength of the absorption signal in the transverse probe beam is shown as a function of the time-of-flight of atoms from the 2D MOT and their speed. The change in signal-to-noise ratio of the absorption signal as a function of the push power is presented in (b).

the push is pulsed on and off. Figure 6.9 shows a typical recording of the probe beam power as the push beam is pulsed on and off with a frequency in this case of 2Hz. These data are acquired on an oscilloscope whose display is triggered with the pulsing of the push, shown as the grey square pulse. The blue trace shows the power in the probe beam pulsing in correspondence with the push, as atoms from the 2D MOT are alternately trapped in the quartz cell and ejected into the cavity. The offset between the push (trigger) pulses and the probe beam pulses is due to the finite speed and arrival time of atoms as discussed in the previous section. To be certain the observed power fluctuations in the probe beam do indeed result from the presence of atoms in the cavity and are not due to stray light from the pulsed push beam or some other spurious affect, we make an identical measurement with the 2D MOT trapping beams switched off so there is no atomic source. The red trace shows the probe beam power in this case does not fluctuate with the push beam.

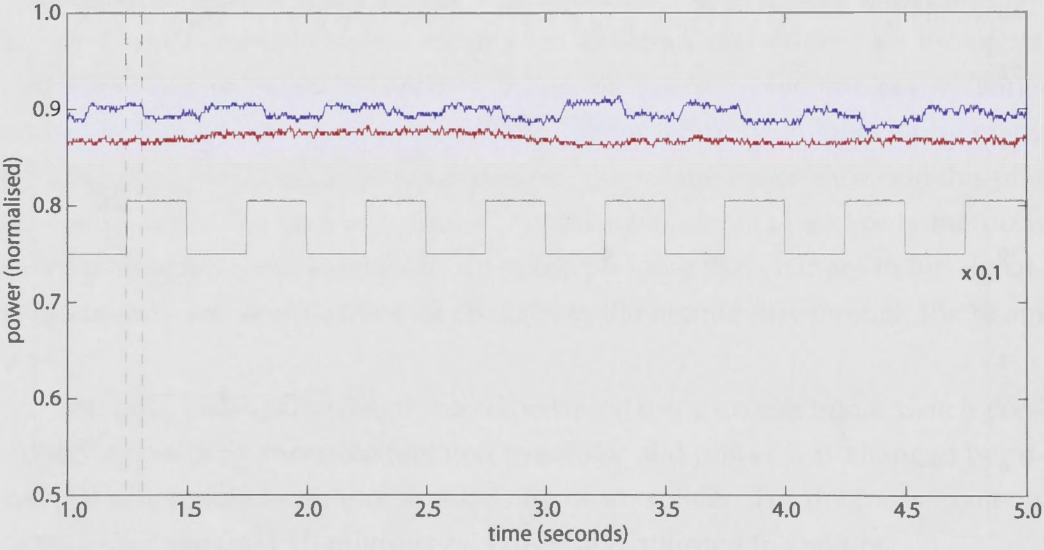

Figure 6.9: Pulses of probe beam power consistent with pulses of the push beam. The upper traces show the monitored power in the push beam when the 2D MOT in on (blue trace) and off (red trace) and the lower square pulse is monitored stray light from the push beam.

Figure 6.10(a) shows two seconds worth of monitoring the probe beam using our data acquisition program. Data are recorded with a resolution of 2μs and can subsequently be re-sampled into different bin sizes to extract the best signal-to-noise ratio.

A Fourier analysis of the raw data [figure 6.10(b)] shows that low frequency noise overwhelms the push beam pulses. To emphasise the bursts of atoms as changes in the probe power, we apply a filter to remove the low frequencies, shown as a shaded region in (b). Figure 6.10(c) shows the filtered data. We fit a sinusoidal signal (red trace) with the push pulse frequency of 10Hz in order to sort the data so that those incidents corresponding to the push beam 'off' (when the fit trace is above zero) can be grouped together as well as those for the push beam being 'on' (fit trace below zero). The relative size of the atom signal and noise can then be easily extracted.

6.5 Noise and Calibration Troubleshooting

In section 5.5.4, we discussed the procedure used to roughly calibrate the probe power measurements: we measured the probe beam at the heterodyne detector using a power meter and compared the values to the beatnote signal on an RF spectrum analyser and the signal recorded on our LabVIEW® interface in order to calibrate these displays. That calibration was performed at higher powers than the experiment since the power meter is not responsive to powers lower than a few nanoWatts. It was only intended as a rough guide, allowing us to determine an approximate operating power for the experiment by extrapolation. We had hoped to use the statistical properties of shot noise to scale the arbitrary units of the LabVIEW® display as follows:

If the photon source were shot-noise limited then (at least when the push beam is off and the probe is unperturbed by the presence of atoms) we would expect the mean photon number measured in any given integration time, τ to be equal to the variance of those measurements;

$$\mu = \sigma^2 \tag{6.4}$$

An arbitrary factor, k introduced with the measurement process means that the mean number displayed in our data acquisition program, μ' with standard deviation σ' is related to the actual number by $\mu = k \times \mu'$ (And $\sigma = k \times \sigma'$). Using equation (6.4) we could find the gain factor by setting

$$k \times \mu' = (k \times \sigma')^2.$$

In practical terms, varying the mean photon number can be achieved either by changing the power in the probe (as was the procedure in the rough calibration method of chapter 5) or by changing the integration time, τ. In figure 6.11 we plot

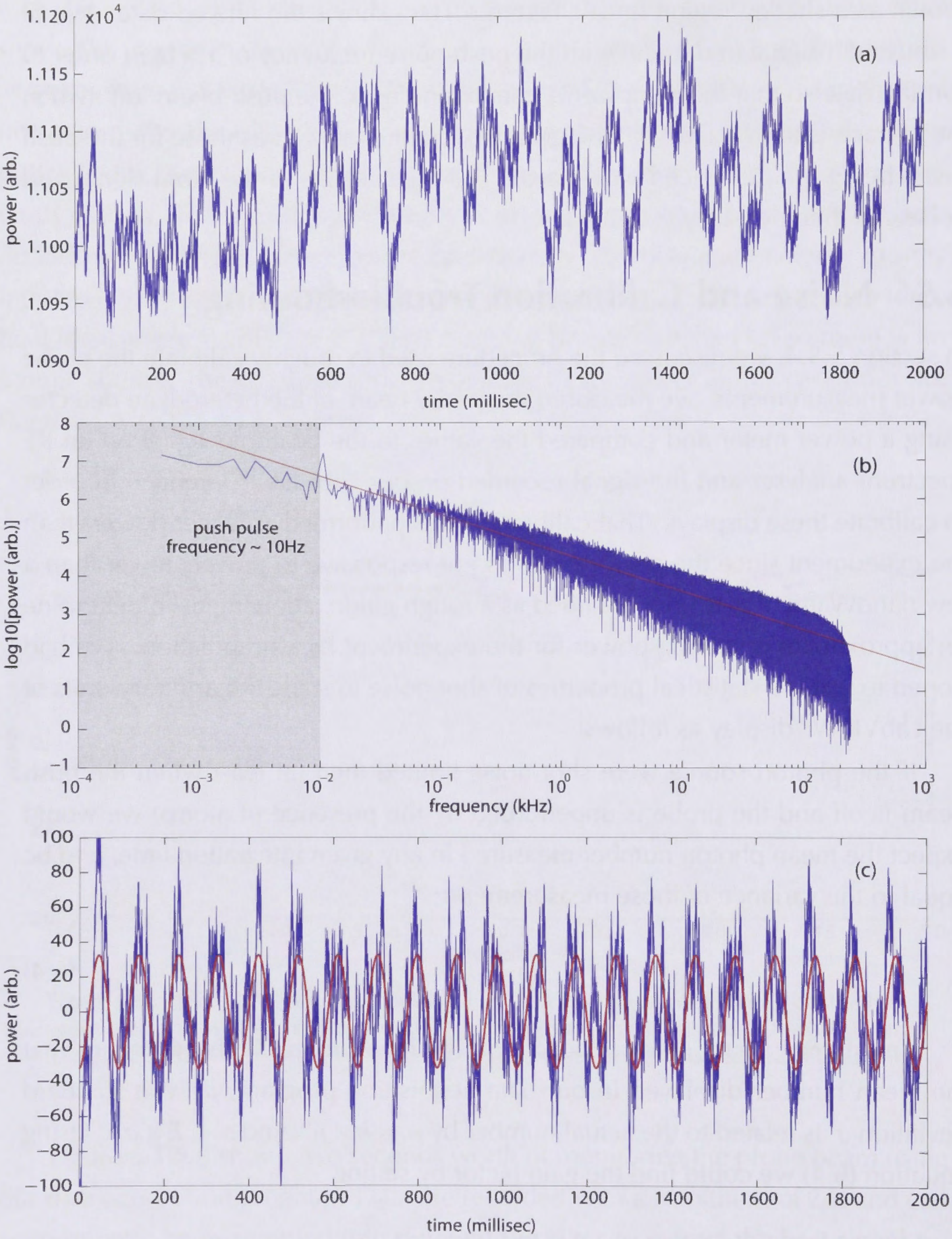

Figure 6.10: (a) Two seconds of data recorded during the pulsing of the push beam. (b) Fast Fourier Transform (FFT) of probe data. The push beam pulse frequency is 100 milliseconds. Low frequency noise dominates the time series so to better observe the pulses of atoms we filter out Fourier components below the push pulse frequency: (c).
]

the variance of the photon counts divided by the mean as a function of the 'bin length', or integration time. We consider measured data when the push beam is on and off separately, as well as the same information for a simulated data set of white Poissonian noise (shot noise).

Figure 6.11 makes use of the data from figure 6.10(c), where we have applied a high pass filter to remove the frequency noise below the pulse frequency in order to separate the data corresponding to 'atoms ON' and 'atoms OFF' states. The raw data are measured at a rate of $2\mu s$, and in figure 6.11 they are resampled with a decimation factor of 500. The statistical uncertainty - shown as the shaded regions around each trace - indicates the standard error in the resampled values. We had hoped that the blue trace - corresponding to data measured when no atoms were present - would show a unvarying value for this ratio that could be scaled to produce unity indicating noise dominated by photon shot-noise. More noise at lower frequencies means that when a long data sample is taken (a sample that spans a long time period) the ratio of the standard deviation to the mean counts is higher than for shorter samples and so there is no unique value of k that we can find to scale our arbitrary units. Consequently, we cannot employ the above approach to determine the power in the detection cavity. In fact, the noise features described here can be extracted immediately from figure 6.10(b) where it is clear that even above the filter cut-off the power in different frequency components varies across the spectrum such that the fourier transform is not flat in frequency space: the signal is *not* dominated by photon shot noise as we had hoped.

The attempted calibration method described above is a post-processing operation. During the experiment, we did not endeavour to set the probe power using an analysis of the noise spectrum. Instead, we followed the procedure discussed in section 5.5.4; checking the heterodyne beatnote amplitude on an RF spectrum analyser before recording the signal allows a measurement of the probe power, using equation (5.3). The reader is reminded that the electrical power in this beatnote is proportional to the optical probe power but also to the optical power in the LO so one must be careful to maintain a constant power in the latter between measurements. Once a signal is observed, the power in the probe beam can be subtly adjusted using the AOM controller until the optimum signal-to-noise ratio is reached.

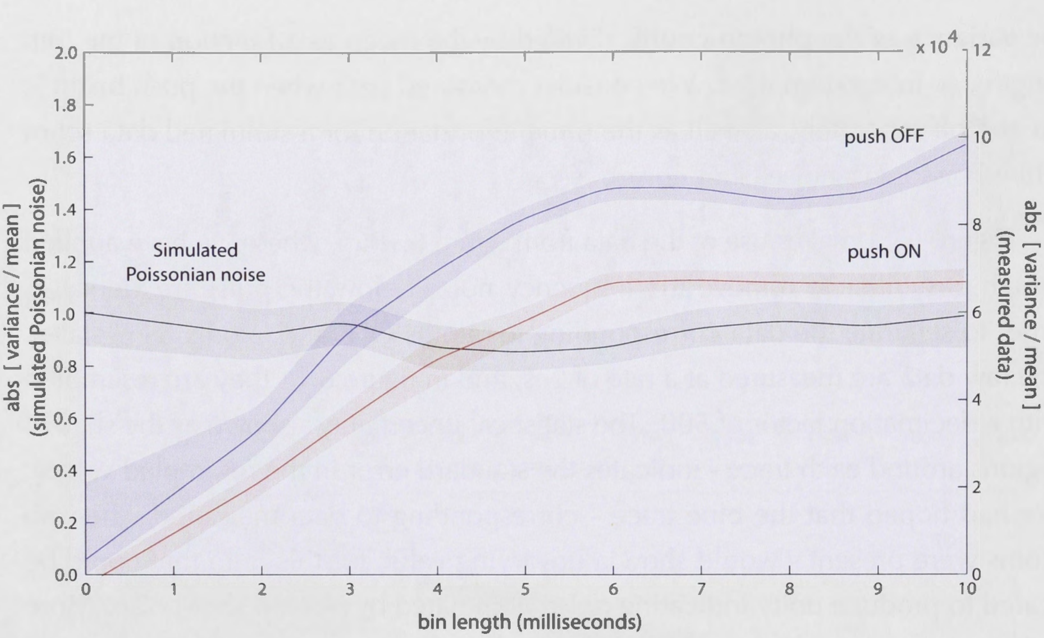

Figure 6.11: Scaling of the standard deviation with sample size. The black trace is simulated data exhibiting Poissonian noise for which the ratio of the variance to the mean is always one, regardless of sample size. The blue and red traces are measured data, scaled for ease of comparison. The blue data are measured with the push beam off and the red when it is on.

6.5.1 Comparison with Other Work

Atomic Shot Noise

Despite the excess noise in our measurement procedure, the plot in figure 6.11 provides us with one interesting observation. The two traces corresponding to experimental measurements are from the cavity probe with the atom beam on, and off, as indicated. While neither trace is flat - that is, shot noise limited - like the simulated Poissonian data, there is a noticeable difference between them: the ratio of variance to mean for the data corresponding to atoms in the cavity is consistently *lower* than for the empty cavity data.

In our simulations in part I - and from a simple intuitive perspective - the above observation is the opposite trend to what one would expect. Indeed, exactly that opposite trend is observed using the fluorescence detector described in reference [145]. A coherent light source of constant mean photon number creates a Poisson distributed photon stream with the probability of detecting n

photons in a given measurement time given by

$$p(n) = \frac{\langle n\rangle^n}{n!}e^{-\langle n\rangle} \tag{6.5}$$

and a variance that equals the mean:

$$\frac{\mathsf{Var}(n)}{\langle n\rangle} = 1.$$

Atoms passing the detection fibre create a fluorescence signal with a mean number of counts per atom α, so that for m atoms the probability of n counts becomes

$$p(n) = \frac{(\alpha m)^n}{n!}e^{-\langle \alpha m\rangle}$$

where we have substituted αm for $\langle n\rangle$ in equation (6.5). For a source of atoms with probability distribution $p_{\mathsf{atom}}(m)$ super-Poissonian statistics are observed: (see appendix D)

$$\begin{aligned}\frac{\mathsf{Var}(n)}{\langle n\rangle} &= 1+\alpha\frac{\mathsf{Var}(m)}{\langle n_0\rangle/\alpha+\langle m\rangle}\\ &\sim 1+\alpha\frac{\mathsf{Var}(m)}{\langle m\rangle}\end{aligned} \tag{6.6}$$

Here $\langle n_0\rangle$ is the mean background photon count that may be neglected in some apparatus.

Co-operative Noise Reduction

Of course, a fluorescence detector behaves differently from a cavity detector, although we might still expect an increase in the relative variance of photon counts per measurement interval when atoms are present in the detection region. However, in contrast to the observations in [145], the authors of reference [55] do not measure a significant increase in noise accompanying the atom signal. In fact, they refer to the *lack of increase* as 'co-operative noise reduction' since it represents a suppression of atomic shot-noise resulting from the generalised multi-atom co-operativity parameter C_N. Their work involves atom detection within a small cavity mode *via* fluorescence and resonant cavity reflection measurements, both of which result in an increase in photon counts.

The significance of cavity detection enters *via* the co-operativity parameter C, (introduced in chapter 3) that describes the effect of a single atom on the cavity spectrum and the multi-atom co-operativity parameter scales with the effective number of atoms in the cavity as $C_N = N_{\text{eff}}C$. The effective intra-cavity atom number is found from the overlap of the atomic and cavity mode spatial density functions:

$$N_{\text{eff}} = \int_0^L \int_{-\infty}^{\infty} \int_{-\infty}^{\infty} [\varrho(\boldsymbol{r})|U(\boldsymbol{r})|^2] \, d^3\boldsymbol{r}.$$

The mean number of photon counts per atom, α is related to the co-operativity parameter *via* different relations depending on the nature of the detection technique [55]. The authors note that they cannot simply replace m with N_{eff} in equation (6.6), since when dealing with noise the two are not interchangeable. They find that by using an analytic result $\text{Var}(N_{\text{eff}})/N_{\text{eff}} = 3/8$, derived from work by Carmichael and Sanders [31], and by treating C_N as a random variable proportional to N_{eff} rather than $\langle N_{\text{eff}}\rangle$, the calculated ratio $\text{Var}(n)/\langle n\rangle$ is remarkably close to Poisson statistics and is in excellent agreement with their observations[2].

If cavity *transmission* is observed instead of reflection or fluorescence, then an atom in a resonant detection cavity removes - rather than adds - on average α photons from a shot noise limited probe beam. Proceeding with the same working (appendix D), equation (6.6) becomes:

$$\frac{\text{Var}(n)}{\langle n\rangle} = 1 + \alpha\frac{\text{Var}(m)}{\langle n_0\rangle/\alpha - \langle m\rangle} \tag{6.7}$$

where $\langle n_0\rangle$ cannot be ignored. Since the number of photons removed from the probe beam cannot exceed $\langle n_0\rangle$, the second term in equation (6.7) must be positive, and one would expect the relative variance to increase above the Poissonian value of unity. However we need to consider the co-operative noise suppression due to the statistical nature of the collective atomic dipole (observed previously in reflection [55]). This reduces the significance of this second term in (6.7), so that Poissonian statistics continue to dominate when atoms are present, regardless of the nature of the atomic distribution. But the derivation of equation (6.7) assumes photon detection at the shot-noise limit. Our measurements are not shot-noise

---

[2] Note that the observations in [55] do not negate the results presented in reference [145] since in that work atoms where detected close to a fibre input but not within a cavity mode, so issues regarding co-operativity parameters do not arise.

limited - even in the absence of atoms we don't observe Poissonian statistics - and we measure a significant *reduction* in the photon noise when atoms are detected, *below* the level of the probe when the cavity is without atoms: see figure 6.11. We can only conclude that this reduction in the excess photon noise is due to the attenuating influence of the atoms.

For a beam of photons with relative variance $V_0 \equiv \text{Var}(n_0)/\langle n_0 \rangle$, the effect of attenuation, can be modelled as a beamsplitter with a transmission η and an empty port that introduces a quantum vacuum $\delta\nu$:

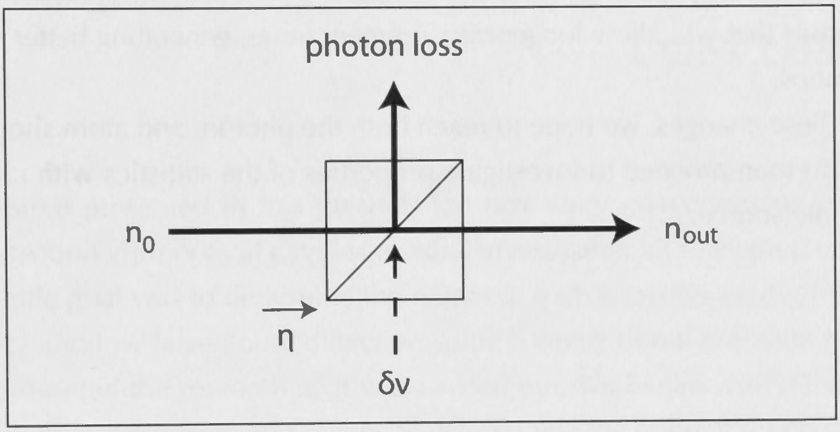

Figure 6.12: A model of photon attenuation by a factor (1-η)

The relative variance due to this attenuation is found to be [25]:

$$\begin{aligned} V_{\text{out}} &= \eta V_0 + (1-\eta) \\ &= \eta(V_0 - 1) + 1 \end{aligned}$$

In the instance of a shot-noise limited source ($V_0 = 1$) the relative variance of the attenuated beam remains the same. If the photon source is squeezed ($V_0 < 1$) the output variance increases with attenuation - in other words, the squeezing is reduced - but for a noisy photon source ($V_0 > 1$) the relative noise is suppressed. This is the effect observed in our cavity atom measurements.

6.6 Summary

Here, I have presented our first attempts at an experimental implementation of the cavity-detection set-up. Our moderate-finesse cavity has been used to observe an atomic beam from a 2D MOT, but we were not able to measure single-atom transits or to calibrate the atom number and measure atomic shot-noise. The main limitation is excess photon noise in the system that has yet to be eliminated. This might require active power feedback to our lasers, or a reconfiguration of optical components where possible, to limit pointing errors in beam positions, and misalignment of polarisation-sensitive devices.

We also noted that the atomic source we have used produced atoms moving through the detection-cavity much faster than in the modelled system. We will move to a new set-up, where a different source of atoms will be used to achieve slower transits that will allow longer measurement times, generating better signal-to-noise ratios.

With these changes, we hope to reach both the photon, and atom shot-noise limit, and to then proceed to investigate properties of the statistics with changes in the atomic source.

CHAPTER

SEVEN

CONCLUSIONS

The research presented in this thesis is the first study concentrating on single-atom detection with optical cavities to have investigated all relevant parameters. The specific goal was to determine the merits of such a system for high quantum efficiency and low false-count detection using a cavity of only moderate finesse. I have presented the research as it was carried out; we began with a theoretical examination of the system as a means to determining the optimal set-up. We then proceeded with the practical construction of the experimental system, aiming to demonstrate the modelled parameters.

7.1 Related Work

Prior to the commencement of this work, several experimental studies investigated atom detection using optical cavities - for example, references [93, 70, 104, 42, 101] - and one in particular demonstrated a *low*-finesse cavity used to detect single atoms with good sensitivity: reference [60]. This significant result has great relevance to the motivation of our work. That was a practical study, however, so necessarily there were experimental restrictions on the variables under investigation, and it cannot be said that the results demonstrate an optimisation of detection sensitivity or efficiency.

Some previous modelling work has considered cavities in the context of atom detection, but the scope of these studies has tended to be more limited than that presented in this thesis: Horak *et al.* investigated optical cavity detection of single atoms using microcavities [73]. While their work covered a reasonable-sized parameter space, their models were entirely classical. As we have demonstrated in our own simulations (chapter 3), classical models produce many of the correct qualitative features, but are not quantitatively accurate in all regimes, and are therefore inappropriate for a realistic determination of optimal detection parameters. In reference [109], a quantum model was used to explore the effect of detunings on the signal-to-noise ratio. These investigations however, do not consider variation of the probe power, since they are interested in the single atom *and single photon* regime that is the focus of cavity QED experiments. This is a significant restriction since one of our key results concerns the necessary variation of probe power with detuning, for the maintenance of high signal-to-noise ratios.

7.2 Summary of Modelling Work

Our first simulations considered the optimal signal-to-noise ratio for the detection of a single atom maximally coupled to the mode of a cavity with moderate finesse. In contrast with much of the recent work involving cavities and atoms - for a varied selection, consider references [92, 109, 102, 19, 101, 22, 140, 94] - this research was *not* fundamentally motivated by the regime of strong coupling, and high co-operativity parameters required in cavity QED. In cavity QED studies, the requirements of strong coupling place restrictions on the nature of cavities used and their modes of operation. High-finesse and/or small mode volumes are key objectives since they increase the atom-cavity coupling parameter, g_0. Generally very-low photon numbers are required, since the regime is concerned with the interactions between single (or at most, only a few) quanta: one atom, and one photon [92, 6, 109].

In our work, low photon number was not necessarily an objective. In fact, photon number (power) was one of the variables we considered in our quest for high signal-to-noise ratios. We considered a wide range of parameters that influence the detection, including characteristics of the cavity - such as its mirror quality (finesse) and length - as well as those of the operating conditions: probe power, detunings, and a comparison of the photon detection techniques presented with single photon counting and heterodyne detection of phase and amplitude quadratures.

The modelling was subsequently extended to more realistic considerations, in particular the atom trajectories through different coupling strengths in the cavity mode and the influence on the signal-to-noise ratio. We were specifically interested in the quantum efficiency and dark noise of the detector.

From these theoretical studies, we conclude that moderate-finesse cavity-based single atom detection is capable of very good signal-to-noise ratios and, more importantly, high quantum efficiencies, provided it is used appropriately. We deduced that the finesse of a detection cavity does not need to be very high for good detection, provided the intra-cavity power in the probe beam corresponds to the saturation intensity of the atom. When the finesse is relatively low (this thesis has addressed a cavity with a finesse of 10^4) that condition is satisfied for a reasonably strong probe (in the order of picoWatts for resonant detection to nanoWatts for a detuned probe) and so photon detection is best performed with heterodyne detection rather than avalanche photo diodes, which saturate at very low power. The detection efficiency is improved with detuned detection (accompanied with an increase in probe power, to maintain saturation intensity) because the dipole force can be used to channel atoms into regions of strong coupling within the cavity mode.

7.3 Summary of the Experimental Set-up

Our simulations illustrated that cavity-based detection with cavities of only moderate finesse, is indeed feasible as a means to high quantum efficiency, low-noise single atom detection. It would have been desirable to experimentally demonstrate the modelled features of this system, and to then extend the investigation using a practical apparatus, whose properties were well-understood and established in theory. We were able to detect atoms with our apparatus, but two substantial problems stand in the way of a direct comparison between our current experimental measurements and the results from our simulations: (1) The present experimental observations of our probe beam are not shot-noise limited like our modelled data and (2) the atomic source results in substantially faster atoms than those in the modelled detection.

Reaching the Shot-Noise Limit

The most decisive improvement to this experiment will be reaching the photon shot-noise limit. Even without slow atoms, observations exhibiting noise that we are able to quantify will be far more useful in comparing with our simulated results for signal-to-noise ratio of cavity detection. Only then can we consider the more intriguing measurements concerning the atomic statistics.

Active power feedback is always an option for light sources exhibiting excess noise. In our set-up, the primary source of noise is due to polarisation drifts arising from our fibre-coupling, rather than power fluctuations at the laser or in other optical components. Although there will always be some cross-talk between orthogonal polarisations, it should be possible to align single-mode optical fibres sufficiently well to eliminate much of the polarisation rotation noise. Direct coupling of the probe and stabilisation lasers into the detection cavity might also be considered, although generally it is technically easier to minimise noise due to pointing errors when fibres are used.

New Atomic Source

We have tried to reconfigure the experimental set-up to use a 3D MOT dropped into the cavity chamber from above. The atoms from this source are initially stationary and the velocity they acquire having reached the detection cavity depends on how far they have fallen. In contrast to our 2D MOT set-up, we form the 3D MOT in the same vacuum chamber as the cavity itself, approximately 15cm above the cavity; atoms will be travelling at around 1.7m/s at the cavity mode.

The configuration is similar to that used in reference [60] (although the speed of atoms transiting the cavity in that experiment was closer to 0.6m/s). It introduces a higher pressure in the detection region than in our initial set-up using two separated vacua, since a reasonable background pressure of rubidium is necessary to form the MOT. We considered the risk that the signals from background atoms may overwhelm with the single atom detection. However, the un-trapped atoms constituting the background pressure travel with thermal velocities, so it is unlikely that they will be observed in the cavity detection measurement time; indeed, this was the point of concern with atoms from the 2D MOT source. Results are pending.

7.3.1 Further Work: Different Modes of Cavity Detection

As discussed in chapter 3, there is a plethora of variations on the use of an optical cavity for atom detection. Here, our experimental work has only just commenced the investigation of resonant detection *via* probe power measurements. The natural extension is to consider the parameter space defined by non-resonant regimes, with the accompanying variation in probe power and also to explore and compare the merits of detection using measurements of phase rotation.

The experimental work that our research group is currently investigating has an emphasis on inteferometry using atom laser beams. We are capable of very good, low noise, absorption imaging, but the next stage of many of our experiments will require atomic-shot noise limited detection with high bandwidth. The scheme will either be a cavity detector, such as that presented in this work, or a fluorescence set-up that we have yet to investigate. Integrating the cavity set-up with our atom laser will be a challenging process (as demonstrated by another research group [104]), but is the ultimate use of this 'root N' detection device.

7.4 Other Detection Techniques

7.4.1 Fluorescence Detection

The atomic sources that have been considered in this research have been untrapped cold, neutral atoms - specifically, rubidium 87. We have extensively studied cavity-based detection, and now in conclusion, we return to a discussion of other detection techniques, introduced in the preliminary chapters. Along with optical cavities, one of the likely candidates for high efficiency single-atom detection is *via* the monitoring of fluorescence photons. In a fluorescence detector, atoms are transferred to an excited state with an external field and the spontaneously emitted photons are detected. The sensitivity and the dark-noise of the detection scheme depend on the detection efficiency of the scattered light and the suppression of background photons. Since photo-detectors can have high quantum efficiency, it is the ability to collect the scattered light that limits the atom detection and a high numerical aperture optical set-up is required.

The technologies of fluorescence and cavity detectors differ in many ways, but there are also some similar considerations between the two schemes. Channelling the atomic beam into the detection region is always important, and because of the technical difficulties with achieving high-numerical aperture optics, a small detection region in a fluorescence set-up is usually desirable. The requirements on the size of the atomic beam are therefore stringent. The theoretical sensitivity (ie: the theoretical signal to noise ratio) of fluorescence detection in comparison to cavity-based detection is worth investigating, but so too are the practical considerations in building and using the detector as an integrated component of a cold-atom experiment.

Two studies in particular have gone some way to comparing fluorescence detection with a cavity-based system: in experiment [55], and more thoroughly in theoretical examinations [144]. Both these investigations were primarily concerned with fibre-based detectors in 'atom-chip' experiments, where miniaturisation is a natural objective. The advantage of fibres is that they can be easily handled using well established techniques, and in comparison to other on-chip technology, the fabrication of optical components using fibres does usually not require expensive and time consuming lithographic techniques.

However, while fibre-based on-chip detectors deliver small mode-volumes (cavities) or detection regions (fluorescence) at relatively minimal expense, experiments that are conducted entirely on-chip are restricted to miniaturised apparatus that limit the possibilities of the investigations. For example, we might consider atom interferometry with untrapped atoms. This usually requires diffraction or Raman transitions to split atoms into a coherent superposition of momentum states, where the components of each wave function are distinctly separated in space [39]. Increasing the spatial separation - *via* increasingly high-order photon momentum transfers, or with longer propagation time before the states are recombined - improves the sensitivity of the interferometric measure but generally increased spatial separation will be at odds with the miniaturised geometry of atom chips. This is not to say that chip experiments are without their merits, nor does it rule out fibre-based detection (*via* fluorescence or cavities), but calls for further investigation comparing the two detection techniques realised in a broader context.

7.4.2 But what is it used for?

We have established that moderate-finesse cavity-based detection is a possible means for high-quantum efficiency single-atom detection, and our theoretical modelling has determined where, and how, in the extensive parameter-space, is realistically best to operate. However, cavity-detection is not a simple scheme to implement. Even with moderate finesse mirrors - with which we can eshew some of the complications such as bi-refringence that often occur in ultra-high finesse coatings - the system is complex and procedure delicate to perform. Finally, we return to the driving motivation for this research: Is high-quantum efficiency of single atoms in fact an important objective?

Perhaps where statistics are concerned, in quantum mechanical measurements such as Hanbury Brown Twiss correlation measurements with atoms [127, 77, 143, 103], near unity quantum efficiency is superfluous, and the *'root N'* detection requirement discussed in the introduction and in chapter 4.1 is sufficient. That requirement is most simply attained using microchannel plate (MCP) detectors, that are much easier than cavities to use [127, 143, 115]. Such detectors are usually used in conjunction with highly excited atoms such as meta-stable helium, or ions. For more versatility, a somewhat similar scheme has been suggested for the detection of photo-ionised atoms (in principle, atoms of any element) with better than $N^{-1/2}$ sensitivity [29]. Electro-ionised atoms have been measured with efficiencies of around 12% [52]. These detectors do not provide the highest quantum efficiencies, but to date - as demonstrated with their track record in published results - have proved to be the most appropriate for quantum statistical measurements.

As always, we can assimilate a lesson from the photon quantum opticians: where measurement of squeezing is desired/required then high quantum efficiency photodetectors are used in heterodyne or homodyne configurations, since the loss of photons anywhere in the system immediately degrades the level of squeezing that is measured. Elsewhere in quantum optics, single quanta (photons) can be recorded using avalanche photo diodes, at the expense of quantum efficiency, but the gain of simplicity. Similarly in quantum atom optics, it is unlikely that a single device will be the ultimate solution for the detection criteria of every investigation. Some measurements are best aided with low-quantum efficiency, but fast and simple MCP or ion detectors, but when measuring squeezing in an atom beam, high quantum efficiency detection will be paramount, and a scheme such as the cavity detection presented in this thesis is appropriate.

APPENDIX

A

MATHEMATICA® CODE

```
(*System and measurement parameters*)
lightspeed = 3 * 10^8;     (*μm/μs*)
λ = 780 * 10^-3;           (*μm*)
τ = 20;                   (*integration time, μs*)
w0 = 20;                  (*beam waist, μm*)
cavitylength = 100;       (*μm*)
A = π * w0^2;              (*beam cross sectional area, μm^2*)
Γ = ((26 * 10^-9)^-1) * 10^-6 ; (*natural atomic decay rate, MHz*)
σ0 = 3 λ^2 / (2 π);           (*resonant atomic cross section, μm^2*)
g = Sqrt[σ0 Γ lightspeed / (A * cavitylength)]; (*atom-cavity
                                       coupling freq, MHz*)
sat = Γ / (2 σ0);         (*saturation flux, photons μm^2/μs*)
logRef = 4;               (*-log10[1-mirror reflectivity]*)
(*atom-laser detuning*)
θmin = -40 Γ;
θmax = 40 Γ;
θpoints = 71;
θstep = (θmax - θmin) / (θpoints - 1);
(*cavity-laser detuning*)
Δmin = -10 κ;
Δmax = 10 κ;
Δpoints = 71;
Δstep = (Δmax - Δmin) / (Δpoints - 1);
```

```
(*log10[input flux (photons/τ)]*)
fluxmin = 0;
fluxmax = 4;
fluxpoints = 21;
fluxstep =  fluxmax - fluxmin  /  fluxpoints - 1 ;

maxphoton = 0;
basistable = {};
Print[meanphotonnumber];
             ⎛lightspeed (1 - ( 1 - π 10^(-logRef)))      ⎞
xx = N[10^fluxmax / ⎜───────────────────────────────────── / 2⎟]
             ⎝             cavitylength                     ⎠
Print[maxbasissize]
Max[{ 3 + 5 Ceiling[11.5 Sqrt[xx] / 5 ], 3 + 5 Ceiling[(1.45 xx + 23.2) / 5]}]
(*cavity decay rate MHz*)
     lightspeed (π 10^(-logRef))
κ = ──────────────────────────────
           cavitylength

Clear[κ];
Clear[Δ];
Clear[ϵ];
Clear[θ];

dataarray = {};
fluxtable = {};
Table[
      lightspeed (π 10^(-logRef))
 κ = ──────────────────────────────;
            cavitylength
 data = Table[
   startphoton = maxphoton;
   (*set basis size*)
   maxphoton  = If[10^flux / (κ / 2) < 20,
      3 + 5 Ceiling[11.5 Sqrt[ 10^flux / (κ / 2)] / 5 ],
     3 + 5 Ceiling[(1.45 * 10^flux / (κ / 2) + 23.2) / 5]];

   Clear[Δ];
   Clear[ϵ];
   Clear[θ];

   If[maxphoton != startphoton,

    Clear[Δ];
    Clear[ϵ];
    Clear[θ];
```

```
    (*initialise density matrix*)
    densityfunction = Table[p[i], {i, 1, 4 maxphoton^2}];
    dims = {4 maxphoton^2, 4 maxphoton^2} → 0;

    (*Master equation coefficients*)
mgt0 = Table[{
        {4 (m + maxphoton n) + 1, 4 (m - 1 + maxphoton n) + 1} → ϵ √m ,
        {4 (m + maxphoton n) + 1, 4 (m - 1 + maxphoton n) + 3} → g √m ,
        {4 (m + maxphoton n) + 2, 4 (m - 1 + maxphoton n) + 2} → ϵ √m ,
        {4 (m + maxphoton n) + 3, 4 (m - 1 + maxphoton n) + 3} → ϵ √m ,
        {4 (m + maxphoton n) + 4, 4 (m - 1 + maxphoton n) + 4} → ϵ √m ,
        {4 (m + maxphoton n) + 4, 4 (m - 1 + maxphoton n) + 2} → g √m },
       {m, 1, maxphoton - 1}, {n, 0, maxphoton - 1}];
ngt0 = Table[{
        {4 (m + maxphoton n) + 1, 4 (m + maxphoton (n - 1)) + 1}   → ϵ √n ,
        {4 (m + maxphoton n) + 1, 4 (m + maxphoton (n - 1)) + 4}   → g √n ,
        {4 (m + maxphoton n) + 2, 4 (m + maxphoton (n - 1)) + 2}   → ϵ √n ,
        {4 (m + maxphoton n) + 3, 4 (m + maxphoton (n - 1)) + 3}   → ϵ √n ,
        {4 (m + maxphoton n) + 3, 4 (m + maxphoton (n - 1)) + 2}   → g √n ,
        {4 (m + maxphoton n) + 4, 4 (m + maxphoton (n - 1)) + 4}   → ϵ √n },
       {m, 0, maxphoton - 1}, {n, 1, maxphoton - 1}];
mlt = Table[{
        {4 (m + maxphoton n) + 1, 4 (m + 1 + maxphoton n) + 1} → ϵ √(m + 1) ,
        {4 (m + maxphoton n) + 2, 4 (m + 1 + maxphoton n) + 2} → ϵ √(m + 1) ,
        {4 (m + maxphoton n) + 2, 4 (m + 1 + maxphoton n) + 4} → g √(m + 1) ,
        {4 (m + maxphoton n) + 3, 4 (m + 1 + maxphoton n) + 3} → ϵ √(m + 1) ,
        {4 (m + maxphoton n) + 4, 4 (m + 1 + maxphoton n) + 4} → ϵ √(m + 1) ,
        {4 (m + maxphoton n) + 3, 4 (m + 1 + maxphoton n) + 1} → g √(m + 1) },
       {m, 0, maxphoton - 2}, {n, 0, maxphoton - 1}];
nlt = Table[{
        {4 (m + maxphoton n) + 1, 4 (m + maxphoton (n + 1)) + 1}   → ϵ √(n + 1) ,
        {4 (m + maxphoton n) + 2, 4 (m + maxphoton (n + 1)) + 2}   → ϵ √(n + 1) ,
        {4 (m + maxphoton n) + 2, 4 (m + maxphoton (n + 1)) + 3}   → g √(n + 1) ,
        {4 (m + maxphoton n) + 3, 4 (m + maxphoton (n + 1)) + 3}   → ϵ √(n + 1) ,
        {4 (m + maxphoton n) + 4, 4 (m + maxphoton (n + 1)) + 4}   → ϵ √(n + 1) ,
        {4 (m + maxphoton n) + 4, 4 (m + maxphoton (n + 1)) + 1}   → g √(n + 1) },
       {m, 0, maxphoton - 1}, {n, 0, maxphoton - 2}];
```

```
nandmlt = Table[{
      {4 (m + maxphoton n) + 1, 4 (m + 1 + maxphoton (n + 1)) + 1} → κ √(n + 1) (m + 1) ,
      {4 (m + maxphoton n) + 2, 4 (m + 1 + maxphoton (n + 1)) + 2} → κ √(n + 1) (m + 1) ,
      {4 (m + maxphoton n) + 3, 4 (m + 1 + maxphoton (n + 1)) + 3} → κ √(n + 1) (m + 1) ,
      {4 (m + maxphoton n) + 4, 4 (m + 1 + maxphoton (n + 1)) + 4} → κ √(n + 1) (m + 1) ,
      {m, 0, maxphoton - 2}, {n, 0, maxphoton - 2}];
nandmfree = Table[{
      {4 (m + maxphoton n) + 1, 4 (m + maxphoton n) + 1} → ⅈ Δ (m - n) - κ / 2 (m + n),
      {4 (m + maxphoton n) + 1, 4 (m + maxphoton n) + 2} → Γ,
      {4 (m + maxphoton n) + 2, 4 (m + maxphoton n) + 2} → ⅈ Δ (m - n) - κ / 2 (m + n) - Γ,
      {4 (m + maxphoton n) + 3, 4 (m + maxphoton n) + 3} → ⅈ(Δ (m - n) + θ) - κ / 2 (m + n) - Γ / 2,
      {4 (m + maxphoton n) + 4, 4 (m + maxphoton n) + 4} → ⅈ(Δ (m - n) + θ) - κ / 2 (m + n) - Γ / 2,
     {m, 0, maxphoton - 1}, {n, 0, maxphoton - 1}];

   (*Matrix of coefficients,
   dropping the first row so that it can be replaced with trace 1*)
   coeffic = Drop[
     SparseArray[Flatten[{dims, mgt0, ngt0, mlt, nlt, nandmlt, nandmfree}]],
     {1, 1}];
   (*equation for trace 1*)
   traceeq =
    Sum[p[4 ((maxphoton + 1) (i)) + 1] + p[4 ((maxphoton + 1) (i)) + 2],
      {i, 0, maxphoton - 1}]   1;
   (*The row that goes in the matrix*)
   extratracerow = CoefficientArrays[traceeq, densityfunction][[2]];
   (*New Matrix with new last row*)
   M = Insert[coeffic, extratracerow, 4 maxphoton^2];
   (*solution vector with final element=1*)
   v = SparseArray[{4 maxphoton^2}   1];
   (*Clear useless stuff from precious memory*)
   Unprotect[In, Out];
   Clear[mgt0, ngt0, mlt, nlt, nandmlt, nandmfree, In, Out, coeffic];
   Protect[In, Out];
  ];
 (*Solve equations over and over again over different values of ϵ *)

      lightspeed (π 10^(-logRef))
κ = ───────────────────────────── ;
            cavitylength
Δ = Δd;
θ = θd;
ϵ  = N[√10^flux / (κ / 2) Sqrt[(κ / 2)^2]];
```

```
   solution = LinearSolve[N[M], N[v]];
   (*matrix for |g><g|*)
   ρ1 = Chop[Table[solution[[4 (tc + tr * maxphoton) + 1]],
      {tr, 0, maxphoton - 1}, {tc, 0, maxphoton - 1}]];
   (*matrix for |e><e|*)
   ρ2 = Chop[Table[solution[[4 (tc + tr * maxphoton) + 2]],
      {tr, 0, maxphoton - 1}, {tc, 0, maxphoton - 1}]];
   adag = SparseArray[{{m_, n_} /; (m - n)} == 1 → Sqrt[m - 1]},
     {maxphoton, maxphoton}];
   a = SparseArray[{{m_, n_} /; (n - m) == 1 → Sqrt[n - 1]},
     {maxphoton, maxphoton}];

   outputflux = 10^flux  (1 + (2 Δ  κ)^2);
   noiseempty = Sqrt[τ outputflux];
   noisefull = Sqrt[(0.5 * κ * τ) * Tr[a.(ρ1 + ρ2)] * Tr[adag.(ρ1 + ρ2)]];
   noiseSig = Sqrt[2 * noiseempty^2 + 2 * noisefull^2];
   noisefullAPD =
    Sqrt[(0.5 * κ * τ) *
      ((Tr[adag.a.adag.a.(ρ1 + ρ2)]) - (Tr[adag.a.(ρ1 + ρ2)])^2)];
   noiseSigAPD = Sqrt[noiseempty^2 + noisefullAPD^2];
   {{θ  Γ, Δ  κ}, ( Tr[adag.a.ρ1] + Tr[adag.a.ρ2]),
    0.5 * κ * τ * (outputflux  (κ  2) - ( Tr[adag.a.ρ1] + Tr[adag.a.ρ2]))
      noiseSigAPD,
    (0.5 * κ * τ * (outputflux  (κ  2) - Tr[a.(ρ1 + ρ2)] * Tr[adag.(ρ1 + ρ2)])
       noiseSig), outputflux, Tr[ρ1], Tr[ρ2]},
   {θd, θmin, θmax, θstep}, {Δd, Δmin, Δmax, Δstep}];
 dataarray = Append[dataarray, data];
 fluxtable = Append[fluxtable, flux],
 {flux, fluxmin, fluxmax, fluxstep}];
(* output syntax: {{Δ,θ,κ}, n, apd, het, emptyflux, Tr[ρ1], Tr[ρ2]} *)
```

APPENDIX

B

ATFILMS SUBSTRATE

The reflectivity of mirror coatings is necessarily wavelength-dependent. The mirrors for our detection cavity were custom designed and coated at ATFilms as modified quarter-wave stacks - with the requirement of high transmittance at two distinct wavelengths. The following plot shows simulated transmission data for the designed coating (solid line) and an un-modified 780nm quarter-wave stack (dashed line).

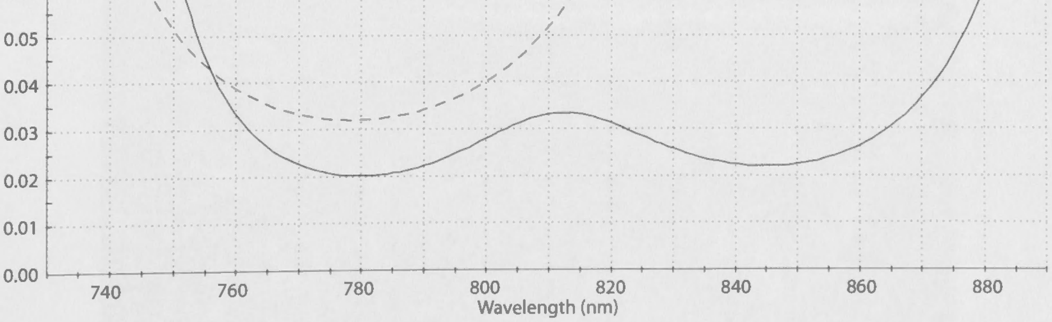

Figure B.1: Detection cavity output mirror transmittance data from ATFilms

APPENDIX

C

LABVIEW® CODE

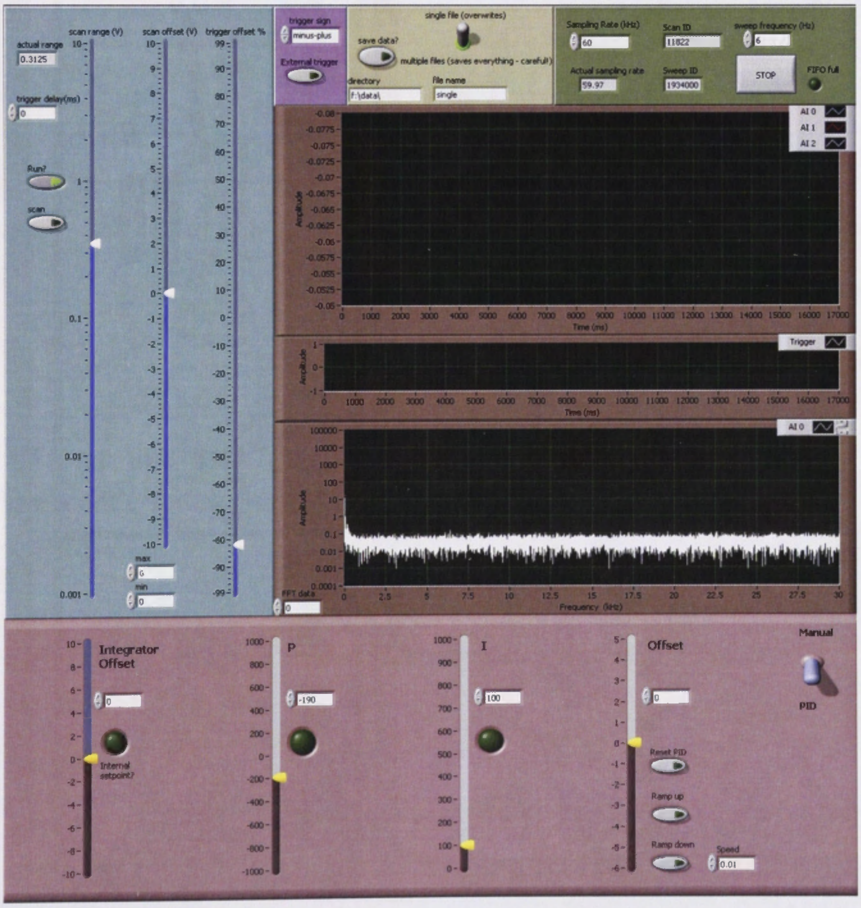

actual range: 0.3125
trigger delay(ms): 0
trigger sign: minus-plus
directory: f:\data\
file name: single
Sampling Rate (kHz): 60
Scan ID: 11822
sweep frequency (Hz): 6
Actual sampling rate: 59.97
Sweep ID: 1934000
max: 6
min: 0
FFT data: 0
Integrator Offset: 0
P: -190
I: 100
Offset: 0
Speed: 0.01

Figure C.1: Front panel of LabVIEW oscilloscope and locking control for the science cavity monitoring and manipulation.

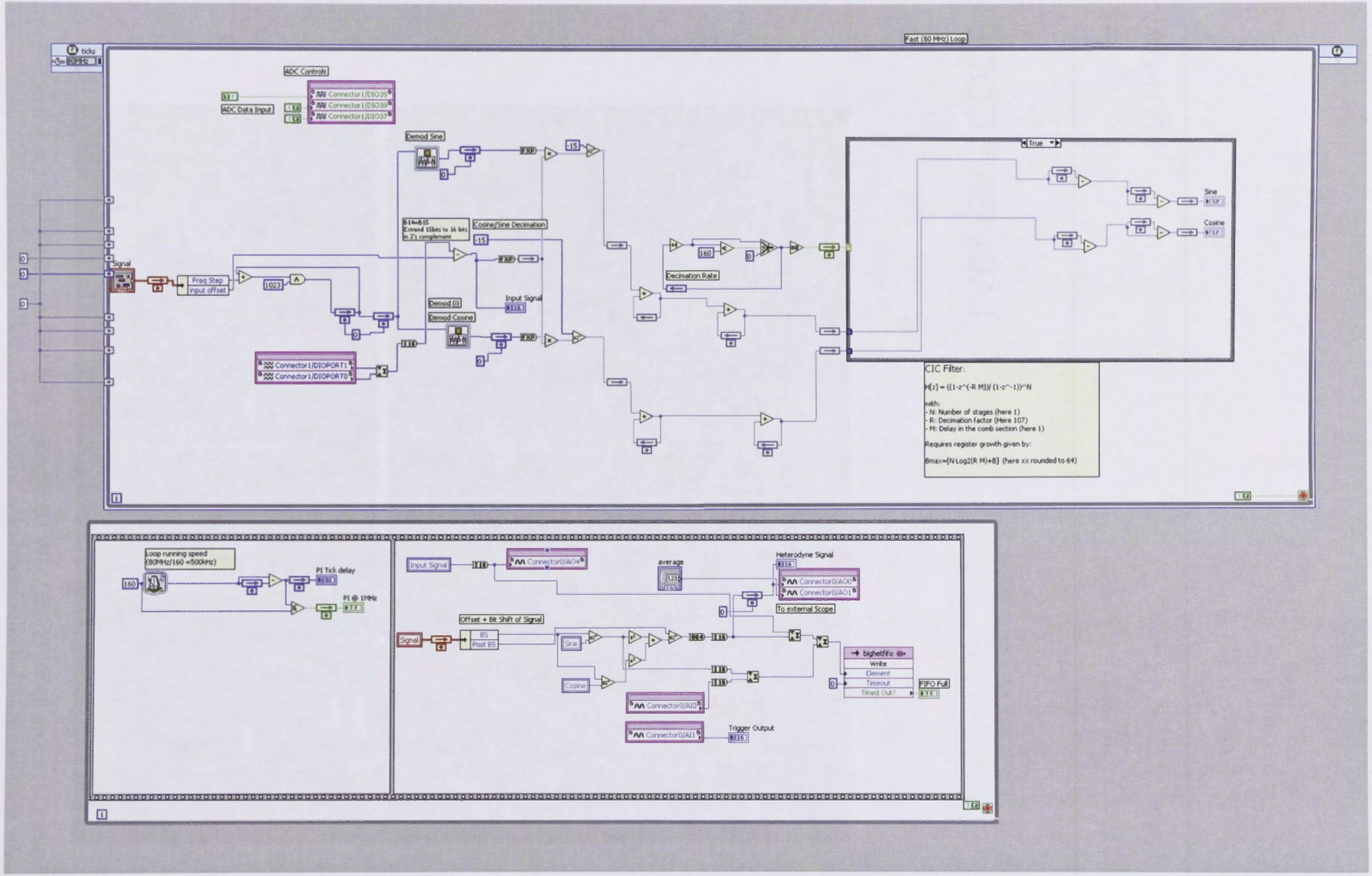

CIC Filter:

H[z] = (((1-z^(-R M))/ (1-z^-1))^N

with:
- N: Number of stages (here 1)
- R: Decimation factor (Here 107)
- M: Delay in the comb section (here 1)

Requires register growth given by:

Bmax=[N Log2(R M)+B] (here xx rounded to 64)

Figure C.2: Block diagram of LabVIEW demodulation code.

APPENDIX

D

PHOTON STATISTICS

In chapter 6 we discussed the relation between the variance and mean of photons in a fluorescence measurement. If we account for background photons with a Poisson distribution

$$p_1(n) = \frac{\langle n_0 \rangle^n}{n!} e^{-\langle n_0 \rangle}$$

with mean $\langle n_0 \rangle$, as well as fluorescence photons (also with a Poisson distribution) from m atoms:

$$p_2(n) = \frac{(\alpha m)^n}{n!} e^{-(\alpha m)},$$

with mean (αm), then the total distribution of photons for an arbitrary distribution of atoms, $p_{at}(m)$ is given by

$$p(n) = \sum_m p_{\text{atom}}(m) \frac{(\alpha m + \langle n_0 \rangle)^n}{n!} e^{-(\alpha m + \langle n_0 \rangle)}$$

The mean of the total photon distribution is

$$\begin{aligned}
\langle n \rangle &= \sum_n n p(n) \\
&= \sum_n n \sum_m p_{\text{atom}}(m) \frac{(\alpha m + \langle n_0 \rangle)^n}{n!} e^{-(\alpha m + \langle n_0 \rangle)} \\
&= \sum_m p_{\text{atom}}(m) \sum_n n \frac{(\alpha m + \langle n_0 \rangle)^n}{n!} e^{-(\alpha m + \langle n_0 \rangle)} \\
&= \sum_m p_{\text{atom}}(m) [\langle n_0 \rangle + (\alpha m)] \\
&= \langle n_0 \rangle + \alpha \langle m \rangle
\end{aligned} \tag{D.1}$$

We can similarly find the value for $\langle n^2 \rangle$:

$$\begin{aligned}
\langle n^2 \rangle &= \sum_n n^2 p(n) \\
&= \sum_n n^2 \sum_m p_{\text{atom}}(m) \frac{(\alpha m + \langle n_0 \rangle)^n}{n!} e^{-(\alpha m + \langle n_0 \rangle)} \\
&= \sum_m p_{\text{atom}}(m) \sum_n n^2 \frac{(\alpha m + \langle n_0 \rangle)^n}{n!} e^{-(\alpha m + \langle n_0 \rangle)} \\
&= \sum_m p_{\text{atom}}(m) \langle (\alpha m + \langle n_0 \rangle)^2 \rangle
\end{aligned} \tag{D.2}$$

Using the property of Poisson statistics that relates the mean of a variable (λ) to the mean of its square ($\langle x^2 \rangle$): $\langle x^2 \rangle = \lambda^2 + \lambda$, where $\lambda = (\alpha m + \langle n_0 \rangle)$, equation (D.2) becomes:

$$\begin{aligned}
\langle n^2 \rangle &= \sum_m p_{\text{atom}}(m) [(\alpha m + \langle n_0 \rangle)^2 + (\alpha m + \langle n_0 \rangle)] \\
&= \langle n_0 \rangle^2 + \langle n_0 \rangle + 2\alpha \langle n_0 \rangle \langle m \rangle + \alpha \langle m \rangle + \alpha^2 \langle m^2 \rangle
\end{aligned} \tag{D.3}$$

The variance is Var(n) $\equiv \langle n^2 \rangle - \langle n \rangle^2$, so making use of equations (D.1) and (D.2)

$$\text{Var}(n) = \langle n \rangle + \alpha^2 Var(m)$$

and

$$\frac{\text{Var}(n)}{\langle n \rangle} = 1 + \alpha \frac{Var(m)}{\langle m \rangle + \langle n_0 \rangle / \alpha}$$

BIBLIOGRAPHY

[1] Sputter-ion pumps - measurement of performance characteristics. Technical Comittee ISO/TC 112, 1992.

[2] Advanced thin films. www.atfilms.com, Jun 2011.

[3] Moglabs. http://www.moglabs.com, Jun 2011.

[4] Perkin elmer. www.optoelectronics.perkinelmer.com, Jun 2011.

[5] T. T. Aalto, M. Harjanne, and M. Kapulainen. Method for the rotational alignment of polarization-maintaining optical fibers and waveguides. *Optical Engineering*, 42:2861–2867, Jan 2003.

[6] P. Alsing and H. Carmichael. Spontaneous dressed-state polarization of a coupled atom and cavity mode. *Quantum Optics*, 3:13–32, Jan 1991.

[7] W. Alt. An objective lens for efficient fluorescence detection of single atoms. *Optik-International Journal for Light and Electron Optics*, 3:142–144, Jan 2002.

[8] P. A. Altin, G. McDonald, D. Döring, J. E. Debs, T. H. Barter, J. D. Close, N. P. Robins, S. A. Haine, and R. P. Anderson. Optically trapped atom interferometry using the clock transition of large 87Rb Bose-Einstein condensates. *New Journal of Physics*, 13, 2011.

[9] P. A. Altin, N. P. Robins, R. Poldy, J. E. Debs, D. Döring, C. Figl, and J. D. Close. Measurement of inelastic losses in a sample of ultracold 85Rb. *Physical Review A*, 81:012713(4), Jan 2010.

[10] M. Anderson, J. Ensher, M. Matthews, C. Wieman, and E. Cornell. Observation of Bose-Einstein condensation in a dilute atomic vapour. *Science*, 269(5221):198–201, Jan 1995.

[11] M. Andrews, C. G. Townsend, H.-J. Miesner, D. S. Durfee, D. M. Kurn, and W. Ketterle. Observation of interference between two Bose condensates. *Science*, 275:637, May 1997.

[12] A. Aspect, P. Grangier, and G. Roger. Experimental realization of Einstein-Podolsky-Rosen-Bohm gedankenexperiment: A new violation of Bell's inequalities. *Physical Review Letters*, 49(2):94–97, 1982.

[13] H. A. Bachor. *A Guide to Experiments in Quantum Optics*. Wiley-VCH, 1998.

[14] W. S. Bakr, J. I. Gillen, A. Peng, S. Fölling, and M. Greiner. A quantum gas microscope for detecting single atoms in a Hubbard-regime optical lattice. *Nature*, 462:74–78, Oct 2009.

[15] K. Baumann, C. Guerlin, F. Brennecke, and T. Esslinger. Dicke quantum phase transition with a superfluid gas in an optical cavity. *Nature*, 464:1301–1307, Apr 2010.

[16] P. R. Berman. Atom interferometry. page 478, Jan 1997.

[17] L. S. Bishop, J. M. Chow, J. Koch, A. A. Houck, M. H. Devoret, E. Thuneberg, S.M.Girvin, and R. Schoelkopf. Nonlinear response of the vacuum Rabi resonance. *Nature Physics*, pages 105–109, Jan 2009.

[18] I. Bloch and T. W. H. Esslinger. Measurement of the spatial coherence of a trapped Bose gas at the phase transition. *Nature*, 403:166–170, Dec 1999.

[19] T. Bourdel, T. Donner, S. Ritter, A. Ottl, M. Kohl, and T. Esslinger. Cavity QED detection of interfering matter waves. *Physical Review A*, 73(4):043602, Jan 2006.

[20] D. Bouwmeester, J.-W. Pan, K. Mattle, M. Eibl, H. Weinfurter, and A. Zeilinger. Experimental quantum teleportation. *Nature*, 390:575–579, 1997.

[21] P. Bouyer and M. A. Kasevich. Heisenberg-limited spectroscopy with degenerate Bose-Einstein gases. *Physical Review A*, 63:1083, 1997.

[22] S. Brattke, B. Varcoe, and H. Walther. Generation of photon number states on demand via cavity quantum electrodynamics. *Physical Review Letters*, 86(16):3534–3537, Jan 2001.

[23] F. Brennecke, T. Donner, S. Ritter, T. Bourdel, M. Koehl, and T. Esslinger. Cavity QED with a Bose-Einstein condensate. *Nature*, 450(7167):268–U8, Jan 2007.

[24] F. Brennecke, S. Ritter, T. Donner, and T. Esslinger. Cavity optomechanics with a Bose-Einstein condensate. *Science*, 322:235–238, Oct 2008.

[25] B. C. Buchler. *Electro-optic Control of Quantum Measurements*. PhD thesis, Australian National University, Canberra, Sep 2001.

[26] R. Bücker, J. Grond, S. Manz, T. Berrada, T. Betz, C. Koller, U. Hohenester, T. Schumm, A. Perrin, and J. Schmiedmayer. Twin-atom beams. *Nature Physics*, 8(7), 2011.

[27] E. A. Burt, R. W. Ghrist, C. J. Myatt, M. J. Holland, E. A. Cornell, and C. E. Wieman. Coherence, correlations, and collisions - what one learns about Bose-Einstein condensates from their decay. *Physical Review Letters*, 79:337, Jul 1997.

[28] M. Cadoret, E. D. Mirandes, P. Cladé, S. Guellati-Khélifa, C. Schwob, F. Nez, L. Julien, and F. Biraben. Combination of Bloch oscillations with a Ramsey-Bordé interferometer: New determination of the fine structure constant. *Physical Review Letters*, 101:230801, Dec 2008.

[29] T. Campey, C. Vale, M. Davis, N. Heckenberg, H. Rubinsztein-Dunlop, S. Kraft, C. Zimmermann, and J. Fortágh. Atom counting in ultracold gases using photoionization and ion detection. *Physical Review A*, 74(4):9, Oct 2006.

[30] H. J. Carmichael. Statistical methods in quantum optics 2: Non-classical fields. page 540, Jan 2007.

[31] H. J. Carmichael and B. C. Sanders. Multiatom effects in cavity QED with atomic beams. *Physical Review A*, 60:2497–2504, Sep 1999.

[32] C. W. Chou, D. B. Hume, J. C. J. Koelemeij, D. J. Wineland, and T. Rosenband. Frequency comparison of two high-accuracy Al^+ optical clocks. *Physical Review Letters*, 104(7):070802, Feb 2010.

[33] C.-S. Chuu, F. Schreck, T. Meyrath, J. Hanssen, G. Price, and M. Raizen. Direct observation of sub-poissonian number statistics in a degenerate Bose gas. *Physical Review Letters*, 95(26):260403, Dec 2005.

[34] J. I. Cirac and P. Zoller. Quantum computation with cold trapped ions. *Physical Review Letters*, 74(20):4091(4), May 1995.

[35] J. I. Cirac and P. Zoller. New frontiers in quantum information with atoms and ions. *Physics Today*, 57(3):38–44, 2004.

[36] P. Cladé, E. D. Mirandes, M. Cadoret, S. Guellati-Khélifa, C. Schwob, F. Nez, L. Julien, and F. Biraben. Determination of the fine structure constant based on Bloch oscillations of ultracold atoms in a vertical optical lattice. *Physical Review Letters*, 96:033001, Jan 2006.

[37] Y. L. Coq, J. Thywissen, S. Rangawala, F. Gerbier, S. Richard, G. Delannoy, P. Bouyer, and A. Aspect. Atom laser divergence. *Physical Review Letters*, 87(17):170403, Jan 2001.

[38] S. L. Cornish, S. T. Thompson, and C. E. Wieman. Formation of bright matter-wave solitons during the collapse of attractive Bose-Einstein condensates. *Physical Review Letters*, 96(17):170401, May 2006.

[39] A. Cronin, J. Schmiedmayer, and D. Pritchard. Optics and interferometry with atoms and molecules. *Reviews of Modern Phys*, 81:1–10, Sep 2009.

[40] K. Davis, M. Mewes, M. Andrews, N. Vandruten, D. Durfee, D. Kurn, and W. Ketterle. Bose-Einstein condensation in a gas of sodium atoms. *Physical Review Letters*, 75(22):3969–3973, Jan 1995.

[41] D.J.Wineland, J.J.Bollinger, W.M.Itano, and D.J.Heinzein. Squeezed atomic states and projection noise in spectroscopy. *Physical Review A*, 50(1), 1994.

[42] A. Doherty, A. Parkins, S. Tan, and D. Walls. Motion of a two-level atom in an optical cavity. *Physical Review A*, 56:833, Jan 1997.

[43] L.-M. Duan, A. Sorensen, J. I. Cirac, and P. Zoller. Squeezing and entanglement of atomic beams. *Physical Review Letters*, 85:3991, 2000.

[44] J. Dunningham, K. Burnett, and W. D. Phillips. Bose-Einstein condensates and precision measurements. *Philosophical Transactions of the Royal Society A: Mathematical, Physical and Engineering Sciences*, 363(1834):2165–2175, Jul 2005.

[45] J. Esteve, C. Gross, A. Weller, S. Giovanazzi, and M. K. Oberthaler. Squeezing and entanglement in a Bose-Einstein condensate. *Nature*, 455(7217):1216–1219, Oct 2008.

[46] M. Fattori, C. D'errico, G. Roati, M. Zaccanti, M. Jona-Lasinio, M. Modugno, M. Inguscio, and G. Modugno. Atom interferometry with a weakly interacting Bose-Einstein condensate. *Physical Review Letters*, 100(8):080405, Feb 2008.

[47] R. P. Feynman, F. V. Jr., and R. W. Hellwarth. Geometrical representation of the Schrödinger equation for solving maser problems. *Journal of Applied Physics*, 28:49–52, 1957.

[48] J. B. Fixler, G. T. Foster, J. M. Mcguirk, and M. A. Kasevich. Atom interferometer measurement of the Newtonian constant of gravity. *Science*, 315(5808):74–77, Jan 2007.

[49] M. Fleischhauer and S. Gong. Stationary source of nonclassical or entangled atoms. *Physical Review Letters*, 88:07040, 2002.

[50] G. M. H. (for the LIGO Scientific Collaboration). Advanced LIGO: the next generation of gravitational wave detectors. *Classical and Quantum Gravity*, 27(8):084006, 2010.

[51] I. Gerhardt, G. Wrigge, P. Bushev, G. Zumofen, M. Agio, R. Pfab, and V. Sandoghdar. Strong extinction of a laser beam by a single molecule. *Physical Review Letters*, 98:033601(4), Jan 2007.

[52] T. Gericke, P. Würtz, D. Reitz, T. Langen, and H. Ott. High-resolution scanning electron microscopy of an ultracold quantum gas. *Nature Physics*, 4(12):949–953, Dec 2008.

[53] M. Gilowski, C. Schubert, M. Zaiser, W. Herr, T. Wubbena, T. Wendrich, T. Muller, E. Rasel, and W. Ertmer. Narrow bandwidth interference filter-stabilized diode laser systems for the manipulation of neutral atoms. *Optics Communications*, 280:443–447, Dec 2007.

[54] K. Goda, E. E. Mikhailov, O. Miyakawa, S. Saraf, S. Vass, A. WEinstein, and N. Mavalvala. Generation of a stable low-frequency squeezed vacuum field with periodically-poled KTiOPO$_4$ at 1064 nm. *Optics Letters*, 33(2):92–94, 2008.

[55] J. Goldwin, M. Trupke, J. Kenner, A. Ratnapala, and E. Hinds. Fast cavity-enhanced atom detection with low noise and high fidelity. *Nature Communications*, 2:418, Aug 2011.

[56] R. Grimm and Y. B. Ovchinnikov. Optical dipole traps for neutral atoms. *arXiv*, physics.atom-ph, Feb 1999.

[57] C. Gross, T. Zibold, E. Nicklas, J. Estève, and M. K. Oberthaler. Nonlinear atom interferometer surpasses classical precision limit. *Nature*, 464(7292):1165–1169, Apr 2010.

[58] S. Gupta, K. Dieckmann, Z. Hadzibabic, and D. E. Prichard. Contrast interferometry using Bose-Einstein condensates to measure h/m and α. *Physical Review Letters*, 89:140401, Sept 2002.

[59] T. Gustavson, P. Bouyer, and M. Kasevich. Precision rotation measurements with an atom interferometer gyroscope. *Physical Review Letters*, 78:2046, Jan 1997.

[60] A. Haase, B. Hessmo, and J. Schmiedmayer. Detecting magnetically guided atoms with an optical cavity. *Optics Letters*, 31(2):268–270, Jan 2006.

[61] E. Hagley, L. Deng, M. Kozuma, J. Wen, K. Helmerson, S. Rolston, and W. Phillips. A well-collimated quasi-continuous atom laser. *Science*, 283(5408):1706–1709, Jan 1999.

[62] S. Haine and M. Johnsson. Dynamic scheme for generating number squeezing in Bose-Einstein condensates through nonlinear interactions. *Physical Review A*, 80(2):023611, Aug 2009.

[63] S. A. Haine and J. J. Hope. Outcoupling from a Bose-Einstein condensate with squeezed light to produce entangled-atom laser beams. *Physical Review A*, 72(3):033601, Sep 2005.

[64] S. A. Haine, M. K. Olsen, and J. J. Hope. Generating controllable atom-light entanglement with a Raman atom laser system. *Physical Review Letters*, 96(13):133601, Apr 2006.

[65] K. Hammerer, M. Wallquist, C. Genes, M. Ludwig, F. Marquardt, P. Treutlein, P. Zoller, J. Ye, and H. J. Kimble. Strong coupling of a mechanical oscillator and a single atom. *Arxiv preprint*, page 5, Jul 2009.

[66] C. J. Hawthorn, K. P. Weber, and R. E. Scholten. Littrow configuration tunable external cavity diode laser with fixed direction output beam. *Review of Scientific Instruments*, 72:4477–4479, Nov 2001.

[67] K. Hennessy, A. Badolato, M. Winger, D. Gerace, M. Atature, S. Gulde, S. Falt, E. Hu, and A. Imamoglu. Quantum nature of a strongly coupled single quantum dot–cavity system. *Nature*, 445:896–899, Feb 2007.

[68] S. S. Hodgman, R. G. Dall, A. G. Manning, K. G. H. Baldwin, and A. G. Truscott. Direct measurement of long-range third-order coherence in Bose-Einstein condensates. *Science*, 331:1046, Feb 2011.

[69] E. B. Hogenauer. Acoustic, speech, and signal processing. *IEEE Transaction*, 29(155), 1981.

[70] C. Hood, M. Chapman, T. Lynn, and H. Kimble. Real-time cavity QED with single atoms. *Physical Review Letters*, 80(19):4157–4160, Jan 1998.

[71] C. Hood, H. Kimble, and J. Ye. Characterization of high-finesse mirrors: Loss, phase shifts, and mode structure in an optical cavity. *Physical Review A*, 64(3):033804, Jan 2001.

[72] C. J. Hood. *Real-time Measurement and Trapping of Single Atoms by Single Photons*. PhD thesis, California Institute of Technology, Pasadena, California, May 2000.

[73] P. Horak, B. G. Klappauf, P. Domokos, and E. A. Hinds. Possibility of single-atom detection on a chip. *Physical Review A*, 67(4):043806, Apr 2003.

[74] Z. Hu and H. Kimble. Observation of a single-atom in a magneto optical trap. *Optics Letters*, 19(22):1888–1890, Jan 1994.

[75] J. Janousek, K. Wagner, J.-F. Morizur, N. Treps, P. K. Lam, C. C. Harb, and H.-A. Bachor. Optical entanglement of co-propagating modes. *Nature Photonics*, 3(7):399–402, Jul 2009.

[76] E. Jaynes and F. Cummings. Comparison of quantum and semiclassical radiation theories with application to beam maser. *Proceedings of the IEEE*, 51(1):89–109, Jan 1963.

[77] T. Jeltes, J. M. McNamara, W. Hogervorst, W. Vassen, V. Krachmalnicoff, M. Schellekens, A. Perrin, H. Chang, D. Boiron, A. Aspect, and C. I. Westbrook. Comparison of the Hanbury Brown-Twiss effect for bosons and fermions. *Nature*, 445(7126):402–405, Jan 2007.

[78] M. Jeppesen, J. Dugué, G. Dennis, M. Johnsson, C. Figl, N. Robins, and J. Close. Approaching the Heisenberg limit in an atom laser. *Physical Review A*, 77(6):063618, Jun 2008.

[79] H. Jing, J.-L. Chen, and M.-L. Ge. Nonclassical effect in the mit output coupler for the Bose-Einstein condensate. *Physical Review A*, 63:01561, 2000.

[80] M. A. Kasevich. Coherence with atoms. *Science*, 298(5597):1363–1368, Nov 2002.

[81] G. Khitrova, H. M. Gibbs, M. Kira, S. W. Koch, and A. Scherer. Vacuum Rabi splitting in semiconductors. *Nature Physics*, 2:10, Jan 2006.

[82] H. Kimble. Strong interactions of single atoms and photons in cavity QED. *Physica Scripta*, T76:127–137, Jan 1998.

[83] T. Kinoshita, T. Wenger, and D. Weiss. Local pair correlations in one-dimensional Bose gases. *Physical Review Letters*, 95:190406, Nov 2005.

[84] M. Kitagawa and M. Ueda. Squeezed spin states. *Physical Review A*, 47(6):5138, Aug 1993.

[85] M. Köhl, T. W. Hänsch, and T. Esslinger. Measuring the temporal coherence of an atom laser beam. *Physical Review Letters*, 87(16):160404, Sep 2001.

[86] B. Kubala, M. Ludwig, and F. Marquardte. Optomechanics. *arXiv:0902.2163*, 2009.

[87] S. Kuhr, W. Alt, D. Schrader, M. Muller, V. Gomer, and D. Meschede. Deterministic delivery of a single atom. *Science*, 293(5528):278–280, Jan 2001.

[88] G. Lamporesi, A. Bertoldi, L. Cacciapuoti, M. Prevedelli, and G. Tino. Determination of the Newtonian gravitational constant using atom interferometry. *Physical Review Letters*, 100:050801, Feb 2008.

[89] R. Lapkiewicz, P. Li, C. Schaeff, N. K. Langford, S. Ramelow, M. Wie□niak, and A. Zeilinger. Experimental non-classicality of an indivisible quantum system. *Nature*, 474:490–493, 2011.

[90] Y. Li, P. Treutlein, J. Reichel, and A. Sinatra. Spin squeezing in a bimodal condensate: spatial dynamics and particle losses. *European Physics Journal B*, 68:365–381, 2009.

[91] J. E. Lye, J. J. Hope, and J. D. Close. Nondestructive dynamic detectors for Bose-Einstein condensates. *Physical Review A*, 67(4):043609, Apr 2003.

[92] H. Mabuchi and A. C. Doherty. Cavity quantum electrodynamics: Coherence in context. *Science*, 298:1372, Apr 2008.

[93] H. Mabuchi, Q. Turchette, M. Chapman, and H. Kimble. Real-time detection of individual atoms falling through a high-finesse optical cavity. *Optics Letters*, 21(17):1393–1395, Jan 1996.

[94] P. Maioli, T. Meunier, S. Gleyzes, A. Auffeves, G. Nogues, M. Brune, J. Raimond, and S. Haroche. Nondestructive Rydberg atom counting with mesoscopic fields in a cavity. *Physical Review Letters*, 94(11):113601, Jan 2005.

[95] P. Maunz, T. Puppe, T. Fischer, P. Pinkse, and G. Rempe. Emission pattern of an atomic dipole in a high-finesse optical cavity. *Optics Letters*, 28:46–48, Jan 2003.

[96] D. Meschede, H. Walther, and G. Müller. One-atom maser. *Physical Review Letters*, 54(6):551–552, Jan 1985.

[97] H. J. Metcalf and P. V. D. Straten. *Laser Cooling and Trapping*. Springer-Verlag New York Inc., 2001.

[98] M. Mewes, M. Andrews, D. Kurn, D. Durfee, C. Townsend, and W. Ketterle. Output coupler for Bose-Einstein condensed atoms. *Physical Review Letters*, 78(4):582–585, Jan 1997.

[99] K. Molmer. Quantum atom optics with Bose-Einstein condensates. *New Journal of Physics*, 5:55.1–55.16, Jan 2003.

[100] A. B. Mundt, A. Kreuter, C. Russo, C. Becher, D. Leibfried, J. Eschner, F. Schmidt-Kaler, and R. Blatt. Coherent coupling of a single $^{40}Ca^{+}$ ion to a high-finesse optical cavity. *Applied Physics B*, 76, Jan 2003.

[101] P. Munstermann, T. Fischer, P. Maunz, P. Pinkse, and G. Rempe. Dynamics of single-atom motion observed in a high-finesse cavity. *Physical Review Letters*, 82(19):3791–3794, Jan 1999.

[102] P. Munstermann, T. Fischer, P. Pinkse, and G. Rempe. Single slow atoms from an atomic fountain observed in a high-finesse optical cavity. *Optics Communications*, 159(1-3):63–67, Jan 1999.

[103] A. Ottl, S. Ritter, M. Kohl, and T. Esslinger. Correlations and counting statistics of an atom laser. *Physical Review Letters*, 95(9):090404, Jan 2005.

[104] A. Öttl, S. Ritter, M. Köhl, and T. Esslinger. Hybrid apparatus for Bose-Einstein condensation and cavity quantum electrodynamics: Single atom detection in quantum degenerate gases. *Review of Scientific Instruments*, 77(6):063118, Jan 2006.

[105] A. Ozawa, J. Rauschenberger, Ch. Gohle, M. Herrmann, D. Walker, V. Pervak, A. Fernandez, R. Graf, A. Apolonski, R. Holzwarth, F. Krausz, T. Hänsch, and Th. Udem. High harmonic frequency combs for high resolution spectroscopy. *Physical Review Letters*, 100(25):253901(4), Jun 2008.

[106] T. E. Parker. Long-term comparison of caesium fountain primary frequency standards. *Metrologia*, 47:1–10, Dec 2009.

[107] A. Perrin, H. Chang, V. Krachmalnicoff, M. Schellekens, D. Boiron, A. Aspect, and C. I. Westbrook. Observation of atom pairs in spontaneous four-wave mixing of two colliding Bose-Einstein condensates. *Physical Review Letters*, 99(15):150405, Jan 2007.

[108] A. Peters, K. Y. Chung, and S. Chu. Measurement of gravitational acceleration by dropping atoms. *Nature*, 400:849–852, Aug 1999.

[109] P. W. H. Pinkse, T. Fischer, P. Maunz, T. Puppe, and G. Rempe. How to catch an atom with single photons. *Journal of Modern Optics*, 47(14):2769–2787, Nov 2000.

[110] R. Poldy, B. C. Buchler, and J. D. Close. Single-atom detection with optical cavities. *Physical Review A*, 78(1):013640, Jul 2008.

[111] H. Pu and P. Meystre. Creating macroscopic atomic Einstein-Podolsky-Rosen states from Bose-Einstein condensates. *Physical Review Letters*, 85:3987, Nov 2000.

[112] J. Raimond, M. Brune, and S. Haroche. Colloquium: Manipulating quantum entanglement with atoms and photons in a cavity. *Review of Modern Physics*, 73(3):565–582, Jan 2001.

[113] N. F. Ramsey. History of early atomic clocks. *Metrologia*, 42:030001, Jun 2005.

[114] M. D. Reid, P. D. Drummond, E. G. Cavalcanti, W. P. Bowen, P. K. Lam, H. A. Bachor, U. L. Andersen, and G. Leuchs. The Einstein-Podolsky-Rosen paradox - a fundamental challenge and a tool for quantum engineering. *Review of Modern Physics*, 81:1727, 2009.

[115] R.G.Dall, L.J.Byron, A.G.Truscott, G.R.Dennis, M.T.Johnsson, M.Jeppensen, and J.J.Hope. Observation of transverse interference fringes on an atom laser beam. *Optics Express*, 15:17673, Dec 2007.

[116] M. F. Riedel, P. Böhi, Y. Li, T. W. Hänsch, A. Sinatra, and P. Treutlein. Atom-chip-based generation of entanglement for quantum metrology. *Nature*, 464:1170–1173, 2000.

[117] S. Ritter. *Probing Coherence During Bose-Einsteine Condensation*. PhD thesis, Swiss Federal Institute of Technology, Zurich, 2007.

[118] S. Ritter, F. Brennecke, K. Baumann, T. Donner, C. Guerlin, and T. Esslinger. Dynamical coupling between a Bose-Einstein condensate and a cavity optical lattice. *Applied Physics B*, page 3436, Feb 2009.

[119] G. Roati, M. Zaccanti, C. D'Errico, J. Catani, M. Modugno, A. Simoni, M. Inguscio, and G. Modugno. K Bose-Einstein condensate with tunable interactions. *Arxiv preprint*, page 5, Feb 2008.

[120] N. Robins, C. Figl, S. Haine, A. Morrison, M. Jeppesen, J. Hope, and J. Close. Achieving peak brightness in an atom laser. *Physical Review Letters*, 96(14):140403, Jan 2006.

[121] N. Robins, A. Morrison, J. Hope, and J. Close. Limits to the flux of a continuous atom laser. *Physical Review A*, 72:031606, 2005.

[122] M. Rosenblit, P. Horak, S. Helsby, and R. Folman. Single-atom detection using whispering-gallery modes of microdisk resonators. *Physical Review A*, 70(5):053808, 2004.

[123] M. Rosenblit, Y. Japha, P. Horak, and R. Folman. Simultaneous optical trapping and detection of atoms by microdisk resonators. *Physical Review A*, 73(6):063805, Jan 2006.

[124] B. E. A. Saleh and M. C. Teich. *Fundamentals of Photonics*. John Wiley and Sons, Inc., 1991.

[125] F. D. Santos, J. Leonard, J. Wang, C. Barrelet, F. Perales, E. Rasel, C. Unnikrishnan, M. Leduc, and C. Cohen-Tannoudji. Bose-Einstein condensation of metastable helium. *Physical Review Letters*, 86(16):3459–3462, Jan 2001.

[126] A. A. Savchenkov, A. B. Matsko, V. S. Ilchenko, and L. Maleki. Optical resonators with ten million finesse. *Optics Express*, 15(11):6768–6773, Jan 2007.

[127] M. Schellekens, R. Hoppeler, A. Perrin, J. Gomes, D. Boiron, A. Aspect, and C. Westbrook. Hanbury Brown Twiss effect for ultracold quantum gases. *Science*, 310(5748):648–651, Jan 2005.

[128] A. Schliesser, N. Nooshi, P. Del'Haye, and K. Vahala. Cooling of a micromechanical oscillator using radiation-pressure induced dynamical backaction. *Quantum Electronics and Laser Science Conference*, Jan 2007.

[129] J. Schoser, A. Batär, R. Löw, V. Schweikhard, A. Grabowski, Y. B. Ovchinnikov, and T. Pfau. Intense source of cold Rb atoms from a pure two-dimensional magneto-optical trap. *Physical Review A*, 66:023410, Aug 2002.

[130] D. A. Shaddock, B. C. Buchler, W. P. Bowen, M. B. Gray, and P. K. Lam. Modulation-free control of a continuous-wave second-harmonic generator. *Journal of Optics A*, 2:400–404, Jun 2000.

[131] J. F. Sherson, C. Weitenberg, M. Endres, M. Cheneau, I. Bloch, and S. Kuhr. Single-atom-resolved fluorescence imaging of an atomic mott insulator. *Nature*, 467:68–72, Sep 2010.

[132] A. Sorensen, A. Duan, L. Cirac, and P. Zoller. Many-particle entanglement with Bose-Einstein condensates. *Nature*, 409:63–66, 2001.

[133] B. M. Sparkes, H. M. Chrzanowski, D. P. Parrain, B. C. Buchler, P. K. Lam, and T. Symul. A scalable, self-analyzing digital locking system for use on quantum optics experiments. *arXiv:1105.3795v3*, 2011.

[134] D. Steck. http://steck.us/alkalidata/rubidium87numbers.1.6.pdf, Jun 2011.

[135] M. L. Terraciano, R. O. Knell, D. G. Norris, J. Jing, A. Fernández, and L. A. Orozco. Photon burst detection of single atoms in an optical cavity. *Nature Physics*, page 1282, May 2009.

[136] R. J. Thompson, G. Rempe, and H. J. Kimble. Observation of normal-mode-splitting for an atom in an optical cavity. *Physical Review Letters*, 68:1132–1135, Feb 1992.

[137] P. Treutlein, K. Chung, and S. Chu. High-brightness atom source for atomic fountains. *Nature*, 63:051401, Apr 2001.

[138] M. Trupke, J. Goldwin, B. Darquie, G. Dutier, S. Eriksson, J. Ashmore, and E. A. Hinds. Atom detection and photon production in a scalable, open, optical microcavity. *Physical Review Letters*, 99(6):063601, Jan 2007.

[139] K. Vahala, editor. *Optical Microcavities*. World ScientificPublishing Co. Pte. Ltd., 2007.

[140] S. van Enk, H. Kimble, and H. Mabuchi. Quantum information processing in cavity-QED. *Quantum Information Processing*, 3(1-5):75–88, Jan 2004.

[141] A. Wallraff, D. I. Schuster, A. Blais, L. Frunzio, R.-S. Huang, J. Majer, S. Kumar, S. M. Girvin, and R. Schoelkopf. Strong coupling of a single photon to a superconducting qubit using circuit quantum electrodynamics. *Nature*, 431, Sep 2004.

[142] S. Weis, R. Riviere, S. Deleglise, E. Gavartin, O. Arcizet, A. Schliesser, and T. J. Kippenberg. Optomechanically induced transparency. *Science*, 330:1520–1523, Dec 2010.

[143] C. I. Westbrook, M. Schellekens, A. Perrin, V. Krachmalnicoff, J. V. Gomes, J.-B. Trebbia, J. Estève, H. Chang, I. Bouchoule, D. Boiron, A. Aspect, T. Jeltes, J. McNamara, W. Hogervorst, and W. Vassen. Producing and detecting correlated atoms. *AIP Conference Proceedings*, 869:181–187, Oct 2006.

[144] M. Wilzbach, A. Haase, M. Schwarz, D. Heine, K. Wicker, X. Liu, K.-H. Brenner, S. Groth, T. Fernholz, B. Hessmo, and J. Schmiedmayer. Detecting neutral atoms on an atom chip. *FortSchritte der Physik*, 54(8-10):746–764, Jan 2006.

[145] M. Wilzbach, D. Heine, S. Groth, X. L. andThomas Raub, B. Hessmo, and J. Schmiedmayer. Simple integrated single-atom detector. *Optics Letters*, 34:259–261, Jan 2009.

[146] D. Wineland, J. Bollinger, W. Itano, F. Moore, and D. Heinzen. Spin squeezing and reduced quantum noise in spectroscopy. *Phys. Rev. A*, 46(11):6797, Dec 1992.

[147] H. Wiseman. Defining the (atom) laser. *Physical Review A*, 56(3):2068–2084, Jan 1997.

[148] M. Yasuda and F. Shimizu. Observation of two-atom correlation of an ultracold neon atomic beam. *Physical Review Letters*, 77(15):3090–3093, Jan 1996.

[149] T. Yoshie, A. Scherer, J. Hendrickson, G. Khitrova, H. M. Gibbs, G. Rupper, C. Ell, O. B. Shchekin, and D. G. Deppe. Vacuum Rabi splitting with a single quantum dot in a photonic crystal nanocavity. *Nature*, 432:200–203, Nov 2004.

[150] H. Yuen and V. CHAN. Noise in homodyne and heterodyne detection. *Optics Letters*, 8(3):177—179, Jan 1983.

[151] H. Yuen and J. Shapiro. Optical communication with two-photon coherent states. *Information Theory*, IT-26(1):78—92, Jan 1980.

[152] P. Zhang, Y. Guo, Z. Li, Y. Zhang, Y. Zhang, J. Du, G. Li, J. Wang, and T. Zhang. Elimination of the degenerate trajectory of a single atom strongly coupled to a tilted TEM_{10} cavity mode. *Physical Review A*, 83:031804(4), Mar 2011.